

LIBRARY Michigan State University

This is to certify that the

thesis entitled

# THE SEPARATION OF LIGHT DISPERSIONS IN LONG HYDROCYCLONES

presented by

# Robert Dvorak

has been accepted towards fulfillment of the requirements for

M.S. degree in Chemical Engineering

Major professor

May 31, 1989

Date.

**O**-7639

(.)

MSU is an Affirmative Action/Equal Opportunity Institution

PLACE IN RETURN BOX to remove this checkout from your record. TO AVOID FINES return on or before date due.

DATE DUE	DATE DUE	DATE DUE
- 190 131		
10 % Fight 1 7 7532		

MSU Is An Affirmative Action/Equal Opportunity Institution

# SEPARATION OF LIGHT DISPERSIONS IN LONG HYDROCYCLONES

By

Robert Dvorak

# A THESIS

Submitted to
Michigan State University
in partial fulfillment of the requirements
for the degree of

MASTER OF SCIENCE

Department of Chemical Engineering

#### **ABSTRACT**

# SEPARATION OF LIGHT DISPERSIONS IN LONG HYDROCYCLONES

By

#### Robert Dvorak

Recent studies suggest that a double-cone hydrocyclone is more suited to the separation of dilute light dispersions than a shorter single-cone design. To explore further the capabilities of the single-cone design, a comparison of the separation performance of the two hydrocyclones at the same length was undertaken.

Flow visualization tests (at low overflow ratios) for both hydrocyclones revealed dynamic instabilities in the reverse flow vortex. Transitions from a stable reverse flow vortex to a through flow vortex were observed over periods as short as ten seconds and as long as twenty minutes.

When separating a dispersion with a small density difference  $(.025 \text{ g/cm}^3)$ , the double-cone design achieved a higher underflow purity. However, by fitting model parameters using this efficiency data, theoretical calculations suggest comparable efficiencies for the two designs when separating a suspension with a density difference typical of oilwater dispersions  $(0.1 \text{ g/cm}^3)$ .

To My Wife, Valerie

#### **ACKNOWLEDGEMENTS**

I wish to express my gratitude to Dr. C.A. Petty for his guidance and assistance throughout this study and in preparation of this manuscript.

Special thanks are also given to the gentlemen of the College of Engineering Machine Shop who assisted in the construction of the experimental apparatus.

The high density polyethylene powder used in the experimental studies was donated by the Dow Chemical Company, Midland MI. Also, the cumulative size distribution tests on this powder were performed by Particle Data Institute Laboratories, Elmhurst, IL. This work was partially funded by Battelle - Pacific Northwest Laboratories as well as the Department of Chemical Engineering at Michigan State University.

Finally, I would like to thank my wife and best friend, Valerie, for her moral support and for having endured many hours of study and writing.

# TABLE OF CONTENTS

			Page
LIST C	F TABL	JES	viii
LIST C	F FIGU	TRES	ix
LIST C	F NOTA	TIONS	xii
CHAPTE	ER		
1.	INTRO	DUCTION	1
	1.1	Motivation	1
	1.2	Objectives	5
	1.3.	Background	7
		1.3.1. General design features	7
		1.3.2. Light dispersion separations in hydrocyclones .	10
2.	SEPAR	ATION EFFICIENCY	15
	2.1.	Performance Measures for Two Component Separations	15
	2.2.	A Model for Light Dispersion Separations	21
	2.3.	The Relationship Between Centrifugal Grade Efficiency and Particle Trajectories	28
3.	PARTI	CLE-FLUID INTERACTION AND HYDRODYNAMICS	32
	3.1.	The Particle Trajectory Model	32
	3.2.	Hydrodynamics	35
		3.2.1. Axial velocity	35
		3.2.2. Radial velocity	35
		3 2 3 Tangential velocity	36

			Page
CHAPTER	<b>L</b>		
4. PA	RTICL	E TRAJECTORY CALCULATIONS	40
	4.1.	Particle Trajectory Analysis	40
		4.1.1. Nondimensionalization of the particle trajectory equation	40
		4.1.2. Solution Strategy	42
	4.2.	Application of Trajectory Calculations	44
		4.2.1. Results and discussion	44
		4.2.2. Conclusions	58
	4.3.	Correlation of the Cut Size x <sub>50</sub>	59
5.	EXPER	IMENTAL STUDIES	64
	5.1.	Hydrocyclone Designs	64
	5.2.	Experimental Flow Loop	67
	5.3.	Experimental Test Procedures	70
	5.4.	Results and Discussion	72
		5.4.1. Characterization of the dispersion	72
		5.4.2. Reverse flow vortex behavior	73
		5.4.3. Pressure drop measurements	79
		5.4.4. Underflow purity measurements	82
		5.4.5. Conclusions	87
	5.5.	Comparison of Theoretical and Experimental Results	90
		5.5.1. Centrifugal head calculations	90
		5.5.2. Estimation of the centrifugal efficiency	92
	5.6.	Application of the Cut Size Correlation	98
6	CONCL	PMOTPII	103

			Page
CHAPTER			
7.	RECOM	MENDATIONS	106
APPENDI	X		
A.	COMPU	TER PROGRAMS	109
	A.1.	Particle Trajectory Calculations	109
	A.2.	Centrifugal Grade Efficiency Calculation	119
	A.3.	Calculation of the Centrifugal Efficiency	122
В.	EXPERI	IMENTAL METHODS AND TABULATED DATA	133
	B.1.	Isokinetic Sampling Technique	133
	B.2.	Calibration of Rotameters	136
	в.3.	Filtration Methodology	137
	B.4.	Characterization of the Dispersion	137
		B.4.1. Mass density determination	138
		B.4.2. Size density determination	139
	в.5.	Pressure Drop - Flow Rate Data	143
	В.6.	Underflow Purity Data	144
LIST OF	REFE	RENCES	147

# LIST OF TABLES

		Page
TABLE		
4.1.	Dimensionless groups in trajectory calculations	45
B.1.	Diameter size vs. percentage oversize	140
B.2.	Pressure drop - flow rate data	143
B.3.	Underflow purity data for the SCI-cyclone	145
B.4.	Underflow purity data for the CT-cyclone	146

# LIST OF FIGURES

		Page
FIGURE		
1.1.	Light dispersion hydrocyclone designs	2
1.2.	Schematic of the flow patterns in a conical hydrocyclone	8
1.3.	Asymptotic behavior of the underflow purity in the CT-cyclone	13
2.1.	Schematic for the separation of a two component mixture	16
2.2.	Model for light dispersion separation in a hydrocyclone	22
2.3.	Critical trajectory for a light dispersed phase particle	29
4.1.	Example trajectories for particles in the CT-cyclone	46
4.2.	Comparison of the convective transport and the drift velocity contributions in a 100 micron size particle trajectory	48
4.3.	Comparison of the Reynolds number and drag ratio for 100 micron size particles; W = W(Rep) for curve (a), W = 1 for curve (b)	50
4.4.	Effect of inlet velocity on the centrifugal grade efficiency for the three hydrocyclone	
4.5.	The effect of re on the centrifugal grade efficiency for the CT-cyclone	

		Page
FIGURE		
4.6.	Centrifugal efficiency for the three designs with equal hydrodynamic and dispersion parameters	57
4.7.	The relationship between the dimensionless groups N <sub>3</sub> and N <sub>4</sub> for the cut size x <sub>50</sub> in the CT-cyclone	62
5.1.	Hydrocyclone designs tested in the experimental work	66
5.2.	Flow loop (nominal lengths given in cm)	68
5.3.	Operating regions for hydrocyclone designs	74
5.4.	Progression of the reverse flow vortex instability in the CT-cyclone	77
5.5.	Pressure losses for the CT-cyclone and SCI-cyclones	81
5.6.	Underflow purity for the cyclone designs	83
5.7.	Comparison of particle size distributions for the (a) feed and (b) underflow streams in the CT-cyclone. Photos represent approximately 40X enlargement of samples taken when operating at $u_F = 3.9 \text{ m/s}$ , $S_0 = 0.13$ , and $y_F \approx 250 \text{ wppm}$ . The scale next to the figures can be used to estimate particle sizes	86
5.8.	Comparison of particle size distributions for the (a) feed and (b) underflow streams in the SCI-cyclone. Photos represent approximately 40% enlargement of samples taken when operating at $u_F = 3.9$ m/s, $S_0 = 0.09$ , and $y_F \approx 250$ wppm. The scale next to the figures can be used to estimate particle sizes	89
5.9.	Theoretical vs. experimentally estimated centrifugal efficiency for the CT-cyclone	94
5.10.	$N_3^{(50)} - N_4^{(50)}$ relationship using hydrodynamic parameters based on the underflow purities of the CT- and SCI-cyclones from	
	Figure 5.6	100

		Page
FIGURE		
B.1.	Isokinetic sampling assembly	135
B.2.	Comparison of analytically fitted cumulative size distribution to experimental data for	
	HDPE powder	141
в.3.	Size density distribution for HDPE powder	142

# LIST OF NOTATIONS

a	constant in size density distribution
ao, a1, a2	polynomial coefficients in centrifugal grade efficiency approximation
b	steepness constant in size density distribution
CD	drag coefficient
C <sub>D</sub> .	drag coefficient for a sphere defined by Stoke's law
Сри	underflow pressure loss coefficient
Сро	overflow pressure loss coefficient
CT-	abbreviation for Colman-Thew double-cone hydrocyclone
D	diameter in CT-cyclone denoting transition from large taper section to small taper section
Dc	major diameter of a hydrocyclone; usually measured at the largest diameter near the inlet end
$D_{\mathbf{F}}$	feed tube diameter
$D_0$	overflow orifice diameter
$D_{U}$	underflow orifice diameter
E	total hydrocyclone efficiency (recovery)
Ec	centrifugal efficiency
E'	underflow purity
Fc	dimensionless centrifugal acceleration

$F_F(x)$ , $F_U(x)$ , $F_O(x)$	cumulative size distribution of dispersed phase in feed, underflow, and overflow streams, respectively
Fu* (x)	cumulative size distribution of dispersed phase at mixing point in light dispersion separation model
f <sub>F</sub> (x)	size density distribution of dispersed phase in feed stream
G(x)	grade efficiency (recovery)
G <sub>C</sub> (x)	centrifugal grade efficiency
G'(x)	underflow grade purity
k	power law coefficient in the free-like vortex representation of the tangential velocity
L	overall hydrocyclone length
<b>L</b>	hydrocyclone length in trajectory model coordinate system
Lc	length of cyclindrical chamber at inlet end of hydrocyclone
Lu	length of cylindrical underflow section
Lα	length of large taper section
Lp	length of small taper section
m	inlet velocity conversion factor
n	free-like vortex power index
N <sub>1</sub>	dimensionless ratio of axial residence time to radial separation time
N <sub>2</sub>	dimensionless ratio, when multiplied by $N_1$ gives a characteristic particle Reynolds number
N <sub>3</sub>	dimensionless ratio used in cut size correlation; $N_3^{(50)}$ represents this ratio used for a cut size representing a centrifugal grade efficiency of 50%

N4	dimensionless ratio used in cut size correlation; N <sub>4</sub> (50) represents this ratio used for a cut size representing a centrifugal grade efficiency of 50%
P <sub>F</sub> , P <sub>U</sub> , P <sub>O</sub>	static pressure measured at the wall of the feed tube, underflow orifice, and overflow orifice, respectively
<b>q</b> c	fraction of feed volumetric flow rate experiencing centrifugal separation
Qc	volumetric flow rate experiencing centrifugal separation
QE W	end-wall boundary layer volumetric flow rate
Qr, Qu, Qo	volumetric flow rate of the feed, underflow, and overflow streams, respectively
Qs w	side-wall boundary layer volumetric flow rate
Qν	reverse flow vortex volumetric flow rate
rc	radius of cylindrical section near inlet end of hydrocyclone
r	radial coordinate in trajectory model coordinate system; $r = \hat{r}/\hat{r}_c$ ; also used to denote particle position (see Eq.(4-6))
r	feed tube radius; $r_F = \hat{r}_F / \hat{r}_C$
r̂ <sub>I</sub> (x)	initial radial coordinate for critical tra- jectory of particle of diameter $x$ ; $r_1(x) = \hat{r}_1(x)/\hat{r}_c$
r <sub>p</sub>	particle radial position
ru	underflow radius; $r_U = \hat{r}_U / \hat{r}_C$
r̂w(z)	radial coordinate of hydrocyclone wall; $r_w(z) = \hat{r}_w(z)/\hat{r}_c$
rv	capture surface radius; $r_v = \hat{r}_v / \hat{r}_c$
re	radial coordinate denoting peak tangential velocity of continuous phase; $r_0 = \hat{r}_0/\hat{r}_c$
Ref	Reynolds number base on inlet velocity and feed diameter; Re $_F$ = $D_Fu_F/c$

Rep	Reynolds number based on particle drift velocity and particle size; $Re_p = x u_r - u_{rp} /c$
So	overflow split ratio; $S_0 = Q_0/Q_F$
Ssw	side-wall boundary layer flow ratio; $S_{SW} = Q_{SW}/Q_F$
SCI-	single-cone hydrocyclone design I
SCII-	single-cone hydrocyclone design II
t	time
T	temperature
uc	characteristic radial velocity
UF	bulk average velocity in feed tube
ur	radial component of continuous phase velocity
Urp	radial component of particle velocity
Uz	axial component of continuous phase velocity
Uz p	axial component of particle velocity
U⊕	tangential component of continuous phase velocity
VE	hydrocyclone volume
W	dimensionless drag coefficient ratio
x	equivalent Stoke's diameter of a dispersed phase particle
Xm	mode size of size density distribution
X5 0	particle diameter corresponding to a fifty percent centrifugal grade efficiency
Уг, Уш, Уо	volume fraction of dispersed phase in feed, underflow, and overflow streams, respectively
Yu *	volume fraction of dispersed phase at mixing point in light dispersion separation model
Y	functional relation between $N_3$ and $N_4$

<del>2</del>	axial coordinate in trajectory model coordinate system; $z = \hat{z}/\hat{L}$		
<b>Ž</b> I	initial axial coordinate in a particle trajectory; $z_1 = \hat{z}_1/\hat{L}$		
Ž <sub>1</sub>	axial coordinate at beginning of large taper section; $z_1 = \hat{z}_1/\hat{L}$		
22	axial coordinate at beginning of small taper section; $z_2 = \hat{z}_2/\hat{L}$		
2̂3	axial coordinate at beginning of cylindrical underflow section (CT-cyclone only); $z_3 = \hat{z}_3/\hat{L}$		
α	large taper section half-angle		
β	small taper section half-angle		
ν <sub>c</sub>	kinematic viscosity of the continuous phase		
tc, to	mass density of the continuous and dispersed phases, respectively		
$\sigma_{\mathbf{g}}$	geometric standard deviation of cumulative size distribution		
Tc	time scale characteristic of a given set of dispersion parameters $\mathbf{x}$ , $\mathbf{p}$ , $\mathbf{c}$ , and $\mathbf{c}$		
TR	characteristic time scale for radial migration of a dispersed phase particle		
Tz	characteristic axial residence time		
θ	tangential coordinate in particle trajectory model		
•	generic taper angle		

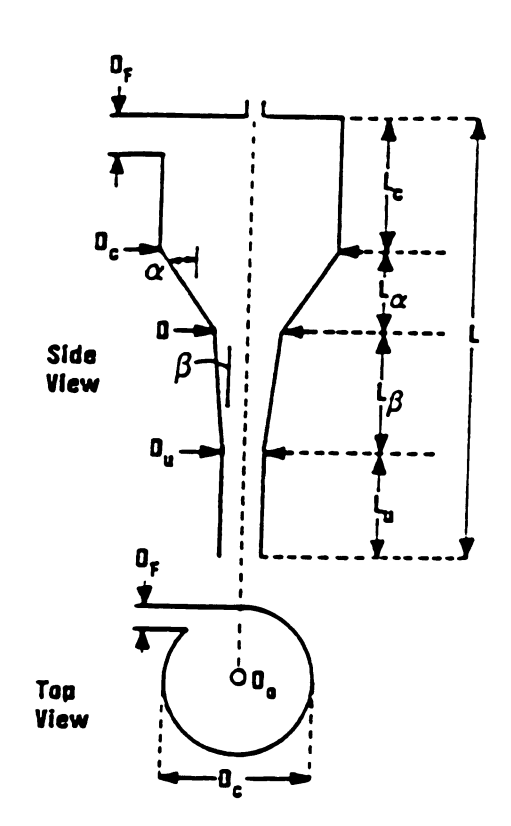
#### CHAPTER 1

#### INTRODUCTION

## 1.1. Motivation

The recent application of a class of long hydrocyclones to the separation of oil-water dispersions on offshore platforms has renewed an interest in the hydrocyclone as a liquid-liquid separator. The double-cone hydrocyclone design used in this application is based on the work of Colman [1981] at the University of Southampton. The design was able to achieve separation efficiencies of approximately 90% for crude oil-water mixtures, having a dispersed phase density of about 0.9 g/cm<sup>3</sup> and a mean drop size of 30 - 40 microns. Unfortunately, this hydrocyclone design can only meet current coastal effluent standards ( \leq 48 ppm) for feed concentrations less than 500 ppm. To improve the capability of long hydrocyclones to separate these dispersions, the underlying separation phenomena must be understood better.

Figure 1.1a shows a schematic of the Colman-Thew double cone hydrocyclone (CT-cyclone) as used by Hayes et al. [1985] and Meldrum [1987] in field testing of this concept. The design is determined by the specification of eight geometric scales:  $D_F/D_C$ ,  $D_U/D_C$ ,  $D_0/D_C$ 

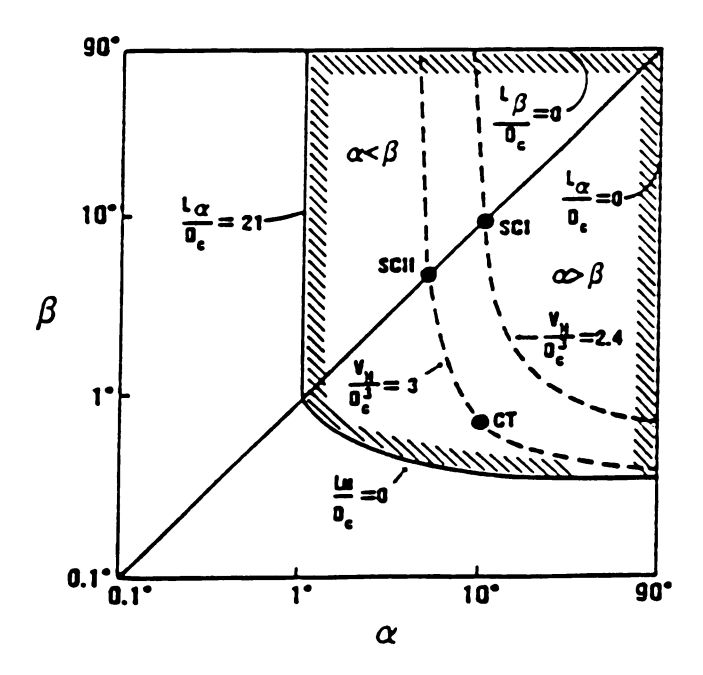


# **Geometric Scales**

	Scale	CT *	SCI	SCII
(1)	0 <sub>8</sub> /0 <sub>c</sub>	0.25	0.25	0.25
(2)	0 <sub>u</sub> /0 <sub>c</sub>	0.25	0.25	0.25
(3)	0,/0,	0.07	0.07	0.07
(4)	0/0 <sub>c</sub>	0.5	0.5	0.5
(5)	لي⁄0ء	1	1	1
(6)	UD <sub>c</sub>	22	22	22
(7)	α	10°	10°	5.24*
(8)	β	0.75*	10°	5.24*

<sup>\*</sup>Nezhati and Thew [1987], single inlet cross-sectional area equivalent to twin inlet cross-sectional area

(a) double-cone hydrocyclone design and geometric scales studied in this research



(b) hydrocyclone designs consistent with scales 1 - 6.

Figure 1.1. Light dispersion hydrocyclone designs.

inlet into a cylindrical swirl chamber, two conical sections, and a long tube leading to the underflow orifice. The majority of the experimental and operational test results are reported for hydrocyclones of diameter  $D_C = 30$  and 60 mm.

Colman and Thew have incorrectly argued that the CT-cyclone is significantly different from hydrocyclones for heavy dispersion separations (see Colman et al., 1984). There are many similarities in the geometric scales of the CT-cyclone and "conventional" hydrocyclone designs for solid-liquid separation. The cylindrical "swirl chamber" and large taper angle section of the CT-cyclone are nearly identical to conventional design scales used by Rietema [1961] and others in hydrocyclones for solid-liquid separation. The length of the swirl chamber falls within the range specified by Bradley (see p.116, 1965) for solid-liquid separations:  $2/3 \le L_C/D_C \le 2$ . Also, the use of a 10° taper angle is common in the design of hydrocyclones employed for heavy dispersion separations (see p.96 Bradley, 1965).

Colman [1981] used twin inlets to symmetrically introduce the feed but this feature was not used in practice by either Hayes et al. [1985] or Meldrum [1987], both of whom used a single inlet design. A feed diameter ratio  $D_F/D_C=0.25$  for the single inlet design results when the cross sectional areas of the twin inlet and single inlet designs are equated. This is nearly identical to the optimal feed diameter ratio found by Rietema [1961] for heavy dispersion hydrocyclones ( $D_F/D_C\approx0.28$ ).

In heavy dispersion hydrocyclones the overflow orifice is larger than the underflow orifice because the majority of the fluid exits at the

overflow, while the solids leave through the smaller underflow orifice. For light dispersion separations this situation is reversed and most of the heavy phase exits through the underflow orifice (see Figure 71b, p.181 Bradley, 1965). For the CT-cyclone, about 90% of the feed flow rate leaves via the larger underflow orifice; the dispersion enriched stream leaves through the overflow orifice. The overflow stream is not collected by a protruding vortex finder as commonly used in heavy dispersion hydrocyclones because loss of the dispersion directly to the overflow is not detrimental to the separation efficiency; however, the absence of a vortex finder may affect the stability of the reverse flow vortex (see Chapter 5).

The use of long hydrocyclones for light dispersions was employed by Regehr [1962] more than fifteen years before the development of the CT-cyclone. The large length to diameter ratio is needed to increase drop-let residence times to offset the relatively low centrifugal forces associated with low inlet velocities. High inlet velocities (  $\geq$  8 m/s) used in the generation of large centrifugal forces tend to cause drop breakup in liquid-liquid systems (see Bohnet, 1969).

The novelty of the CT-cyclone appears to be in the use of a very fine taper angle to maintain the stability of the reverse flow vortex by conserving angular momentum over the long axial length. Colman (see Figure 18, 1981) studied the effect of the taper angle  $\beta$  on the separation performance of the CT-cyclone. The separation efficiency increased by 8% as  $\beta$  was decreased from 10° to 40°. Colman concluded that the finest taper angle resulted in the best separation; however, the overall length to diameter ratio was not fixed in these studies. It is unclear

whether the differences in performances can be attributed to a natural increase in the separation length as  $\beta$  decreases or, as conjectured by Colman, to a more favorable hydrodynamic environment for the fine taper design. Hence, Colman's work has not conclusively shown the CT-cyclone to be an improved separator compared with a more conventional single-cone design.

## 1.2. Objectives

Figure 1.1b shows the set of hydrocyclone designs consistent with design scales 1 - 6 in Figure 1.1a. The effect of the taper angles a and \$\beta\$ on the separation performance can be determined by exploring the region inside the hatched boundaries. The left boundary represents a single cone hydrocyclone with a taper of 1° (i.e.,  $\alpha = 1°$ ,  $L_0 = 0$ ) extending all the way from the cylindrical section to the underflow orifice. The upper boundary represents a zero length fine taper section (LG = 0) with a sudden contraction of 90° between the upper swirl chamber and the cylindrical underflow section. The right boundary represents a class of cyclones having a sudden 2:1 contraction in the large taper section. Various combinations of α and β are indicated by the lower boundary for which the cylindrical underflow section has a zero length. Hydrocyclones of constant volume are represented by a family of curves, two of which have been shown by the dashed line curves in Figure 1.1b. The CT-cyclone, represented by the point CT on the diagram, lies on a curve of constant volume for which  $V_{\rm H}/D_{\rm C}^3 = 3$ .

Due to the limited scope of this research, only a small subset of the possible designs shown in Figure 1.1b will be explored. Besides the CT-cyclone, two other designs will be considered. Both are single-cone hydrocyclones, denoted as SCI and SCII (SC for single cone). Figure 1.1a shows the geometric scales for these single-cone designs. The SCI-cyclone has the same upper body section as the CT-cyclone, but the large taper angle ( $\alpha = 10^{\circ}$ ) continues all the way to the underflow diameter  $D_U$ . This results in a long cylindrical section leading to the underflow orifice and essentially replaces the fine taper section of the CT-cyclone. The SCII-design ( $\alpha = \beta = 5.24^{\circ}$ ) was chosen because it has the same volume and, thereby, the same mean residence time ( $V_H/Q_F$ ) as the CT-cyclone, where  $Q_F$  denotes the feed volumetric flow rate.

Based on the foregoing discussion, the specific objectives of this study were identified as follows:

- (1) Formulate a mathematical model describing the separation of light dispersed particles in long hydrocyclones. Using hydrodynamic parameters based on available data, calculate the efficiencies of different hydrocyclone designs.
- (2) Study the effect of geometry (taper angles) on separation efficiency by experimentally determining the performances of a conventional single-cone hydrocyclone and the CT-cyclone.

A model for the separation of light dispersions is used to develop a relation between the observed underflow purity and a theoretically calculated centrifugal efficiency in Section 2.2. The model uses material balances and the concept of short circuit flows to link these two quantities. In order to calculate the centrifugal efficiency, a particle trajectory model is formulated in Chapters 3 and 4 by using specific approximations for particle-fluid interaction and fluid velocity

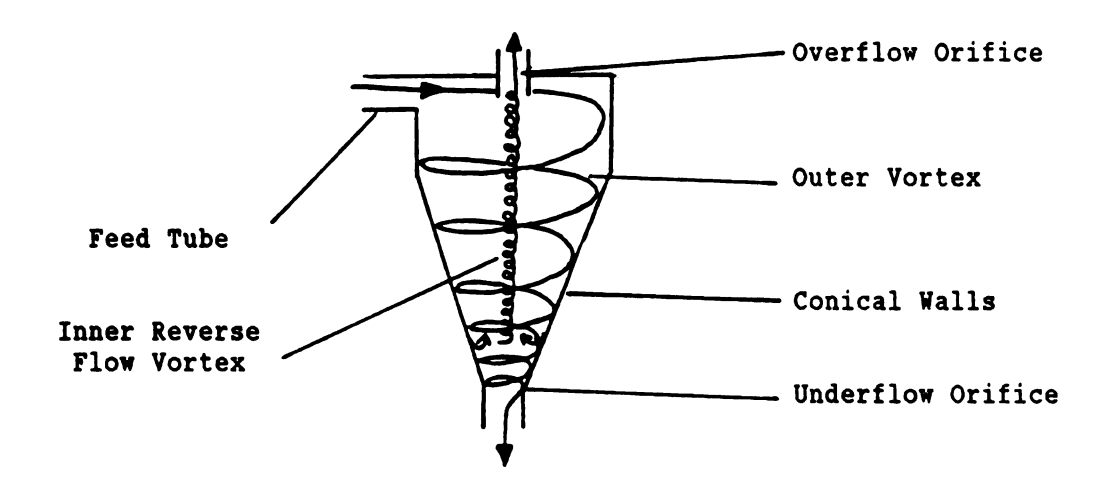
components in light dispersion hydrocyclones. Parameters which arise in the theory will be estimated by using available data for both light and heavy dispersion hydrocyclones. The separation performances of the CT-cyclone and a single-cone hydrocyclone are experimentally determined in Chapter 5 and are used to evaluate the particle trajectory model. The underflow purity results for the two designs are extrapolated to the separation of a typical oil-water dispersion using the particle trajectory model and are consistent with data presented by Colman (see Figure 18 of Colman, 1981).

### 1.3. Background

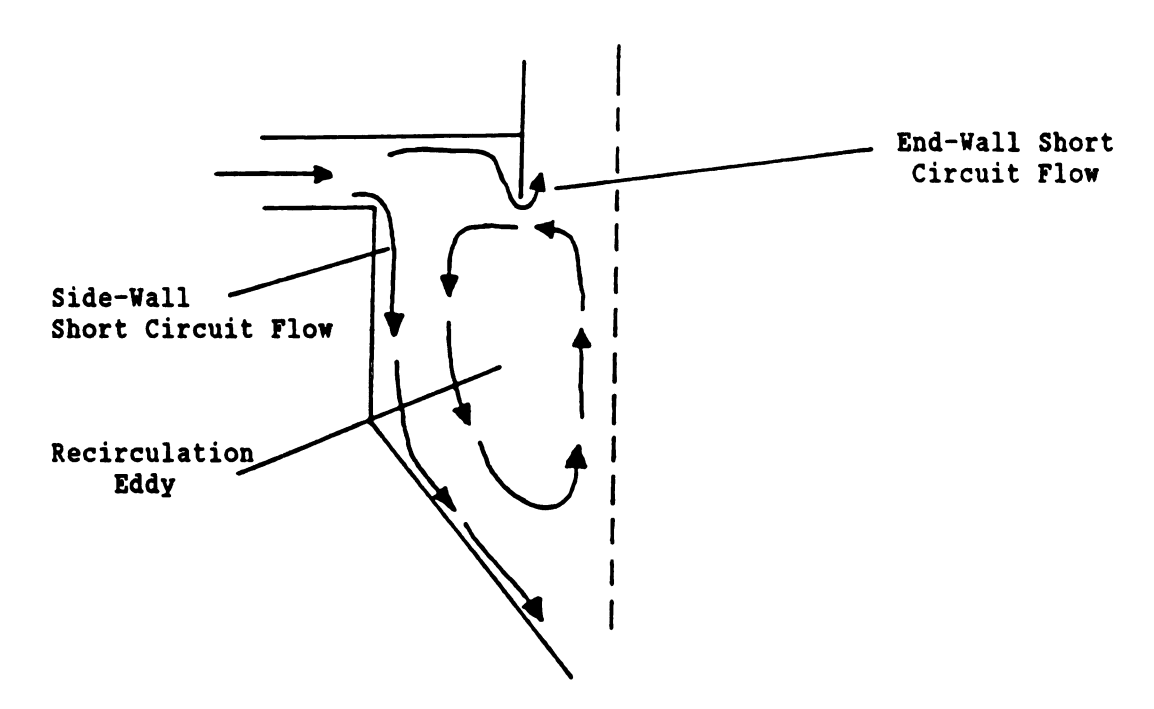
The hydrocyclone is a device that uses a centrifugal force field generated by the rotational motion of a liquid to separate materials having different properties. These properties include density, shape, size, and even magnetic field strength. The hydrocylone has also been proposed for use in the dual role of reactor and separator.

## 1.3.1. General design features

In Figure 1.2a the basic features and operation of a reverse flow hydrocyclone are shown. There are three orifices, one for each stream. The fluid enters the hydrocyclone through a tangential feed tube in the upper section and forms an outer vortex directed toward the underflow orifice. The swirl intensity increases as the hydrocyclone walls converge and fluid angular momentum is "conserved". When fluid is discharged directly to the atmosphere, the low pressures on the hydrocyclone axis may cause an air core to form. Back pressure at the underflow and/or overflow orifice can be used to eliminate the formation of an air core.



(a) Primary flow patterns in a conical hydrocyclone



(b) Secondary flow patterns in a conical hydrocyclone

Figure 1.2. Schematic of the flow patterns in a conical hydrocyclone.

At a point near the underflow orifice, a portion of the outer vortex reverses direction. An inner vortex is formed and flows along the hydrocyclone axis towards the overflow orifice. The swirl of the inner vortex is in the same tangential direction as the outer vortex. In general, a tube called the vortex finder projects down through the end wall into the hydrocyclone body to collect the inner vortex as it flows toward the overflow orifice. In some applications this vortex finder is omitted.

Figure 1.2b depicts the presence of secondary flows in the hydrocyclone. A portion of the feed flow will "short circuit" across the end wall towards the vortex finder due to a pressure gradient induced by the tangential flow. This flow continues along the vortex finder to exit in the overflow stream. Likewise, a short circuit flow can exist along the side walls that proceeds directly to the underflow orifice without experiencing centrifugal separation forces. A recirculation eddy, commonly referred to as the "mantle", exists in the upper section and prevents inward radial flow across its boundaries.

The values of the centrifugal acceleration may range from 25 to 5000 times the acceleration due to gravity. This acceleration causes heavy dispersed phase particles to experience a centrifugal ("fleeing the center") force. These particles (or droplets in the case of liquid-liquid systems) tend to migrate to the hydrocyclone walls where they are caught in a downward moving flow toward the underflow orifice. The swirling flow causes particles lighter than the continuous phase to experience a centripetal force ("toward the center"). These particles tend to migrate toward the reverse flow vortex.

### 1.3.2. Light dispersion separations in hydrocyclones

By far, most industrial applications of hydrocyclones to date have been in heavy dispersion separations. In these applications the hydrocyclone has been used as a thickener, classifier, or a washer. Many theoretical and experimental studies have been undertaken to explain the operation and flow phenomena in such hydrocyclones. Early studies by Kelsall [1952] and Bradley and Pulling [1959] describe the basic flow patterns present. Rietema [1961] provided a basis for selecting design features to optimize separation efficiency. The "optimal" hydrocyclone for solid-liquid separations included specifying the length to diameter ratio at  $L/Dc \approx 5$  and the feed diameter ratio  $D_F/Dc \approx 0.28$ . An excellent review of these and other analyses can be found in Bradley [1965] as well as Svarovsky [1984].

The hydrocyclone has also been used as a degasser and a mass transfer device. As a liquid-liquid separator, hydrocyclones have not been widely used. Most applications of hydrocyclones in the separation of light dispersions have been concerned with liquid-liquid systems.

Tepe and Woods [1943] reported the first known application in this area, attempting to separate water-alcohol mixtures in a 10 mm diameter hydrocyclone. Very low separation efficiencies on the order of 10% were reported for alcohol feed fractions of about 50% by weight. Hitchon [1959] used a similar hydrocyclone to separate kerosene-water mixtures and found that it was possible to obtain one component in pure form. Either the water could be obtained pure at the underflow for high overflow split ratios, or kerosene could be obtained pure at the overflow for low overflow split ratios. However, very high feed fractions of

the dispersed phase were used (≈ 50%), and a pure product in this sense probably contained some small impurities.

Simkin and Olney [1956] conducted separation studies for a white oil-water system in a 95 mm diameter hydrocyclone and obtained results similar to those of Hitchon. They concluded that phase separation efficiency was critically dependent on dispersed phase drop size and that poor separation resulted from moderate mixing intensities at the feed inlet. Phase separation was found to be principally a function of operating conditions and not of hydrocyclone geometry. Again, high dispersed phase feed concentrations were used.

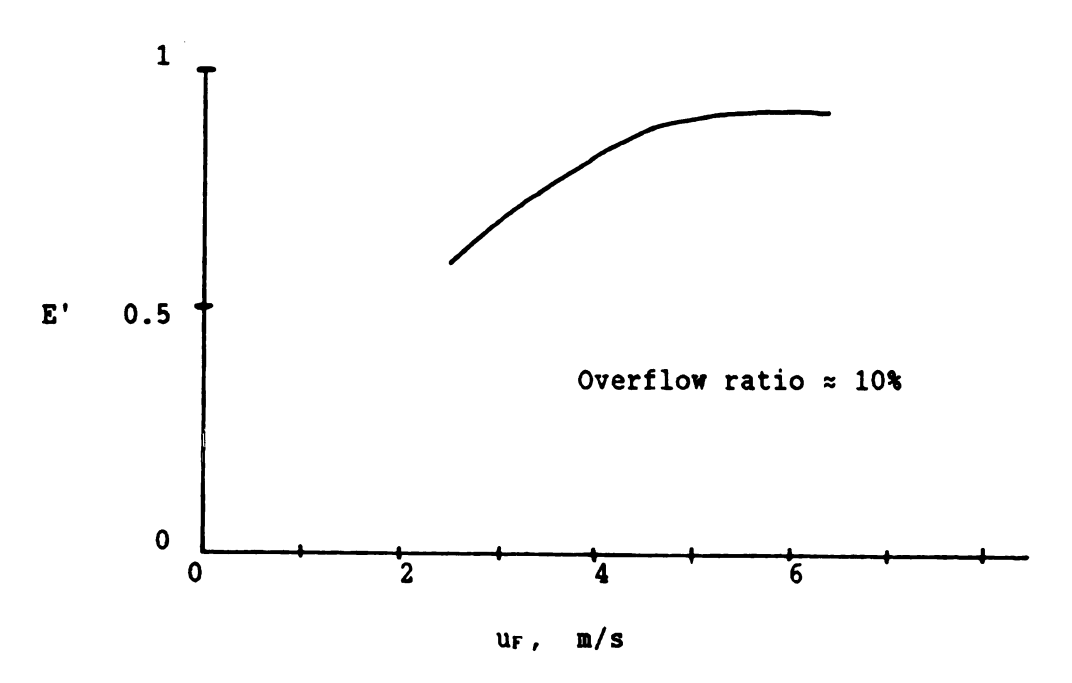
Regehr [1962] conducted the first studies of light dispersion separations using solid particles dispersed in water as a model for the liquid-liquid system. In this manner, the dispersed phase size distribution would remain fixed and the effects of hydrocyclone geometry and operating variables could be studied. The designs studied appear to be the original attempts at using long hydrocyclones (length to diameter ratio  $\geq$  10) for this application. Both reverse-flow and through-flow designs were investigated. In his study, Regehr used the underflow purity,

$$E' = 1 - y_U/y_F , \qquad (1-1)$$

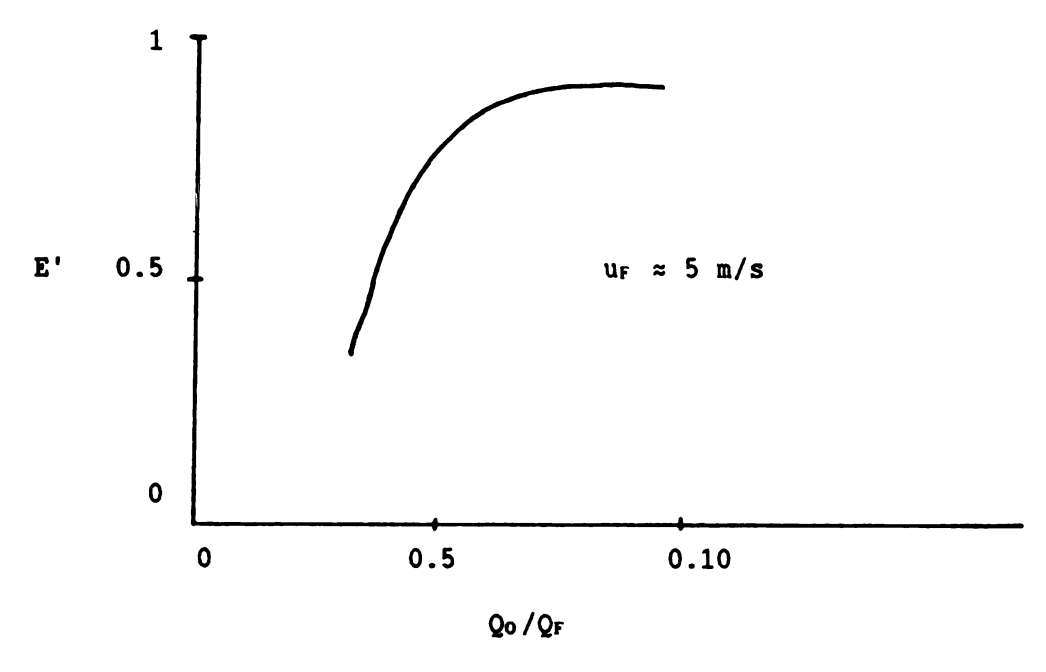
as a measure of separation efficiency. In Eq.(1-1),  $y_U$  and  $y_F$  are volume fractions of dispersed phase in the underflow and feed streams, respectively. This measure reflects the ability of the separator to remove the dispersed phase from the underflow. An efficiency of 100% is reflected by the underflow containing no dispersed phase, while an efficiency

of 0% represents the feed stream being split into streams of equal composition. Regehr found that for all hydrocyclone designs tested, the underflow purity tended to reach an asymptotic value of less than 100% as either separation length or feed velocity approached large values ( $L/D_C \geq 10$  or feed velocity  $u_F \geq 8$  m/s). This result was independent of the particle size distribution or particle-fluid density differential and indicated the presence of an inefficiency common to all the designs studied. The asymptotic value of E' as total separation length increased was interpreted by Regehr as a decay of angular momentum at the downstream end of the hydrocyclones.

Kimber and Thew [1974] conducted separation studies of oil-water mixtures in a hydrocyclone design used by Regehr [1962]. These studies were prompted by environmental concerns, and were continued by Colman [1981]. Colman conducted a series of experiments in an attempt to optimize the design of long hydrocyclones to separate very dilute mixtures of light dispersed particles. Using a combination of flow visualization, separation tests, particle size determinations, and velocity profile measurements, Colman arrived at an improved double-cone hydrocyclone design for light dispersion separations. The general behavior of the underflow purity E' as a function of inlet velocity for the CT-cyclone is shown in Figure 1.3a. The asymptotic behavior of E' is observed for both the solid-liquid studies of Regehr [1962] and Colman [1981] as well as the liquid-liquid studies of Colman and Thew [1983]. The underflow purity rises with increasing up but at a decreasing rate, up to the value of up where E' becomes asymptotic. Since this behavior exists for both solid-liquid and liquid-liquid systems, droplet breakup is not



(a) Underflow purity vs. inlet velocity.



(b) Underflow purity vs. overflow ratio

Figure 1.3. Asymptotic behavior of the underflow purity in the CT-cyclone.

likely to be the cause. Meldrum [1987] presented data for the CT-cyclone which differed from the other researchers. The underflow purity exhibited a very sharp drop-off at both low and high values of us with a constant value in between. Meldrum attributed the drop off at low inlet velocities to insufficient centrifugal forces available for separation. The decrease in E' at high inlet velocities was attributed to insufficient pressure drop across the overflow orifice. The "plateau" value of E' in these tests (from 90-95%) suggests the presence of a limiting factor such as the loss of dispersion directly to the underflow in a sidewall boundary layer.

An interesting aspect in the performance of the CT-cyclone is the relatively sharp drop in the underflow purity as the overflow ratio  $Q_0/Q_F$  decreases through a critical value. The symbols  $Q_F$  and  $Q_0$  represent, respectively, the volumetric flow rates of the feed and overflow streams. This behavior is illustrated by Figure 1.3b which shows that E' plunges quickly to zero as  $Q_0/Q_F$  decreases below .05. Colman (see p.29, 1981) attributed this phenomenon to instabilities in the reverse flow vortex as it approaches the overflow orifice. The reverse flow vortex (marked by light dispersed particles) was reported to break up as it traveled toward the overflow outlet and to remix with the incoming feed flow. This type of phenomenon was not observed in this study. Instead a sudden flow reversal of the vortex core toward the apex occurred for low overflow ratios (see Section 5.4.1).

#### CHAPTER 2

#### SEPARATION EFFICIENCY

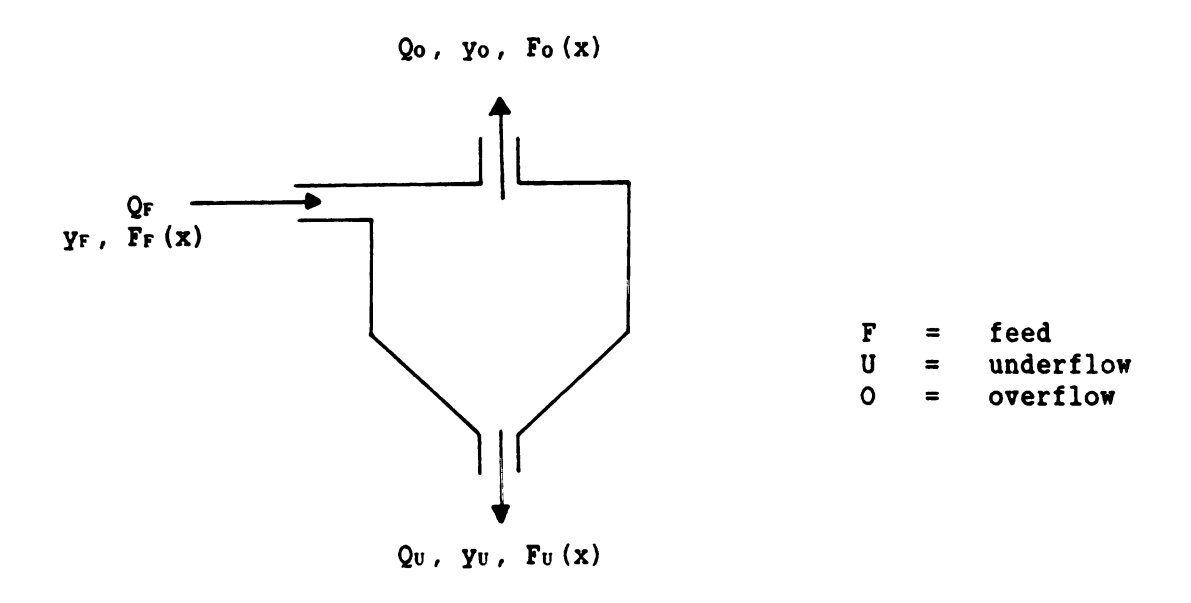
The efficiency of the CT-cyclone for separating light dispersions reaches asymptotic values less than unity even for large feed velocities (see Figure 1.3a). In this chapter a model for this phenomenon is related to the short circuit flows within the separation process. However, before this concept is developed, some performance measures will be discussed.

## 2.1. Performance Measures for Two Component Separations

The following discussion is limited to mixtures of two immiscible components for which the density of the mixture can be expressed as a linear combination of the component densities. Particles (or droplets) of the dispersed phase are assumed to have a distribution of sizes. The separation process is assumed to be at steady state, with no agglomeration or breakup of dispersed phase particles occurring in the hydrocyclone. Figure 2.1 defines the basic physical variables related by material balances.

The overall material balance can be written as a balance equation for the total volumetric flow rates using the above assumptions

$$Q_F = Q_0 + Q_U. \qquad (2-1)$$



 $Q_F$ ,  $Q_U$ , and  $Q_O$  are total volumetric flow rates  $y_F$ ,  $y_U$ , and  $y_O$  are volume fractions of the dispersed phase  $F_F(x)$ ,  $F_U(x)$ , and  $F_O(x)$  are cumulative size distributions for the dispersed phase; x represents particle diameter

Figure 2.1. Schematic for the separation of a two component mixture.

Similarly, a material balance for the dispersed phase can be written as

$$Q_F y_F = Q_O y_O + Q_U y_U . \qquad (2-2)$$

For dispersed particles in the differential size range dx, the following component equation applies

$$Q_F y_F dF_F = Q_O y_O dF_O + Q_U y_U dF_U. \qquad (2-3)$$

The term  $y_F dF_F$  represents the volume fraction of dispersed phase particles of size x in the feed stream and  $F_F(x)$  represents the cumulative size distribution.  $F_O(x)$  and  $F_U(x)$  are analogous to  $F_F(x)$  for the overflow and underflow streams, respectively.

The derivative of the cumulative size distribution F(x) is the density distribution

$$f(x) = \frac{dF}{dx} \qquad 0 \le x \le \infty . \qquad (2-4)$$

The density distribution has an infinite value when the dispersion contains particles of a single size only. A specific example for  $f_F(x)$  employed in this study is given in Appendix B.4. By definition, F(x) and f(x) satisfy the following integral property

$$\int_{0}^{1} dF = \int_{0}^{\infty} f(x) dx = 1. \qquad (2-5)$$

A grade efficiency G(x) can be defined by

Eq. (2-6) can be interpreted as the "recovery" of dispersed phase particles of size x in the overflow. Note that Eq. (2-6) can also be written as

$$G(x)Q_F y_F dF_F = Q_0 y_0 dF_0 . (2-7)$$

For very "small" particles, the separation effect due to the centrifugal force is negligible and the concentration of very fine particles in the feed stream and in the overflow stream are equal,

$$\lim_{x\to 0} (y_F dF_F) = \lim_{x\to 0} (y_O dF_O). \qquad (2-8)$$

Eqs. (2-7) and (2-8) can be combined to give

$$\lim_{x\to 0} G(x) = Q_0/Q_F = S_0. \qquad (2-9)$$

On the other hand, for "large" particles, the separation effect due to the centrifugal force is large and all of the large particles subjected to the centrifugal action will have enough time to migrate to the overflow, giving

$$\lim_{X\to\infty} (Q_F Y_F dF_F) = \lim_{X\to\infty} (Q_O Y_O dF_O). \qquad (2-10)$$

Eqs. (2-7) and (2-10) can be combined to give

$$\lim_{x \to \infty} G(x) = 1 , \qquad (2-11)$$

provided <u>all</u> of the feed stream is subjected to the centrifugal field (i.e., no short-circuit flows exist).

If the mass densities of the dispersed phase and the continuous phase are equal, then no separation occurs. In this case the concentration of the dispersed phase for any particle size equals the concentration of the feed stream,

$$\lim_{C \to C} (y_F dF_F) = \lim_{C \to C} (y_O dF_O), \qquad (2-12)$$

where  $f_c$  and  $f_D$  are the mass densities of the continuous and dispersed phases, respectively. Therefore, it follows directly from Eq. (2-7) that

$$\lim_{C \to C} G(x) = S_0. \qquad (2-13)$$

Thus, the overflow ratio So provides a lower bound on the grade efficiency for either small particles or for neutrally buoyant dispersions.

Integrating Eq. (2-7) over all particle sizes yields

$$E = \int_0^{\infty} G(x) f_F(x) dx , \qquad (2-14)$$

where the total efficiency E, or total recovery, of the light dispersed phase is defined by

$$E = \frac{Qo yo}{Q_F y_F} . \qquad (2-15)$$

Because yo ≥ yr and Qoyo ≤ Qryr, it follows directly from Eq. (2-15) that

$$S_0 \leq E \leq 1 . \tag{2-16}$$

For light dispersions it is also possible to define a grade purity G'(x) as follows

$$G'(x)y_FdF_F = (y_FdF_F - y_UdF_U). \qquad (2-17)$$

Physically, G'(x) is a measure of the separator's ability to remove a specific particle size of the dispersed phase from the underflow stream. When G'(x) = 1, the underflow contains no dispersed phase particles of size x. When G'(x) = 0, the concentration of dispersed phase of size x in the underflow equals the feed concentration of size x. Thus

$$0 \le G'(x) \le 1.$$
 (2-18)

Integrating Eq. (2-17) over all particle sizes yields

$$E' = \int_0^{\infty} G'(x) f_F(x) dx , \qquad (2-19)$$

where the total underflow purity relative to the feed stream is defined by

$$E' = (y_F - y_U)/y_F$$
 (2-20)

When E' = 1, the underflow contains no dispersion. On the other hand, when E' = 0, the underflow and feed compositions are equal.

The grade recovery G(x) and the grade purity G'(x) can be related by combining Eqs. (2-3), (2-7), and (2-17). This gives

$$G'(x) = \frac{G(x) - S_0}{1 - S_0}$$
 (2-21)

Analogously, the total recovery E and the total purity E' can be related by combining Eqs. (2-2), (2-9), and (2-20) with the result that

$$E' = \frac{E - S_0}{1 - S_0} . (2-22)$$

## 2.2. A Model for Light Dispersion Separation

Many factors affect the separation process in hydrocyclones. One of the factors, which is not unique to hydrocyclone equipment, is the possibility of short-circuit flow directly to the outlets. This factor plays a key role in the model for separation shown in Figure 2.2 which illustrates the conceptual framework of the model. The feed, characterized by  $Q_F$ ,  $y_F$ , and  $F_F(x)$ , is split into three streams. An end-wall boundary flow QEw short circuits directly to the overflow, remaining at feed conditions. A side-wall boundary flow Qsw short circuits directly to the underflow, also remaining at feed conditions. These short circuit flows are assumed to remain in relatively low centrifugal fields, with no classification/clarification taking place. The remainder of the flow, Qr - Qrw - Qrw, enters the outer vortex and is subjected to the centrifugal force field. A portion of this flow reverses direction near the underflow orifice at a volumetric flow rate Qv, composition yu\*, and particle size distribution  $F_{U}^{*}(x)$ . During the reversal, dispersed phase particles are assumed to remain entrained in the fluid. Additional particles are collected by the inner vortex from the outer vortex due to

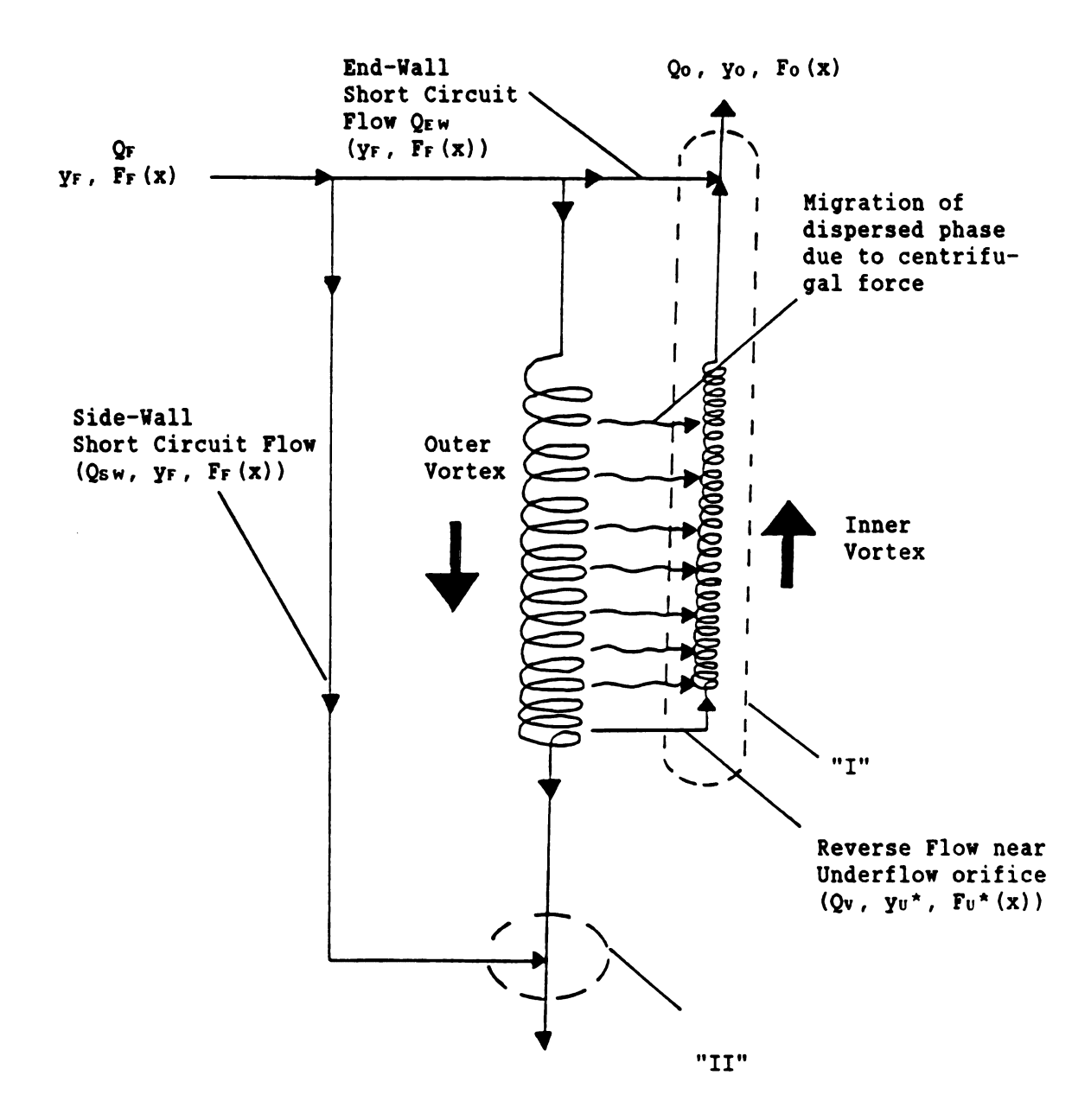


Figure 2.2. Model for light dispersion separation in a hydrocyclone.

centrifugal effects. This occurs all along the length of the reverse flow vortex during its transit toward the overflow orifice. Near the overflow orifice, this jet-like flow combines with the end-wall flow  $Q_{EW}$ , resulting in the overflow stream  $Q_0$ . Near the underflow orifice, all fluid from the outer vortex that does not reverse direction combines with the side-wall flow  $Q_{EW}$ , resulting in the underflow stream  $Q_U$ .

A dispersed phase material balance for particles in the size range dx around control surface "I" (see Figure 2.2) is

$$Q_0 y_0 dF_0 = Q_E w y_F dF_F + Q_V y_U * dF_U *$$

$$+ G_C(x) \left[ Q_F - Q_E w - Q_S w \right] y_F dF_F. \qquad (2-23)$$

Eq.(2-23) introduces the <u>centrifugal</u> grade efficiency, or recovery, defined as follows (cf. Eq.(2-6))

The internal flow rate  $Q_V$  and the term  $y_U^*dF_U^*$  can be eliminated from Eq.(2-23) by writing two additional independent material balances. The first is an overall material balance around control surface "I"

$$Q_0 = Q_{EW} + Q_V + \left[ Q_F - Q_{EW} - Q_{SW} \right] \int_0^{\infty} G_C(x) f_F(x) dx.$$
 (2-25)

The second equation is a dispersed phase material balance for particles in the size range dx over control surface "II"

$$Q_{U} y_{U} dF_{U} = Q_{SW} y_{F} dF_{F} + (Q_{U} - Q_{SW}) y_{U} * dF_{U} * . \qquad (2-26)$$

The centrifugal efficiency, or recovery, is defined by

$$E_{C} = \int_{0}^{\infty} G_{C}(x) f_{F}(x) dx , \qquad (2-27)$$

so Eq. (2-25) can be rewritten as

$$Q_0 = Q_E w + Q_V + (Q_F - Q_E w - Q_S w) y_F E_C$$
 (2-28)

Eqs.(2-26) and (2-28) can be solved for  $y_0*dF_0*$  and  $Q_V$  respectively, and the resulting expressions substituted into Eq.(2-23). The resulting equation can be combined with Eqs.(2-1) and (2-7) and integrated over the dispersed phase particle size range. Upon rearrangement, the following expression for E results

$$E = \frac{S_0 + (1 - S_{SW} - S_0 - (1 - S_{SW}) y_F) E_C}{1 - y_F E_C}, \qquad (2-29)$$

where

$$S_{SW} \equiv Q_{SW}/Q_F$$
 (2-30)

Eq. (2-29) is an important result, linking the total efficiency E to the centrifugal efficiency E<sub>c</sub>. Upper and lower bounds on E follow directly from Eq. (2-29). For instance,

$$\lim_{E_C \to 0} E = S_0 ; \qquad (2-31)$$

and,

$$\lim_{E_{C} \to 1} E = 1 - S_{SW}. \qquad (2-32)$$

Eq. (2-31) is the same lower bound on E as given by Eq. (2-16). Eq. (2-32) shows that the side-wall flow is indeed a limiting factor for the recovery of light dispersed phase into the overflow stream. This limiting behavior is only reached as the centrifugal efficiency approaches its maximum value of unity, which occurs for large feed velocities or for large particle sizes.

Combining Eq. (2-22) with Eq. (2-29) and solving for E' gives

$$E' = \frac{(1 - y_F)(1 - S_0 - S_{SW})E_C}{(1 - y_F E_C)(1 - S_0)}.$$
 (2-33)

The limiting behavior for E' follows directly from Eq. (2-33):

$$\lim_{\mathbf{E}_{\mathbf{C}} \to \mathbf{0}} \mathbf{E}' = \mathbf{0} ; \qquad (2-34)$$

and,

$$\lim_{E \to 1} E' = 1 - S_{8W}/(1 - S_0)$$
. (2-35)

Eq. (2-34) is the result of the separator acting as a flow splitter.

Eq. (2-35) can be used to interpret the asymptotic value of the underflow purity E' at high feed velocities reported by Regehr [1962], Colman [1981], and Meldrum [1987] (see Figure 1.3a). Similar to Eq. (2-32), Eq. (2-35) presents an upper bound on the underflow purity, reflecting the loss of dispersed phase particles from the feed directly to the underflow.

$$E' = \left[ 1 - S_{8W}/(1 - S_0) \right] E_C .$$
 (2-36)

For nonzero values of  $S_{SW}$ ,  $E' \leq E_C$ . From Eq.(2-36) it would be possible to estimate the value of  $S_{SW}$  using experimental data for E' and  $S_O$  under conditions for which  $E_C$  is approximately unity (i.e., large particle sizes or large density differences). Also, if experimental data for E',  $S_O$ , and  $S_{SW}$  were available, then a theory for calculating  $E_C$  could be evaluated.

When  $S_{SW} = 0$  and  $y_F \ll 1$ , Eq.(2-33) reduces to

$$\mathbf{E'} = \mathbf{E_C} . \tag{2-37}$$

The approximation given by Eq. (2-37) is important because it provides a direct comparison between a quantity that is experimentally observed (E') and a quantity that can be theoretically calculated  $(E_C)$ .

The existence of the upper bound on the underflow purity due to the side-wall short circuit flow Q<sub>SW</sub> (see Eq.(2-35)) suggests that further improvements in underflow purity may be realized by somehow reintroducing particles "trapped" in the side-wall boundary layer back into the outer wortex. Fontein et al.(see p. 121 Bradley, 1965) showed that for heavy dispersion separations, roughening of the hydrocyclone walls led to an increased throughput at the same pressure drop, but also resulted in an decreased efficiency. This was due to heavy particles from the side-wall boundary layer being reentrained into the upward moving vortex and contaminating the overflow stream. For light dispersion separations this effect may be advantageous. Colman [1981] studied the

effect of roughened walls in the cylindrical section at the inlet end of a light dispersion hydrocyclone and concluded that the underflow purity decreased as a result of the roughening. However, this may have been due to lower tangential velocities resulting from wall friction. It may be possible to disturb the side wall boundary layer by roughening the side wall nearer to the underflow orifice. This strategy could reintroduce "trapped" particles back into the outer vortex and not disturb the centrifugal force field.

Another possibility of reintroducing particles into the outer vortex is through hydraulic water addition. The concept of side-wall boundary layer manipulation to achieve higher classification efficiencies has been applied to hydrocyclones for classification of heavy dispersions.

Dahlstrom [1952] used hydraulic water addition near the underflow orifice to displace water containing fine particles away from the side-wall boundary layer. The hydraulically added water was injected tangentially at an axial level above the point of fluid reversal. The displaced fluid carried the fine particles to the overflow via the reverse flow vortex. The hydraulically added water reported to the underflow with the coarse solids. The amount of hydraulically added water could not exceed the amount of water normally reporting to the underflow because then coarse particles also reported to the overflow. This was caused by disruption of flow patterns near the underflow orifice.

The use of hydraulic water addition appears to be suited to the reintroduction of light dispersed particles trapped in the side-wall flow back into the outer vortex. The main mechanism for the capture of these displaced particles into the reverse flow vortex would probably

be centrifugal action and not entrainment with the fluid experiencing flow reversal because of the generally low overflow ratios used in light dispersion separations ( $S_0 \le 0.10$ ). Hydraulic water addition would need to be conducted at an axial level far enough displaced from the underflow orifice to allow sufficient time for particles to be centrifugally separated.

# 2.3. The Relationship Between Centrifugal Grade Efficiency and Particle Trajectories

The centrifugal efficiency  $E_C$  is related to the centrifugal grade efficiency by Eq.(2-27). For a given dispersion, the feed size density distribution  $f_F(x)$  can be determined experimentally (see Appendix B.4). To calculate the centrifugal efficiency, the centrifugal grade efficiency  $G_C(x)$  must be determined. A model for particle-fluid interaction can be combined with approximations for the fluid velocity components to give particle trajectories in a hydrocyclone. Figure 2.3 illustrates the relationship of the critical trajectory for a given particle and the centrifugal grade efficiency referred to in Section 2.2.

The critical trajectory is defined as the locus of coordinates connecting the initial and final coordinates for a particle of diameter x. The final coordinates indicate that the particle has just reached the capture surface radius  $\hat{r_v}$  as it exits the underflow orifice. The particle is then assumed to be caught in the upward moving reverse flow vortex. In Figure 2.4,  $\hat{r}$  and  $\hat{z}$  are the radial and axial coordinates, respectively. The coordinate origin is at the intersection of the hydrocyclone axis and the end wall. The bounds of the coordinate system are  $0 \le \hat{r} \le \hat{r_w}(z)$  and  $0 \le \hat{z} \le \hat{L}$ . The variable  $\hat{r_w}(z)$  denotes the

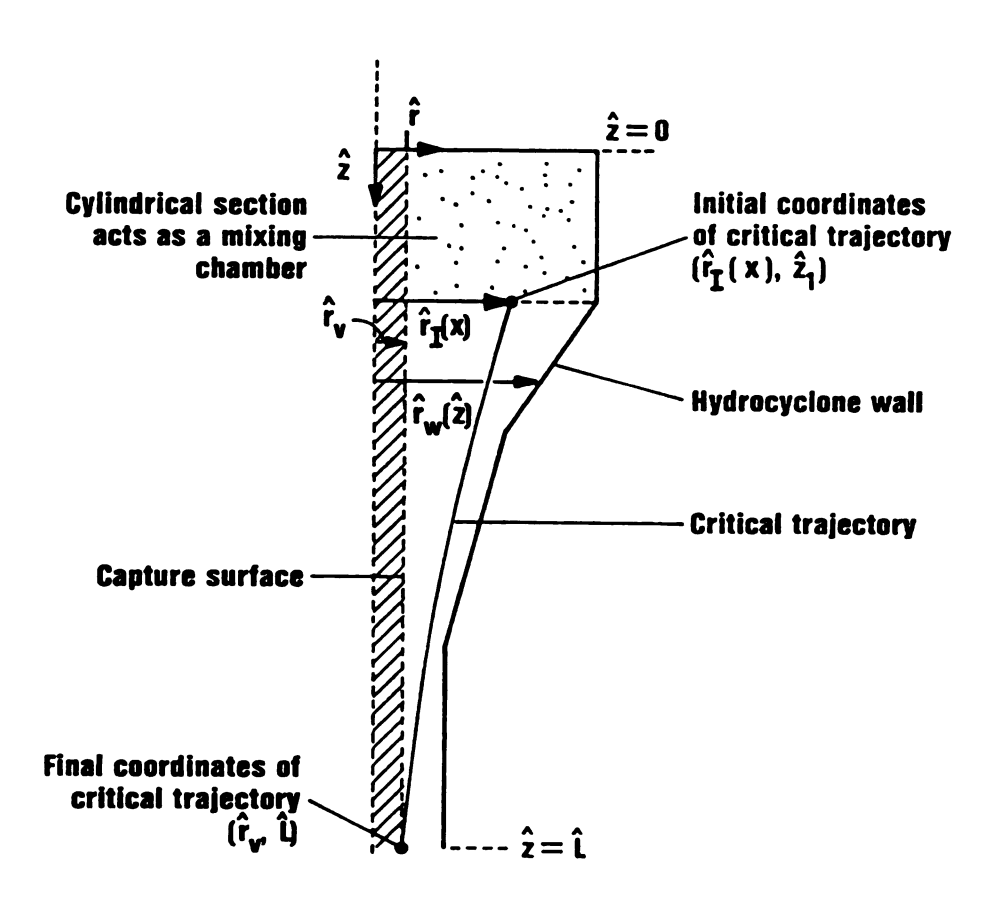


Figure 2.3. Critical trajectory for a light dispersed phase particle.

hydrocyclone wall radial coordinate,  $\hat{r}_c$  indicates the wall radius in the upper cylindrical section, and  $\hat{L}$  is the overall length. The cylindrical section of the hydrocyclone near the inlet end is assumed to act as a mixing chamber (see p.81 Bradley, 1965). Dispersed particles entering the hydrocyclone are homogeneously distributed within the the boundaries  $\hat{r}_v \leq \hat{r} \leq \hat{r}_c$  and  $0 \leq \hat{z} \leq \hat{z}_1$ . Because the upper cylindrical section is assumed to act as a mixing chamber, no separation occurs there. In the calculation of a trajectory, a particle is given an initial axial coordinate  $\hat{z}_1 = \hat{z}_1$ . The capture surface for a particle is taken to be a cylinder of radius  $\hat{r}_v$ , corresponding to the radius of the reverse flow vortex which runs the length of the hydrocyclone axis. This concept has been verified by visual observation of the reverse flow particle core in this research and in Colman [1981].

The centrifugal grade efficiency,  $G_C(x)$ , as defined by Eq.(2-25) can be expressed as

$$G_{C}(x) = \frac{u_{2}\pi(\hat{r}_{1}^{2}(x) - \hat{r}_{v}^{2})y_{F}dF_{F}}{u_{2}\pi(\hat{r}_{C}^{2}(x) - \hat{r}_{v}^{2})y_{F}dF_{F}}, \qquad (2-38)$$

where  $u_z$  is the plug flow velocity assumed to exist in the cylindrical "swirl chamber" (see Figure 2.4). The numerator of Eq.(2-38) represents the volumetric flow rate of particles of size x that will report to the underflow, because they start inside the initial radial coordinate  $\hat{r}_I(x)$  of the critical trajectory. The denominator represents the total volumetric flow rate of particles of size x entering with the feed. Eq.(2-38) can be simplified to give

$$G_{C}(x) = \frac{\hat{r}_{1}^{2}(x) - \hat{r}_{v}^{2}}{\hat{r}_{C}^{2} - \hat{r}_{v}^{2}}.$$
 (2-39)

Eq.(2-39) is the link between the initial radial coordinate for the critical trajectory of a particle of size x and the centrifugal grade efficiency. This relationship is independent of any hydrodynamic model for the velocity components of the continuous phase or any model for particle-fluid interaction.

#### CHAPTER 3

# PARTICLE - FLUID INTERACTION AND HYDRODYNAMICS

## 3.1. The Particle Trajectory Model

Evaluation of the centrifugal grade efficiency requires knowledge of the initial radial coordinate  $r_1(x)$  in the critical trajectory for a particle of diameter x (see Eq.2-39). In the following theory for the trajectory of a light dispersed particle, the axial and tangential velocities of the particle are taken to be the same as the surrounding fluid. The radial velocity of the particle is less than the fluid radial velocity (i.e., more negative than the fluid radial velocity) because of the inwardly directed centripetal forces acting on the light dispersed phase. A radial force balance on the particle which equates the viscous drag and the centrifugal forces at all points in the flow field (see p.354 Hinze, 1959), gives

$$(\pi x^3/6) (\varphi_c - \varphi_b) (u_{\theta^2}/\hat{r}) = C_D (\pi x^2/4) \% \varphi_c (u_r - u_{rp})^2.$$
 (3-1)

The particle is represented by the diameter x and the density  $\mathcal{L}_D$ ; the fluid has a density of  $\mathcal{L}_C$ . The radial velocity of the particle with respect to a fixed frame of reference is denoted by  $u_{rp}$ , and the radial and tangential components of the fluid velocity are given as  $u_r$  and  $u_\theta$ , respectively. The symbol  $C_D$  represents the drag coefficient for the particle. The force balance indicated by Eq. (3-1) represents a

quasi-steady state in which acceleration times for the particles are small in comparison to the residence time in the hydrocyclone (see p.7 Svarovsky, 1984).

The term on the left hand side of Eq.(3-1) represents the centripetal force acting on the light dispersed particle. This force is a combination of the centrifugal acceleration acting on the particle as well as on the surrounding fluid, causing a radial pressure gradient in the fluid surrounding the particle. The term on the right hand side of Eq.(3-1) is the steady state contribution to the viscous drag for which the drag coefficient can be represented by expressions in three different flow regimes (see p.193-4, Bird et al.(1960));

$$\frac{C_{D}^{\circ}}{C_{D}} = \begin{cases} 1 & , & 0 \leq Re_{P} \leq 2 & Stokes' & (3-2a) \\ & & Law \end{cases}$$

$$1.3 Re_{P}^{-2/5}, & 2 \leq Re_{P} \leq 500 & Transition & (3-2b) \\ & & Regime \end{cases}$$

$$54.5 Re_{P}^{-1}, & 500 \leq Re_{P} \leq 2 \times 10^{5} & Newton's . & (3-2c) \\ Law \end{cases}$$

The following definitions apply in Eqs. (3-2a) - (3-2c):

$$C_D^* = 24/Re_P , \qquad (3-3)$$

and

$$Re_{p} = \frac{x | u_{r} - u_{rp}|}{v_{c}} . \qquad (3-4)$$

Eq.(3-3) is Stokes' law for particle drag on a sphere and Eq.(3-4) is a definition for the particle Reynolds number, with  $V_C$  denoting the

kinematic viscosity of the continuous phase. The effects of turbulence, particle-particle interactions, and the lift force (see Bouchillon, 1963) are not included in Eq.(3-1).

The trajectory of a light dispersed phase particle can be expressed by two ordinary differential equations by combining Eqs.(3-1) - (3-4) and by using the assumption of no slip between particle and fluid in the axial direction. The result is

$$\frac{d\hat{\mathbf{r}}_{p}}{dt} = \mathbf{u}_{r} - \tau_{c} \left(\mathbf{u}e^{2}/\hat{\mathbf{r}}_{p}\right) \mathbf{W} , \qquad (3-5)$$

$$\frac{d\hat{Z}_p}{dt} = u_z , \qquad (3-6)$$

where

$$\frac{d\hat{\mathbf{r}}_{p}}{dt} = \mathbf{u}_{rp} , \qquad (3-7)$$

and

$$W = C_D^{\circ}/C_D . \qquad (3-8)$$

The variables  $\hat{r}_P$  and  $\hat{z}_P$  represent, respectively, the radial and axial coordinates of the particle, while t represents the independent variable time. The axial velocity of the particle/fluid is given by  $u_Z$ , and  $\tau_C$  is a time scale characteristic of the dispersion parameters defined by

$$\tau_{\rm c} = \frac{{\bf x}^2 (1 - \rho_{\rm D}/\rho_{\rm c})}{18 \nu_{\rm c}}$$
 (3-9)

In order to calculate the particle trajectory given by Eqs.(3-5) and (3-6), the local magnitude of the axial, radial, and tangential velocities must be modelled. In Eqs.(3-5) and (3-6), the velocities are evaluated at  $\hat{r}_p$  and  $\hat{z}_p$ .

## 3.2. Hydrodynamics

## 3.2.1 Axial Velocity

The axial velocity of the continuous phase will be represented by a plug flow which changes with the cross sectional area as follows

$$u_z = \frac{Qc}{(\hat{r}_w^2 - \hat{r}_v^2)}, \qquad (3-10)$$

where

$$Q_C = Q_F - Q_{SW} - Q_{EW}$$
 (3-11)

Qc represents the portion of the feed available for centrifugal separation (see Figure 2.2). The denominator represents the cross sectional area available for flow toward the underflow orifice (see Figure 2.3). This model for the axial velocity qualitatively describes the axial velocity profile in the outer vortex region for light dispersion hydrocyclones (see Figure 6, Colman et al., 1984).

## 3.2.2 Radial Velocity

The radial velocity of the continuous phase is derived from the axial velocity using the continuity equation for an incompressible fluid. By assuming the flow field to be axisymmetric and the radial velocity of the continuous phase to be zero at the radius  $\hat{\mathbf{r}}_{\mathbf{v}}$  of the inner vortex, the radial velocity  $\mathbf{u}_{\mathbf{r}}$  follows directly from the continuity equation and can be written as

$$u_r = -\frac{(\hat{r}^2 - \hat{r}_{v^2})}{2\hat{r}} \frac{\partial u_z}{\partial \hat{z}}. \qquad (3-12)$$

The assumption of a zero radial velocity at  $r = r_v$  corresponds to a

reverse flow vortex that does not entrain fluid as it flows toward the overflow orifice (see Section 2.3). Substituting Eq.(3-10) into Eq.(3-12) and simplifying gives

$$u_{r} = Q_{c} \frac{\hat{r}_{w}(\hat{r}^{2} - \hat{r}_{v^{2}})}{\hat{r}(\hat{r}_{w}^{2} - \hat{r}_{v^{2}})^{2}} \frac{d\hat{r}_{w}}{d\hat{z}}.$$
 (3-13)

The velocity profile given by Eq.(3-12) has a maximum inward radial velocity at the wall, decreasing to zero at the inner radius  $\hat{r}_v$ . This is consistent with the radial velocity profiles observed by Kelsall [1952] in a conical hydrocyclone. The radial velocity given by Eq.(3-12) will be zero for all values of r in the cylindrical sections of the hydrocyclone. The slope of the wall,  $d\hat{r}_w/d\hat{z}$ , can be related to the taper angle  $\phi$  in the conical regions by

$$\frac{d\hat{\mathbf{r}}_{w}}{d\hat{\mathbf{z}}} = -\tan \phi . \qquad (3-14)$$

## 3.2.3 Tangential Velocity

The tangential velocity of the continuous phase is modelled by a combination of a forced vortex in the core region and a free-like vortex in the outer region . The forced vortex extends from the hydrocyclone axis to  $\hat{\mathbf{r}} = \hat{\mathbf{r}}_0$ , the radius at which the tangential velocity  $\mathbf{u}_0$  takes on a maximum value. The free-like vortex then extends from  $\hat{\mathbf{r}} = \hat{\mathbf{r}}_0$  to the edge of the wall boundary layer,  $\hat{\mathbf{r}} \approx \hat{\mathbf{r}}_w$ . Dabir [1983] measured velocity profiles at several axial positions in an optimal Rietema hydrocyclone using laser doppler anemometry (LDA). The tangential velocity profile was found to be both axisymmetric and largely independent of axial position. These results suggest that the tangential velocity can be represented as a function of radial position only, i.e.

$$u_{\theta} = \mathbf{m}u_{F} \begin{cases} \frac{\hat{\mathbf{r}}}{\hat{\mathbf{r}}_{c}} \frac{\hat{\mathbf{r}}_{c}^{n+1}}{\hat{\mathbf{r}}_{c}} & 0 \leq \hat{\mathbf{r}} \leq \hat{\mathbf{r}}_{\theta} \\ \frac{\hat{\mathbf{r}}_{c}^{n}}{\hat{\mathbf{r}}^{n}} & \hat{\mathbf{r}}_{\theta} \leq \hat{\mathbf{r}} \leq \hat{\mathbf{r}}_{w}(z) , \qquad (3-15b) \end{cases}$$

where m is defined by

$$u_{\theta} = mu_{F}$$
 (3-15)

The parameter m represents the fraction of the bulk average velocity (u<sub>F</sub>) in the feed tube that contributes to the tangential velocity at the wall radius  $\hat{r}_c$ . The variable n is the power index for the free-like vortex. For a free vortex, n = 1. The values of  $\hat{r}_0$ , m, and n are taken to be constants, independent of position and flow field Reynolds number. Eqs.(3-15a) and (3-15b) imply that angular momentum is conserved throughout the axial length of the hydrocyclone. Although Dabir [1983] has shown this to be approximately true for the Rietema design, flow visualization studies by Regehr [1962] showed that decay of angular momentum occurred at downstream positions in long cylindrical hydrocyclones due to wall friction. Because detailed data for the values of n or re does not exist for the CT-, SCI-, and SCII-cyclones, the decay of angular momentum will be accounted for in this study by using a low to intermediate value for n compared to values found in shorter hydrocyclones. The studies of Dabir [1983] and others indicate that a value of n from 0.6 - 0.7 is typical for hydrocyclones used in solid-liquid separation and so a value of n = 0.5 will be used in the initial trajectory calculations in this study.

The studies of Dabir [1983] also suggest that the value of recorresponds to about one half the radius of the largest withdrawal orifice. For light dispersion hydrocyclones, this would correspond to half the radius of the underflow orifice. Laser doppler anemometry (LDA) studies by Colman (see Figure 36 Colman, 1981) on a long cylindrical hydrocyclone design confirmed this value of  $\hat{r}_e$ . A single tangential velocity profile was also given for the CT-cyclone (see Figure 45 Colman, 1981), indicating that  $\hat{r}_e$  may be as small as one-fourth the underflow radius. However, this value was reported only at one axial position.

Bradley (see p.21, 1965) has reviewed the use of the parameter m and suggests a range of 0.4 - 0.8 for most applications. The tangential velocity profile reported by Colman [1981] for the CT-cyclone indicated a value of m  $\approx$  0.5.

Values of n = 0.5,  $\hat{r}_0 = \hat{r}_u/2$ , and m = 0.5 will be used to represent the hydrodynamic environment for light dispersion hydrocyclones in the exploratory particle trajectory calculations presented in Chapter 4.

Using Eqs.(3-15a) and (3-15b), the radial acceleration  $u_0^2/\hat{r}$  can be expressed in dimensionless form as

$$F_{C} = \begin{cases} \frac{r}{r_{e}^{2n+2}} & 0 \le r \le r_{e} \\ r^{-(2n+1)} & r_{e} \le r \le r_{w} \end{cases}$$
 (3-16a)

where

$$F_{C} = \frac{\left(u_{0}^{2}/\hat{r}\right)}{\left(mu_{F}\right)^{2}/\hat{r}_{C}}, \qquad (3-17)$$

and

$$r = \hat{r}/\hat{r}_c . \qquad (3-18)$$

#### CHAPTER 4

## PARTICLE TRAJECTORY CALCULATIONS

# 4.1. Particle Trajectory Analysis

4.1.1. Nondimensionalization of the particle trajectory equation

The time rate of change of particle radial position may be expressed by using the chain rule, i.e.

$$\frac{d\hat{\mathbf{r}}_{p}}{dt} = \frac{d\hat{\mathbf{r}}_{p}}{d\hat{\mathbf{z}}_{p}} \frac{d\hat{\mathbf{z}}_{p}}{dt} = u_{z} \frac{d\hat{\mathbf{r}}_{p}}{d\hat{\mathbf{z}}_{p}}, \qquad (4-1)$$

where  $\hat{r}_P$  denotes the particle radial position. Because Eqs.(3-5) and (3-6) are autonomous, the particle trajectory may be described by combining Eqs.(3-5), (3-6), and (4-1) and solving for  $\hat{dr}_P/d\hat{z}_P$ , giving

$$\frac{d\hat{\mathbf{r}}_{p}}{d\hat{\mathbf{z}}_{p}} = \frac{\mathbf{u}_{r}}{\mathbf{u}_{z}} - \frac{\mathbf{u}_{c}}{\mathbf{u}_{z}} \frac{\mathbf{u}_{e}^{2}}{\hat{\mathbf{r}}_{p}} \mathbf{W} , \qquad (4-2)$$

where

$$u_c = \tau_c (mu_F)^2 / r_c$$
 (4-3)

The symbol  $u_C$  represents a characteristic radial velocity of a particle at the hydrocylone wall radius  $\hat{r}_C$ . Eqs.(3-9), (3-12), and (4-2) can be combined to give

$$\frac{dr}{dz} = \frac{r_W (r^2 - r_V^2)}{r (r_W^2 - r_V^2)^2} \frac{dr_W}{dz} - N_1 (r_W^2 - r_V^2) F_C W , \qquad (4-4)$$

where

$$r = r_p/r_c , \qquad (4-5)$$

$$z = \hat{z}_p / \hat{L} , \qquad (4-6)$$

$$N_1 = T_2/T_R , \qquad (4-7)$$

$$\tau_Z = \frac{\hat{L}}{\Lambda} \frac{\hat{r}_C}{u_F q_C (\hat{r}_F / \hat{r}_C)^2}, \qquad (4-8)$$

$$T_{R} = \hat{r}_{c}/u_{c}, \qquad (4-9)$$

and

$$q_C = Q_C/Q_F . (4-10)$$

All radial and axial variables have been nondimensionalized as in Eqs.(4-5) and (4-6). Note that the symbol  $\hat{L}$  replaces the symbol L used in Figure 1.1a. The dimensionless group  $N_1$  is a ratio of the axial residence time  $\tau_Z$  to the radial separation time  $\tau_R$ . Also, the symbol  $q_C$  represents the fraction of the feed volumetric flow rate which experiences centrifugal separation forces.

Eq.(4-4) represents the trajectory equation for a light dispersed phase particle in the hydrocyclone, valid for  $r_V \le r \le r_W$  and  $z_1 \le z \le 1$ . The motion of a particle in the r-z plane is controlled by two effects. The first is a convective transport effect due to the radial velocity of the fluid induced by the wall taper and is reflected in the first term on the right hand side of Eq.(4-4). This term depends on the geometric parameters shown in Figure 1.1a and the capture surface radius  $r_V$  (see Figure 2.3). The second effect is due to the relative motion of the particle through the fluid (the drift velocity) caused by centrifugal force and this effect is reflected in the second term on the right hand side of Eq.(4-4). For a fixed set of geometric and hydrodynamic parameters, the trajectory is governed by the dimensionless group

N<sub>1</sub> and the particle Reynolds number Rep.

A typical value for  $\tau_Z$  can be estimated using  $\hat{L}=1.5m$ ,  $r_F=1/4$ ,  $q_C=1$  (no short circuit flows), and  $u_F=5$  m/s in Eq.(4-8), giving a value of  $\tau_Z=4.8$  seconds. A value for  $\tau_R$  can be estimated be combining Eqs.(3-8), (4-3), and (4-9), giving

$$\tau_{R} = \frac{18 \, \gamma_{C} (\mathring{r}_{C}/x)^{2}}{(1 - \mathring{r}_{D}/\mathring{r}_{C}) (mu_{F})^{2}}.$$
 (4-11)

For 100 micron oil droplets dispersed in water at  $20^{\circ c}$  ( $f_c = 1 \text{ g/cm}^3$ ,  $f_0 = 0.9 \text{ g/cm}^3$ , and  $f_0 = 10^{-6} \text{m}^2/\text{s}$ ) and fed to a 76 mm diamter hydrocyclone at  $f_0 = 5 \text{ m/s}$ , application of Eq.(4-11) gives  $f_0 = 1.04 \text{ seconds}$ . Because  $f_0 < f_2$ , these particles may be expected to be captured by the reverse flow vortex and separated into the overflow stream. In this example,  $f_0 = 1.04 \text{ seconds}$  and is much larger than  $f_0 = 1.04 \text{ seconds}$  and  $f_0 = 1.04 \text{ seconds}$  and is much larger than  $f_0 = 1.04 \text{ seconds}$ . Thus, large values of  $f_0 = 1.04 \text{ seconds}$  and is much larger than  $f_0 = 1.04 \text{ seconds}$  and  $f_0 = 1.04 \text{ seconds}$  and is much larger than  $f_0 = 1.04 \text{ seconds}$  and  $f_0 = 1.04 \text{ seconds}$  and is much larger than  $f_0 = 1.04 \text{ seconds}$  and  $f_0 = 1.04 \text{ seconds}$  and is much larger than  $f_0 = 1.04 \text{ seconds}$  and  $f_0 = 1.04 \text{ seconds}$  and is much larger than  $f_0 = 1.04 \text{ seconds}$  and is much larger than  $f_0 = 1.04 \text{ seconds}$  and  $f_0 = 1.04 \text{ seconds}$  and is much larger than  $f_0 = 1.04 \text{ seconds}$  and is much larger than  $f_0 = 1.04 \text{ seconds}$  and  $f_0 = 1.04 \text{ seconds}$  and is much larger than  $f_0 = 1.04 \text{ seconds}$  and  $f_0 = 1.04 \text{ seconds}$  and is much larger than  $f_0 = 1.04 \text{ seconds}$  and  $f_0 = 1.04$ 

## 4.1.2. Solution Strategy

Because the term  $N_1$  (  $rw^2 - rv^2$ )  $F_CW$  is always greater than or or equal to zero, Eq.(4-4) can be rewritten as the following inequality

$$\frac{dr}{dz} | \leq \frac{drw}{dz} | . \qquad (4-12)$$

$$dz rw dz rw$$

Ineq.(4-13) implies that a particle trajectory is always bounded by the hydrocyclone wall, a result of the inward radial velocity of the fluid in the conical sections.

Eq.(4-4) can be coupled with the initial condition  $r(z_1) = r_1$  to form an initial value problem. To describe the trajectory of a particle, it is necessary to integrate Eq.(4-4). The particle Reynolds number Repmust be known to calculate the drag ratio W at each step in the integration (see Eqs.(3-2a) - (3-2c)). Eqs.(3-2a) - (3-2c), (3-4), and (3-8) can be combined to give

$$Re_{p} = N_{1} N_{2} F_{C} W (Re_{p}) , \qquad (4-13)$$

where

$$N_2 = q_C (\hat{r}_F / \hat{r}_C)^2 \frac{x_{UF}}{v_C} \frac{\hat{r}_C}{\lambda}. \qquad (4-14)$$

Eqs.(3-16a) and (3-16b) define the quantity  $F_C$ . The product  $N_1\,N_2$  represents a Reynolds number based on the particle size and the radial velocity  $u_C$ , i.e.

$$N_1 N_2 = x uc/vc , \qquad (4-15)$$

The value of Rep which satisfies Eq.(4-14) for given values of  $N_1$ ,  $N_2$ ,  $r_0$ , n, and  $r_V$  is found by substituting Eqs.(3-2a) - (3-2c) into Eq.(4-14) and solving analytically for  $Re_P$  in each flow regime.

To solve the initial value problem defining a particle trajectory, the dimensionless groups representing the hydrocyclone geometry, hydrodynamics, and dispersion properties must be specified. The critical trajectory for a particle, discussed in Section 2.3, can be expressed by setting  $z_1 = 1$  at  $r_1 = rv$ . Eq.(4-4) can be integrated backward from this point to the axial position denoting the end of the swirl chamber ( $z = z_1$ ). This will result in a value for the initial radial coordinate  $r_1(x)$ , allowing evaluation of Eq.(2-39) to find the centrifugal grade

efficiency  $G_c(x)$ .

When calculating a particle trajectory in a given design, the geometric groups introduced in Figure 1.1a will be fixed. Table 4.1 lists the remaining dimensionless groups to be specified in order to calculate particle trajectories. Note that some of the parameters appear in both  $N_1$  and  $N_2$ . The geometric scales  $\hat{L}/\hat{r}_C$  and  $\hat{r}_F/\hat{r}_C$  are the same values presented in Figure 1.1a and the density ratio  $f_D/f_C$  describes the dispersion used for the separation tests in Section 5.4. The values of n, re, and m listed in Table 4.1 were discussed in Section 3.2.3. The kinematic viscosity is the value for water at  $20^{oc}$ , and the value  $q_C = 1$  indicates that no short circuit flows are accounted for. As discussed in Section 2.3, the value for rv corresponds to the overflow orifice radius. The range of values for the dimensionless groups  $N_1$  and  $N_2$  in light dispersion separations is approximately

$$3 \times 10^{-4} \le N_1 \le 30$$
 (4-16)

and

$$.05 \le N_2 \le 30$$
 . (4-17)

# 4.2. Application of Trajectory Calculations

## 4.2.1 Results and Discussion

## (1) Trajectory Calculations

Figure 4.1 illustrates trajectories obtained for 100, 50, and 10 micron size particles in the CT-cyclone using parameter values from Figure 1.1a and Table 4.1 and a feed velocity was  $u_F = 5$  m/s. Values of  $N_1$  and  $N_2$  for these calculations covers the range given by by Eqs.(4-16) and (4-17) up to a value of 0.71. The trajectories were

Table 4.1. Dimensionless groups in trajectory calculations

	Dimensionless Group	Constituent Parameters	Representative Value
		L/r <sub>c</sub> f <sub>f</sub> /r̂c	44.0 0.25
	N <sub>1</sub>	uf m LD/LC	0.5 0.975
	(see Eq.(4-7) )	ν <sub>c</sub> q <sub>c</sub>	1.0 x 10 <sup>-6</sup> m <sup>2</sup> /s
Dispersion related		^ ^	
		Ĺ/r̂c r̂f/r̂c x	44.0 0.25
	N <sub>2</sub> (see Eq.(4-14))	uf V <sub>C</sub> QC	1.0 x 10 <sup>-6</sup> m <sup>2</sup> /s
	re		0.125
Hydro- dynamic	n rv		0.5 0.07

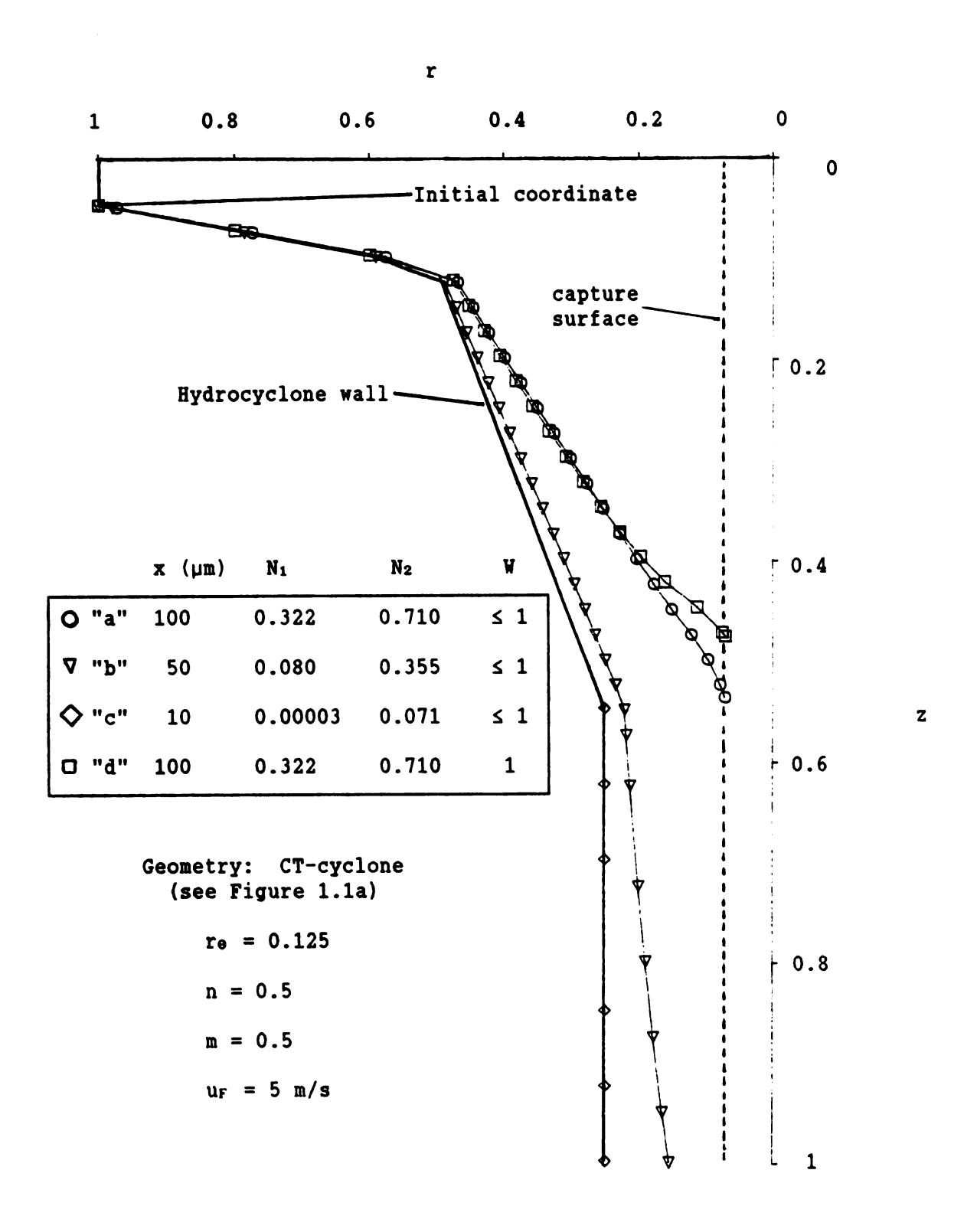
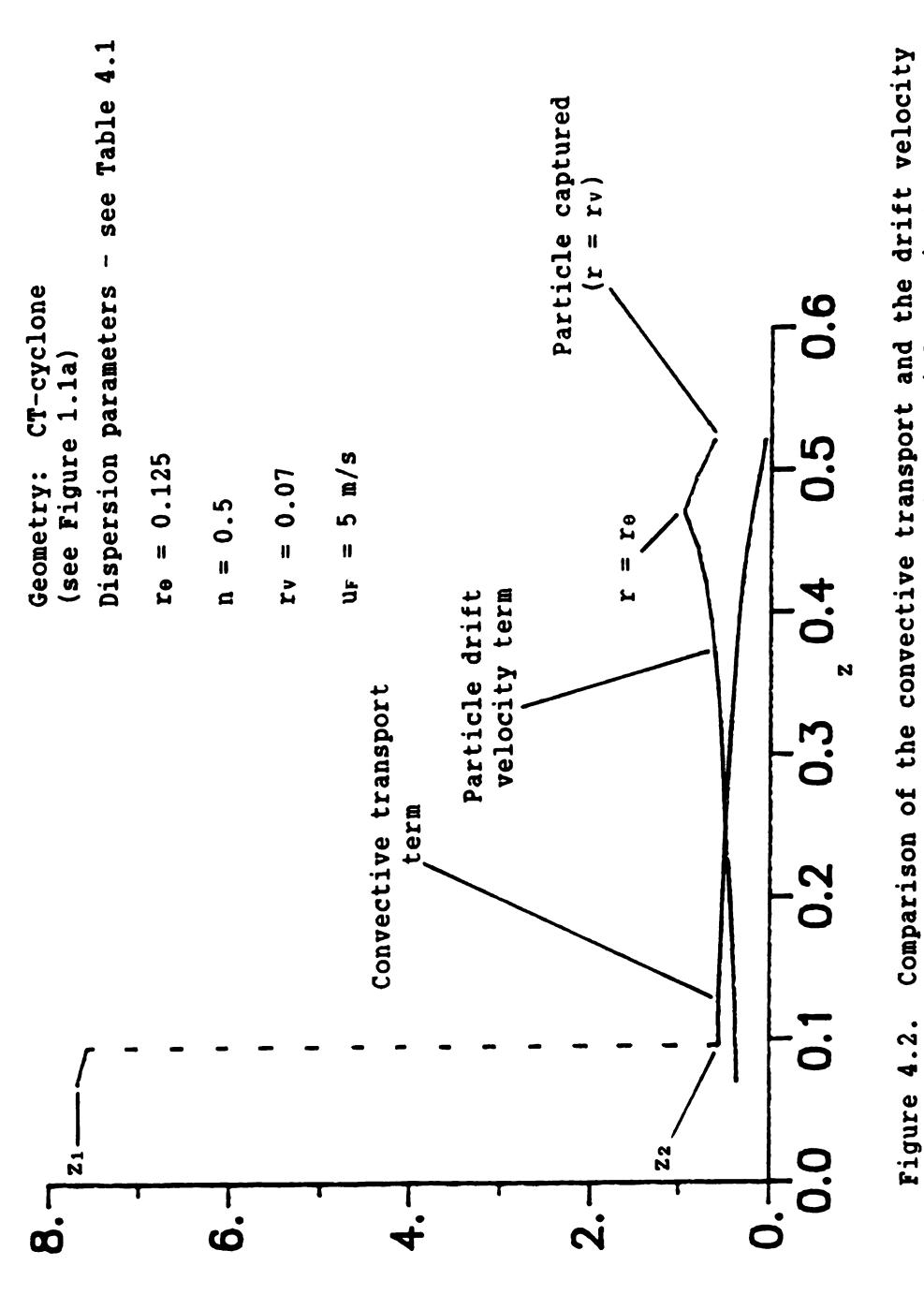


Figure 4.1. Example trajectories for particles in the CT-cyclone.

calculated by numerically integrating Eq. (4-4) using the computer program listed in Appendix A.1. The trajectories shown in Figure 4.1 do not portray critical trajectories because the particles do not pass through the coordinate (r = rv, z = 1). Curves a, b, and c represent trajectories found using the drag ratio calculated from Eqs. (3-2a) - (3-2c), while curve d represents a trajectory for a 100 micron particle resulting from the use of Stokes' law to calculate viscous drag regardless of the local value of Rep.

The 100 micron particle (curve a) is easily caught into the reverse flow vortex at  $z \approx 0.52$  (halfway along the hydrocyclone length). The 50 micron particle (curve b) is not quite captured and the 10 micron particle (curve c) is far from being captured. The larger particles leave the vicinity of the wall early in the trajectory, while the 10 micron particle does not move far from the wall. Note that the rate of radial migration for the 100 micron particle (curve a) slows down as it enters the forced vortex region ( $r < r_0$ ) where the tangential velocity is decreasing as a function of radial position. Curve d represents a trajectory for a 100 micron particle using Stokes' law alone to calculate particle drag. Compared to curve a, this particle reaches the capture surface at a smaller value of z due to the overestimation of drift velocities when  $Re_p \geq 2$  (the upper bound on Stokes' law).

Figure 4.2 represents a comparison of the magnitudes of the convective transport term and the particle drift velocity term from Eq.(4-4) for a 100 micron particle trajectory (Figure 4.1, curve a). The trajectory calculation is begun at an initial axial coordinate  $z_{\rm I}=z_{\rm 1}$ . The convective transport term is very much larger than the drift velocity



contributions in a 100 micron size particle trajectory.

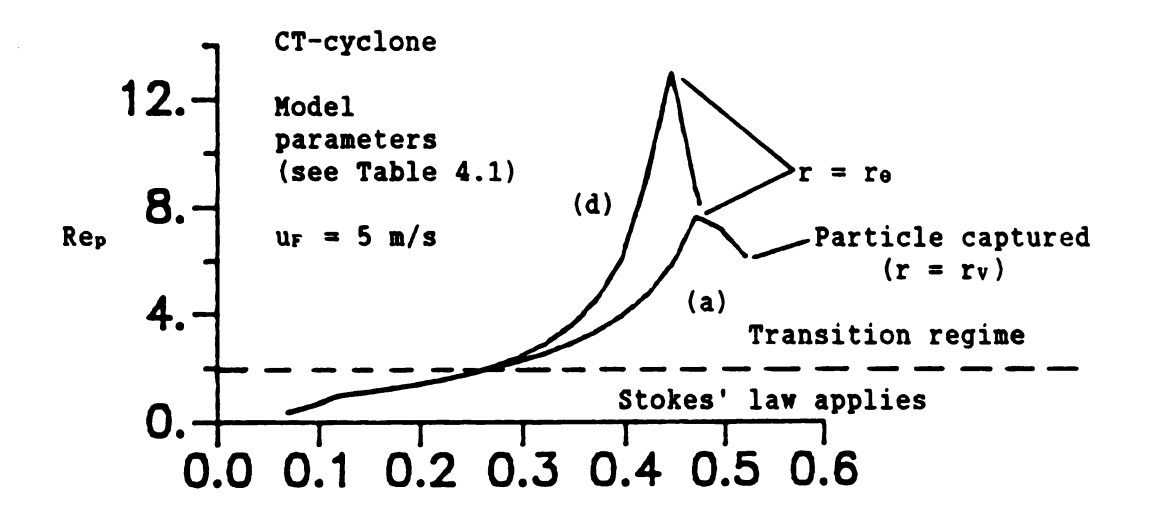
Figure 4.2.

Component of -dr/dz

term in the range  $z_1 \le z \le z_2$  because the fluid radial velocity induced by the 10° taper is large in this region. At  $z=z_2$ , the convective transport term has a jump discontinuity due to the sudden change from a 10° taper to a 0.75° taper. The drift velocity and the convective transport effects become more comparable as the particle transits the fine taper section ( $z \ge 0.11$ ). At  $z \approx 0.3$ , the drift velocity term dominates the convective transport term as the particle enters the regions of high centrifugal acceleration and reaches a maximum at the axial position corresponding to  $r = r_0$  (see Figure 4.1). The centripetal force acting on the particle decreases as the particle enters the forced vortex region ( $r \le r_0$ ).

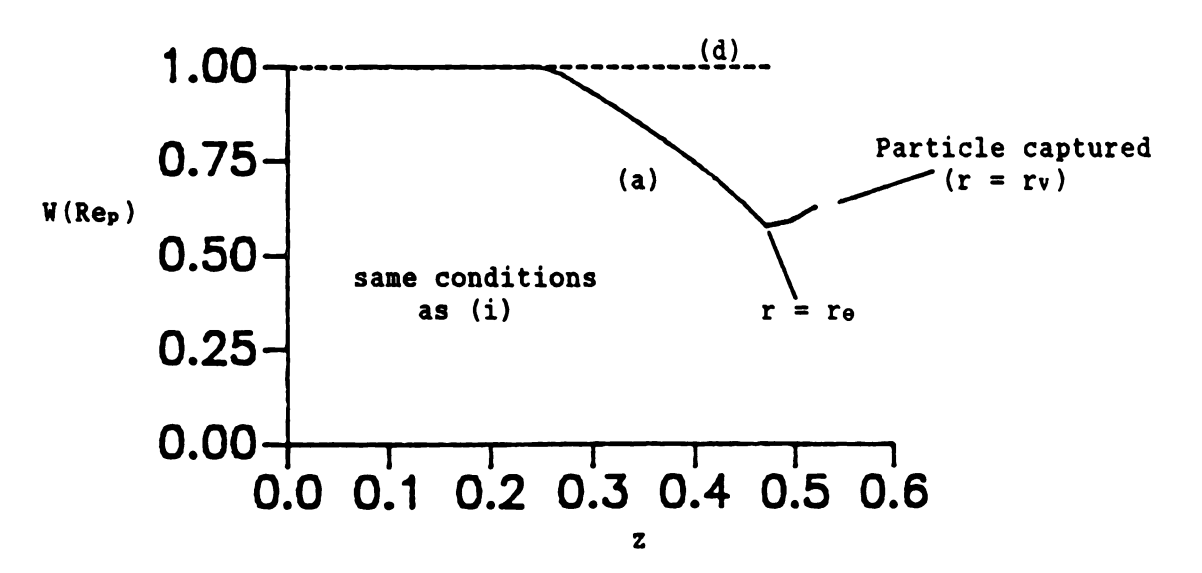
The variation of the particle Reynolds number as a 100 micron particle transits the flow field is shown in Figure 4.3a. The corresponding drag coefficient ratio is shown in Figure 4.3b. The lower curve in Figure 4.3a represents the particle Reynolds numbers attained for trajectory "a" of Figure 4.1 and the upper curve represents the particle Reynolds numbers calculated for trajectory "d". Both curves show a maximum value of Rep at r = re, with Rep decreasing as the particle enters the forced vortex region. The differences between the curves indicate the error incurred when using Stokes' law outside the region where it is valid. For the upper curve, the particle radial velocity is overestimated by a factor of two at the maximum value of Rep. At this point, the value of Rep for which Stokes' law is valid (see Eq.(3-2a)) is exceeded by a factor of seven.

In Figure 4.3b, the solid curve represents values of the drag ratio
W for trajectory "a" of Figure 4.1, while the value W = 1 represents



(i) Particle Reynolds number vs. axial position

z



(ii) Drag ratio vs. axial position

Figure 4.3. Comparison of Particle Reynolds number and drag ratio for 100 micron size particles; W = W(Rep) for curve (a), W = 1 for curve (d).

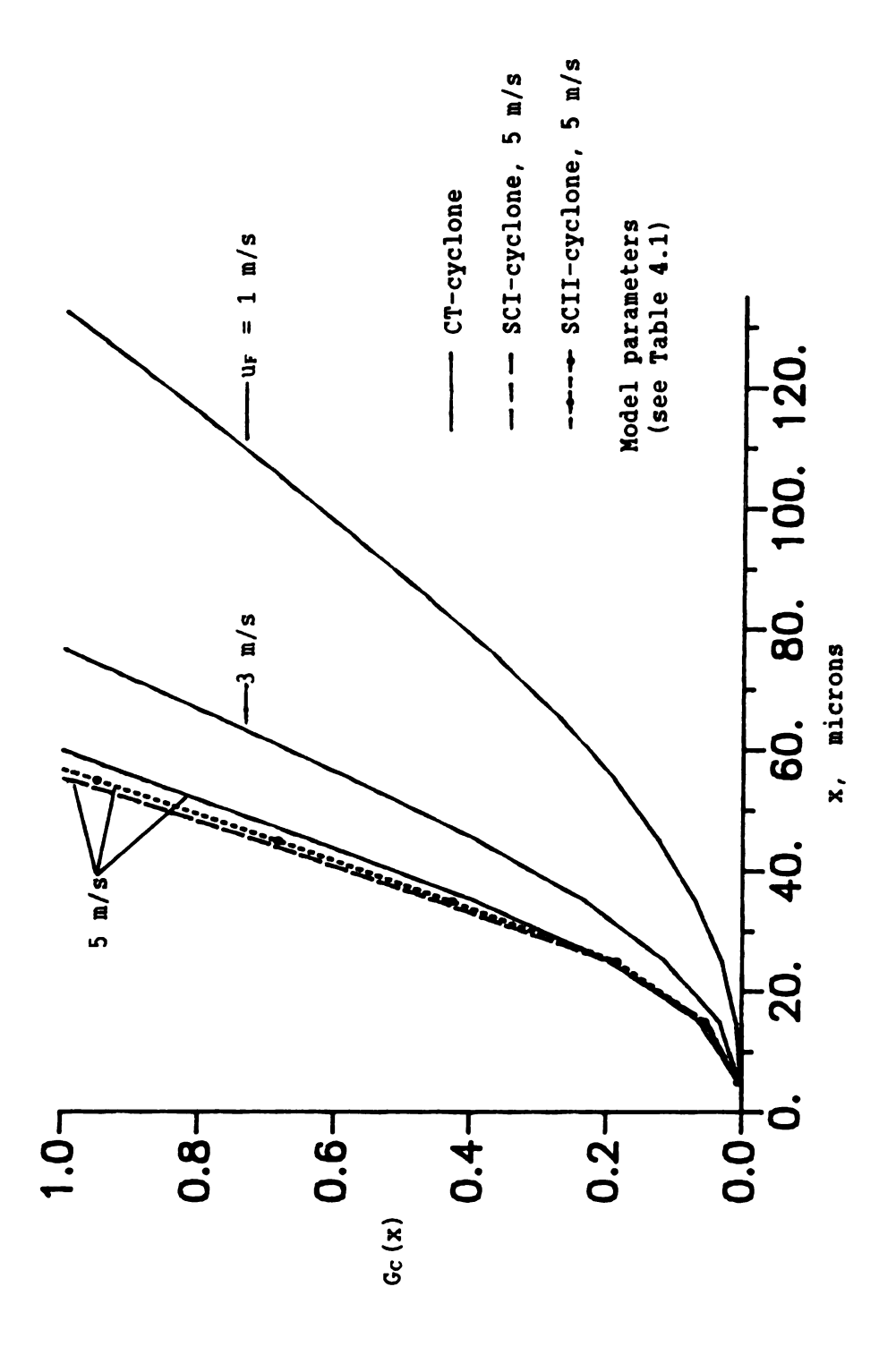
trajectory "d". The minimum value of W for trajectory "a" occurs at the corresponding maximum value of Rep in Figure 4.3a. At this point the drag on the particle has increased by a factor of about two compared to the Stokesian drag. As the particle enters the forced vortex region, the particle drag begins to decrease.

Figures 4.2, 4.3a, and 4.3b reinforce the importance of including the transition regime for viscous drag for large particles in the trajectory calculations. When extending the calculations to the same size particles with larger density differences than used in these calculations, the effects of non-Stokesian viscous drag become even more important because larger particle Reynolds numbers would result.

## (2) Centrifugal Grade Efficiency

The computer program used to calculate the particle trajectories discussed earlier in this section was modified to calculate the centrifugal grade efficiency. Using this modified program, the dimensionless groups (geometric, hydrodynamic, and dispersion) were varied to study the effect of these groups on the centrifugal grade efficiency. The flow chart for this program is shown in Appendix A.2.

To illustrate the effect of the dispersion groups N<sub>1</sub> and N<sub>2</sub> on the centrifugal grade efficiency, the particle size x and the feed velocity u<sub>F</sub> were systematically varied. Particle trajectories were calculated for each of the three designs and the centrifugal grade efficiencies were calculated using Eq.(2-39). Figure 4.4 shows a plot of the centrifugal grade efficiencies using the hydrodynamic parameters specified in Table 4.1. Curves for the centrifugal grade efficiency of the



Effect of inlet velocity on the centrifugal grade efficiency for the three hydrocyclone designs. Figure 4.4.

CT-cyclone at inlet velocities of 1, 3, and 5 m/s are shown as well as curves for the SCI and SCII designs at uf = 5 m/s. Each point on the curves is parameterized by a value of  $N_1$  and  $N_2$ , which ranged from .007 - .12 and .17 - 1.07, respectively. For a given particle size in the CT-cyclone, the centrifugal grade efficiency increases as up increases, but at a slower rate as up becomes large. At  $u_F = 5 \text{ m/s}$ , the CT-cyclone would be expected to capture all particles equal to or larger than 60 microns by centrifugal separation. A comparison of Figure 4.4 with Figure B.3 illustrates the manner in which the centrifugal grade efficiency curve and the particle size density distribution interact (see Eq. (2-27)). As up increases for a given hydrocyclone design, the centrifugal grade efficiency curve moves to lower particle sizes, sweeping across the size density distribution. At very high values of up, the centrifugal grade efficiency of even small particles will be close to unity and the centrifugal efficiency integral is maximized.

The effect of different taper angles is also shown in Figure 4.4 by comparing the centrifugal grade efficiency curves for all three designs at  $u_F = 5$  m/s. The comparison is made here under the assumption that the hydrodynamic parameters n, re, rv, and m are independent of hydrocyclone design. The effect of geometry (taper angles  $\alpha$  and  $\beta$ ) on the centrifugal grade efficiency is small compared to the effect of changing the inlet velocity.

The small differences between the centrifugal grade efficiency curves for the designs were observed at several values of  $r_\theta$  and  $u_F$ . The similarities in the results appear to be related to the observation

that most of the separation takes place in the cylindrical underflow section.

Differences in centrifugal grade efficiency at large particle sizes occur in the large taper section because these particles are convected at different rates to radii where high centrifugal acceleration exists. Thus, the SCI-design is the most efficient at the large particle sizes because it contracts the fluid and particles to regions of higher swirl more quickly than the other designs. The SCII-cyclone has the next highest centrifugal grade efficiency at the large particle sizes because it contracts the fluid and particles to the underflow radius earlier in the trajectory than in the CT-design.

At small particle sizes ( < 20 microns), the particles do not leave the vicinity of the wall until reaching the cylindrical underflow section (see Figure 4.1). At this point, the geometries of all three designs are similar and so the centrifugal grade efficiencies are similar. The very small differences between the designs at small particle sizes may arise from variations in mean residence times. The mean residence time for the SCII-design is 23% less than that for the SCII- and CT-cyclone (see Figure 1.1a), and is a likely reason for lower values of centrifugal grade efficiency for this design at small particle sizes. At large particle sizes the smaller mean residence time of the SCI-cyclone is more than compensated for by the quicker contraction of the fluid to the underflow radius.

To illustrate the sensitivity of the centrifugal grade efficiency to the hydrodynamic parameters, the value of  $r_{\theta}$  was varied from  $r_{\theta} = r_{U}$ 

to  $r_0 = r_0/4$ . Figure 4.5 shows the results of this study for the CT-cyclone at  $u_F = 5$  m/s. Values of the other model parameters were taken from Table 4.1. The effect of  $r_0$  on centrifugal grade efficiency is similar to that of the inlet velocity, where large changes in the centrifugal grade efficiency result as  $r_0$  is initially decreased from 0.25. As  $r_0$  decreases to about 0.125, the rate of change in  $G_C(x)$  towards higher values at each particle size decreases. Figure 4.5 also anticipates that if the hydrodynamics in each of the three designs were such that the values of  $r_0$  were appreciably different, then large differences in centrifugal efficiency may occur.

## (3) Centrifugal Efficiency

A computer program to evaluate the centrifugal efficiency integral (see Eq.(2-27)) by numerical integration is given in Appendix A.3. The program requires values for the centrifugal grade efficiency at several particle sizes as well as the parameters  $\sigma_g$  and  $\kappa_m$  for the log-normal size density distribution of the dispersion (see Appendix B.4). The centrifugal grade efficiency is fit to a second order polynomial, corresponding to the characteristic parabolic shapes of the centrifugal grade efficiency curves shown in Figures 4.4 and 4.5

$$G_C(x) = a_0 + a_1 x + a_2 x^2$$
. (4-18)

The product of the centrifugal grade efficiency and the size density distribution is integrated over the particle size distribution using a Simpson's rule algorithm. Figure 4.6 shows the result of the centrifugal efficiency calculation for the three designs using the hydrodynamic parameters from Table 4.1. The ordering of the curves is consistent with

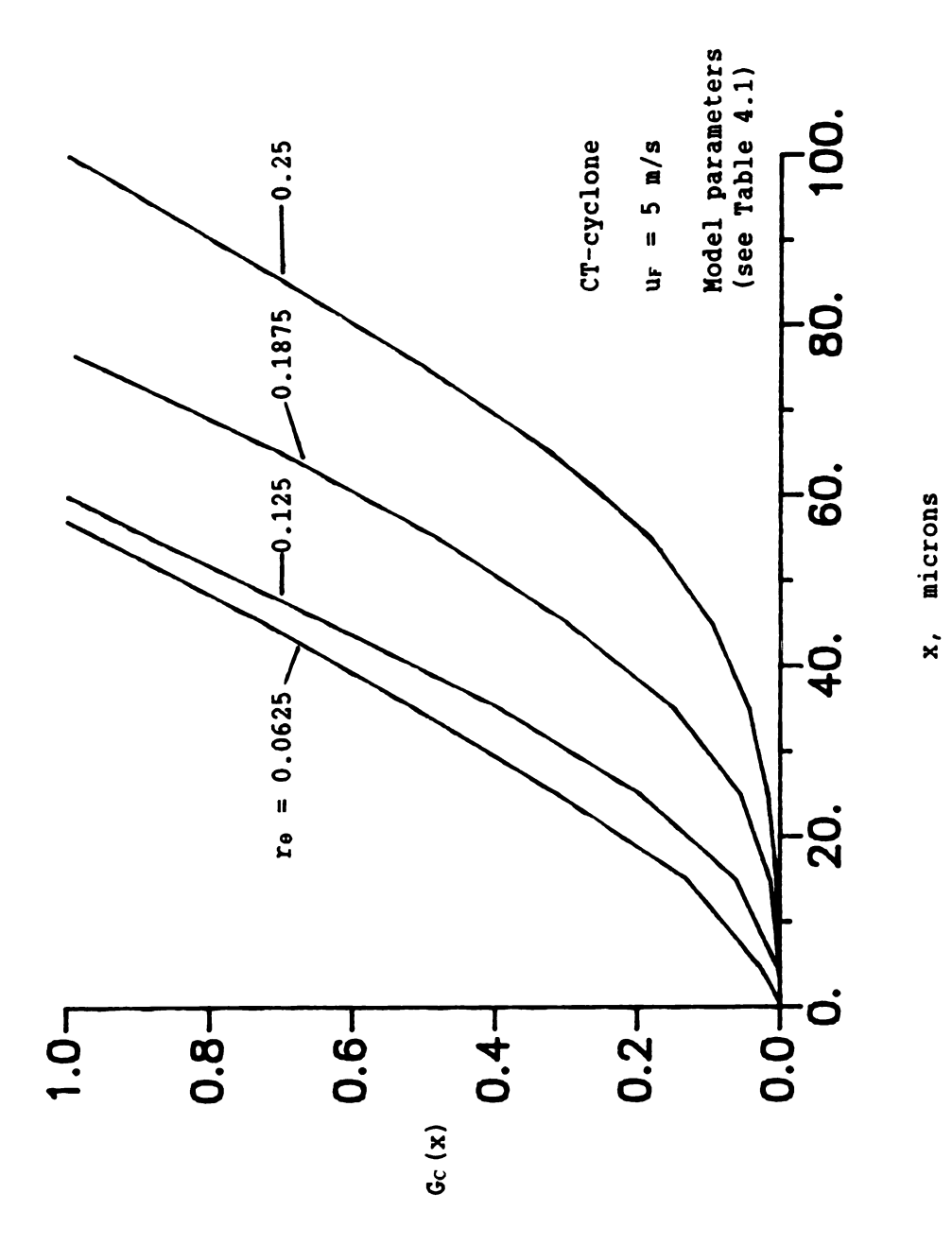
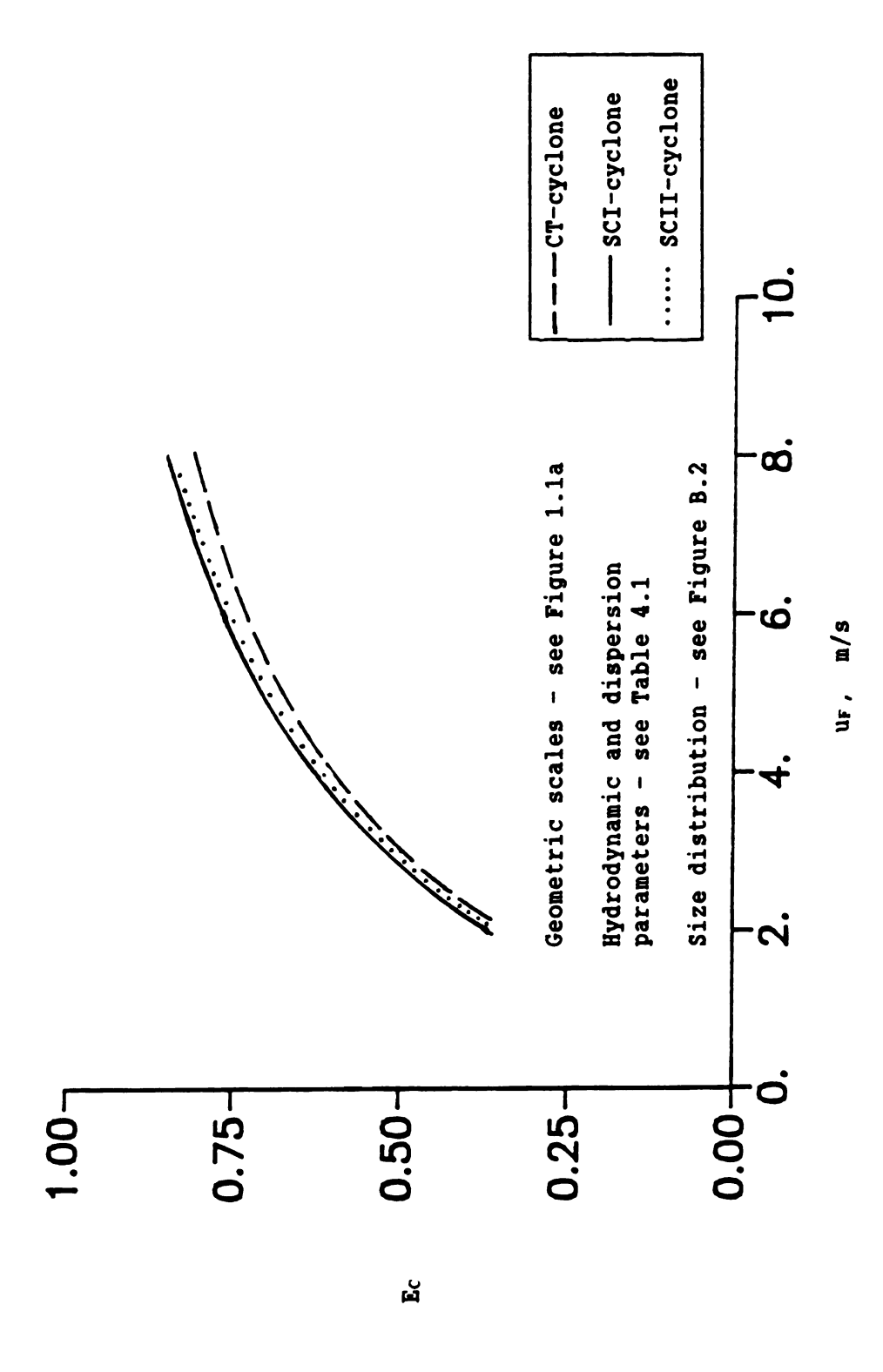


Figure 4.5. The effect of re on centrifugal grade efficiency for the CT-cyclone.



Centrifugal efficiency for the three designs with equal hydrodynamic and dispersion parameters. Figure 4.6.

the centrifugal grade efficiency curves calculated at up = 5 m/s in Figure 4.4. Again, the lower mean residence time for the fluid in the SCI-design is more than offset by the quicker contraction of the fluid to the underflow diameter where the large centrifugal acceleration occurs. For the set of hydrodynamic and dispersion parameters chosen, the centrifugal efficiency of each design slowly approaches the limiting value The effect of geometry (taper angles) is quite small, with  $E_C = 1$ . differences of only a few percent in the centrifugal efficiency between the three designs at all values of ur. Changes in the values of n or re for a single design result in a family of centrifugal efficiency curves that would move towards the upper left corner of Figure 4.6 as n increases or re decreases. Values of  $E_C = 1$  for low values of  $u_F$  (  $\approx$  3 m/s) can be obtained for sufficiently high values of n (n  $\longrightarrow$  1) or low values of  $r_{\theta}$  ( $r_{\theta} \longrightarrow 0$ ). Because the centrifugal efficiency is sensitive to the values of the hydrodynamic paramters, more detailed experimental data are needed for these values to estimate the separation efficiencies using the model developed here.

#### 4.2.2 Conclusions

The trajectory calculations showed that the inclusion of the transition regime in calculating particle drag was important for large particles. The use of Stokes' law alone to calculate viscous drag resulted in overestimation of particle drift velocities by a factor of about two.

Although the radial velocity of the fluid aids in the transport of the particles into regions of high centrifugal acceleration, the differences in the convective transport effect from design to design does not give rise to significant differences in the centrifugal grade efficiency.

The calculation of the centrifugal grade efficiency appears to be very sensitive to changes in the values for the dispersion and hydrodynamic parameters, but not to changes in taper angles. Using the same hydrodynamic parameters for all three designs gives similar values of the centrifugal efficiency (see Figure 4.6). If however, changes in taper angles produce distinct values for the hydrodynamic parameters in each hydrocyclone design, then larger differences in centrifugal efficiencies would be anticipated by the trajectory model.

## 4.3. Correlation of the Cut Size x50

A "reduced" centrifugal grade efficiency curve can be constructed by rescaling the particle size x by the particle size  $x_{50}$  which gives a centrifugal grade efficiency  $G_C(x_{50}) = 0.50$ . The  $x_{50}$  particle is commonly referred to as the cut size because the slope of the grade efficiency curve is generally steepest at this point. An ideal cut size in classification is that for which the grade efficiency is a step function. In this case all particles below the cut size are separated into one stream and all particles above this size are separated into another.

By rescaling the centrifugal grade efficiency curves for the three designs at  $u_F = 5$  m/s (see Figure 4.4), the reduced centrifugal grade efficiency plot shows the three curves to fall closely together, indicating similarity in the centrifugal grade efficiency curves. This trend exists at all values of the inlet velocity when the hydrodynamic parameters for each design are taken to be equal. Although the three designs have not been rigorously shown to be geometrically similar through

dimensional analysis, this similarity in the sharpness of separation is of practical importance. If the centrifugal grade efficiency can be correlated as a universal function of the variable  $x/x_{00}$  alone, then only a single particle size,  $x_{00}$ , need be pursued theoretically or experimentally to define the centrifugal grade efficiency for a class of geometrically similar hydrocyclones. This approach has been applied by many workers for heavy dispersion separation analysis (see Chapter 6 Bradley, 1965) and also by Colman and Thew [1983] for light dispersions. The particle trajectory model presented in Chapters 3 and 4 can be used to correlate the cut size  $x_{00}$  in terms of dimensionless variables derived from the particle trajectory equation.

To find a relationship to correlate the cut size it is useful to rearrange the dimensionless groups  $N_1$  and  $N_2$  so that the particle size x occurs only in one of them. This can be done by defining the following dimensionless groups

$$N_{3} = \frac{\left[\frac{(1 - P_{D}/Q_{C})m^{2} \mathcal{H}}{18\hat{r}_{C} u_{F}}\right]^{1/3}}{q_{C} r_{F}^{2} \hat{r}_{C}/\hat{L}}, \qquad (4-19)$$

and

$$N_4 = \frac{x^3 (1 - f_D/f_C) (m u_F)^2}{18 f_C^2 f_C}.$$
 (4-20)

Note that

$$N_4 = N_1 N_2$$
, (4-21)

and

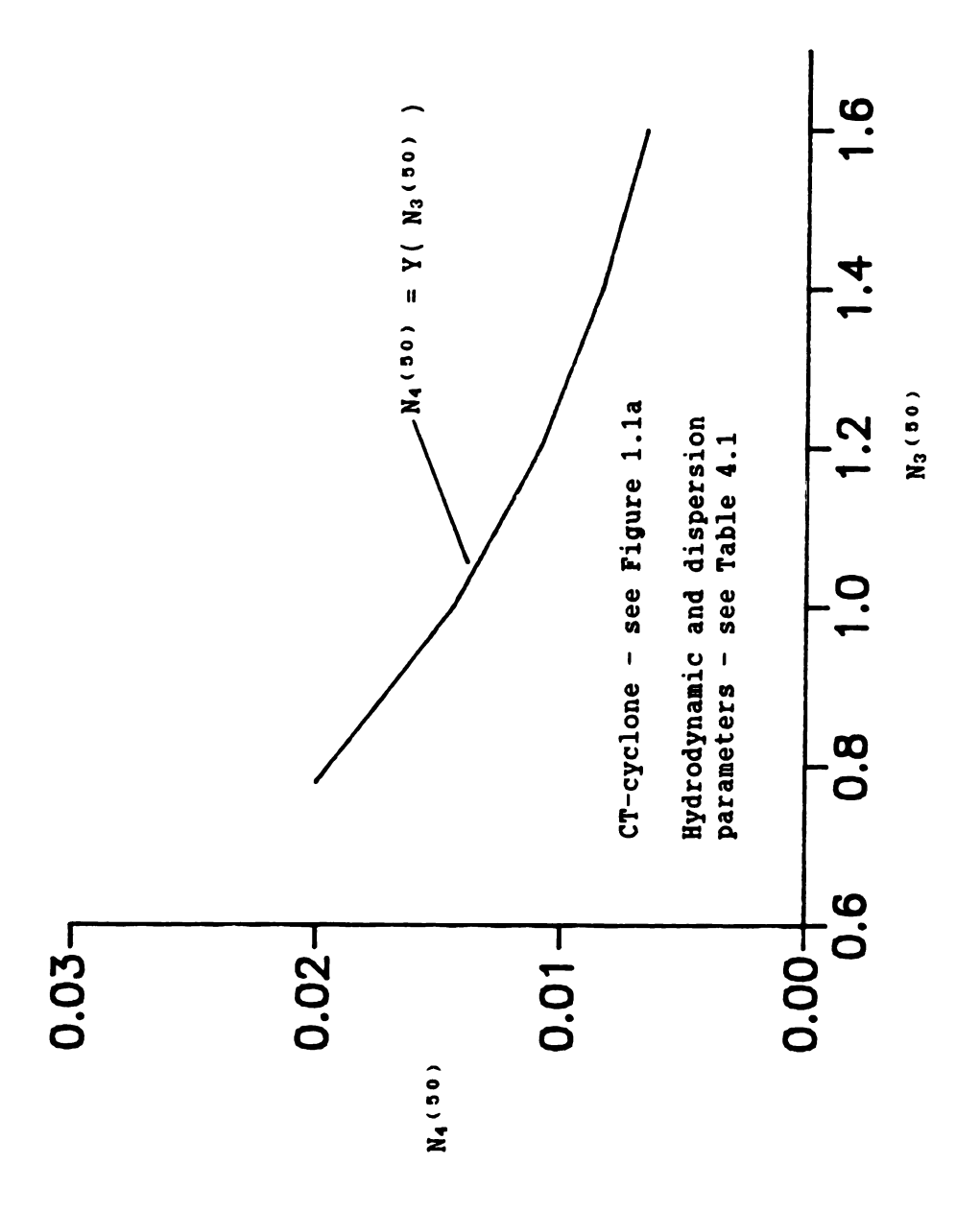
$$N_3 N_4^{2/3} = N_1 \qquad (4-22)$$

By definition, the critical trajectory for the  $x_{50}$  particle size passes through two coordinates;  $(r = r_V, z = 1)$  and  $(r_I(x_{50}), z = z_1)$ , where  $r_I(x_{50})$  is defined by Eq.(2-39) with  $G_C = 0.50$ . Inspection of Eqs.(4-4) as well as Eqs.(3-2a) - (3-2c) shows that for an arbitrary trajectory, when the geometric and hydrodynamic groups are chosen,  $N_1$  and  $N_2$  can be independently specified. Solution of the first order differential equation describing the particle trajectory (Eq.(4-4)) gives a constant of integration that can be eliminated by applying the initial condition  $r|_{Z_I} = r_I(x_{50})$ . By requiring the trajectory to satisfy the end condition  $r|_{Z_I} = r_V$ , the dimensionless groups  $N_1$  and  $N_2$  and, therefore, the groups  $N_3$  and  $N_4$  become functionally dependent, i.e.

$$N_4^{(50)} = Y(N_3^{(50)}), \qquad (4-23)$$

where the superscript (50) denotes a value of the dimensionless group corresponding to the  $x_{50}$  trajectory. The functional dependence indicated by Eq.(4-22) is valid only for the selected set of dimensionless geometric scales defined by Figure 1.1a and the dimensionless hydrodynamic parameters employed to calculate the critical trajectories. Figure 4.7 is a graphic portrayal of Eq.(4-23) for the CT-cyclone. The curve in Figure 4.7 was found by calculating critical trajectories at several values of the inlet velocity. Using the  $x_{50}$  values from the resulting trajectories in Eq.(4-19) gives a value of  $N_4$  (50) for each value of  $N_3$ 

The utility of Figure 4.7 is that for a single hydrocyclone design, the  $x_{50}$  value calculated for a given set of dispersion parameters can be related to the  $x_{50}$  value for any other set of dispersion parameters. This



The relationship between the dimensionless groups N<sub>3</sub> and N<sub>4</sub> for the cut size x<sub>50</sub> in the CT-cyclone. Figure 4.7.

relation holds only for fixed values of the hydrodynamic groups  $n,\ r_{\theta}$ , and  $r_{\Psi}$ .

The group  $N_4^{(50)}$  is proportional to  $x_{50}^3 u_F^2$ , while the group  $N_3^{(50)}$  is proportional to  $u_F^{-1/3}$ . Figure 4.7 shows that increasing values of  $N_4^{(50)}$  result as  $u_F$  is increased, all other parameters remaining constant. This behavior indicates a much slower decline in  $x_{50}$  than the corresponding increase in  $u_F$  (see Eq.(4-19)).

The  $N_3$  (50) -  $N_4$  (50) relationship will be used in Secton 5.6 to estimate the performance of the CT- and SCI-cyclones for a typical oilwater dispersion based on underflow purity data of both designs when separating a polyethylene powder dispersed in water.

#### CHAPTER 5

#### EXPERIMENTAL WORK

The objective of the experimental program was to determine the separation performance of a single-cone hydrocyclone relative to the Colman-Thew double-cone design. The scope of the experimental program included determination of pressure drop - flow rate characteristics, reverse flow vortex behavior, and underflow purity for both designs.

#### 5.1. Hydrocyclone Designs

Two single-cone hydrocyclone designs were discussed in Chapter 1 (see Figure 1.1a) and were evaluated using the trajectory model to find centrifugal efficiencies in Chapter 4. Using the same hydrodynamic parameters, the centrifugal efficiencies calculated by the trajectory model for all three designs were similar, suggesting that the separation performance of the single-cone designs would be comparable to the CT-cyclone (see Figure 4.6). Of the two single-cone designs, the SCI-cyclone was selected for experimental comparison with the CT-cyclone because the large taper angle  $\alpha$  was the same for both, facilitating interchangeability of parts. As discussed in Chapter 1, the cylindrical swirl chambers for both designs are identical ( $D_C = 76$  mm), as is the portion of the large taper section up to the point where  $\hat{r}_w = \hat{r}_C/2$ . At this point in the CT-cyclone, the fine taper section ( $\beta \approx 3/4^\circ$ ) begins. In the SCI-cyclone the 10° taper continues to the underflow diameter, where a long

cylindrical tube is connected which leads to the underflow orifice. This variation in taper angle leads to a 23% smaller volume for the SCI-cyclone (see Figure 1.1a). The total length of the hydrocyclones equaled 1.67 m.

Photographs of the two hydrocyclones are shown in Figures 5.1a and 5.1b. The clear acrylic construction afforded visual observation of the flow patterns within the hydrocyclone body. The feed tube consisted of a short section of copper tube glued to the acrylic body, forming an outer wall tangential entry (see Figure 1.1a). The copper tube allowed sufficient clamping tension for the attached feed hose. The overflow tube was attached through an opening in the hydrocyclone roof and was flush mounted to the swirl chamber end wall. The overflow orifice consisted of a 5.2 mm hole drilled in a 3 mm thick end wall, which opened up to a 12.7 mm ID diameter overflow tube.

The fine taper section for the CT-cyclone was constructed using seven short subsections individually bored and connected by three evenly spaced steel rods (see Figure 5.1a). The steel rods were placed in 6.4 mm diameter holes drilled parallel to the longitudinal axis of each subsection. The subsection joints were sealed with 0.4 mm thick Fel-pro paper gaskets. The fine taper assembly was attached to the upper body by tightening the threaded ends of the three rods into tapped recesses of the large taper section. The steel rods were also bolted at the small diameter end of the fine taper section to clamp the whole hydrocyclone assembly firmly together. The average taper angle in this section was  $\approx 0.80^{\circ}$  over the seven subsections. A value of 2.4° over the last 83 mm of length was thought not to affect operation.



(a) CT-cyclone (see Figure 1.1a for dimensions)



(b) SCI-cyclone (see Figure 1.1a for dimensions)

Figure 5.1. Hydrocyclone designs tested in the experimental work.

The CT-cyclone could be transformed into the SCI-cyclone by removing the fine taper section and bolting on the additional 10° taper section, 54 mm in length. To this section the cylindrical underflow tube was connected.

## 5.2. Experimental Flow Loop

A recycle flow loop was used in the experimental work and is shown in Figure 5.2. Two Meyer QP-30 (3 hp) centrifugal pumps connected in series were supplied from a 200 liter feed tank. In addition to the feed supply valve, a bypass was included in the line to assist in the control of the feed volumetric flow rate. All pressure and return lines were 19 mm ID copper tube or nylon reinforced hose except the overflow line which was 12.7 mm ID nylon reinforced hose. Prior to entering the hydrocyclone, the feed stream passed through an Omega FL-75 rotameter (1 - 30 gpm). During separation tests, the feed stream was next passed through an isokinetic sampling assembly. The overflow stream was passed through a 9.5 mm ID Whitey needle valve prior to returning to the feed tank. The underflow stream was routed through a 19 mm Crane globe valve and, during separation tests, an isokinetic sampling assembly identical to the feed sampling assembly. Before returning to the feed tank, the underflow stream passed through a second Omega FL-75 rotameter. Stream pressures were measured by standard Weiss Bourdon type pressure gauges with a range of 0-100 psig at 2 psig intervals. The pressure gauges were located 15, 5, and 34 cm from the feed, underflow, and overflow connections, respectively (see Figure 5.2). Cooling water was passed through approximately 10 m of 6.4 mm ID flexible copper tubing to maintain a suspension temperature near 20°C.

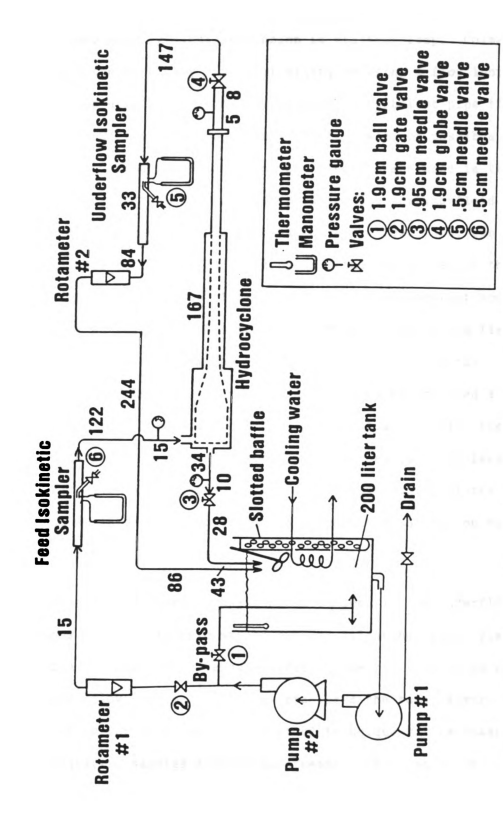


Figure 5.2. Flow loop (nominal lengths given in cm).

One of the difficulties in working with light dispersions is in maintaining a homogeneously mixed suspension in the test loop. Colman [1981] maintained the necessary degree of mixing by using a flow loop that kept about one half of the total suspension in turbulent pipe flow in circulation around the flow loop. This strategy was not possible because of the limited capacity of the two centrifugal pumps used in this study, and so a recycle tank holding nearly 90% of the working fluid was employed. To maintain a well mixed suspension in the feed tank, the following measures were employed. The feed bypass line was routed to the bottom of the feed tank. A "tee" fitting was employed to prevent vortex formation and air entrainment. A single slotted metal baffle was fastened to the tank wall running from the tank bottom to just above the liquid-air interface. An ac motor (G.E. 1750 rpm, 1/4 hp) rotated a twobladed centripetal impeller to mix the suspension. Additionally, the overflow and underflow lines were adjacently discharged into the feed tank (below the liquid-air interface) to promote rapid mixing of the streams. These measures combined to give a homogeneous suspension with no air entrainment into the feed tank.

To determine the dispersed phase concentrations in the underflow and feed streams by a gravimetric method such as filtering, small samples were needed for analysis. Because large volumetric flow rates of the feed and underflow streams (\$\approx\$ 25 gpm) precluded the total diversion of each stream for sampling, some sort of technique was necessary to take representative samples from these streams. This was accomplished using two isokinetic sampling probes, described in detail in Appendix B.1.

### 5.3. Experimental Test Procedures

All data were recorded when operating the flow loop with a suspension of high density polyethylene powder (HDPE) in water. To mix the suspension, 15 ml of Liquinox detergent were added to approximately 190 liters of tap water in the feed tank. The soap acted as a surfactant for the HDPE powder, which exhibited strong hydrophobic characteristics. To eliminate soap sudsing, 15 ml of True Value DF-5 Carpet Defoamer was added to the mixture before agitation by the impeller was initiated. The HDPE powder was then added in small portions until a homogeneous suspension was obtained.

The pressure drop - flow rate characteristics for both hydrocyclones were determined in conjunction with the study of the reverse flow vortex. These experimental tests were conducted at an HDPE concentration of approximately 400 parts per million by mass (wppm). Pressure readings and flow rates were recorded for flow conditions exhibiting stable reverse flow vortex characteristics as discussed in Section 5.4.2. The feed and underflow rotameters were calibrated by the procedure outlined in Appendix B.2.

The determination of the underflow purity E' involved the use of the isokinetic sampling technique and subsequent gravimetric analysis. The underflow purity was defined by Eq.(2-20) in terms of volumetric fractions  $y_U$  and  $y_F$ . For immiscible components where  $f_D/f_C \approx 1$ , the component volume fractions are equivalent to mass fractions. The mass fractions of dispersed phase in the feed and underflow streams were determined gravimetrically using a filtration technique. To separate the solids from the sample fluid, #3 Whatman filters (passing 6 micron

particles and below) were used in a Buchner funnel - aspirator arrangement. The filter papers were pre-dried and weighed prior to filtering. After filtering, the papers and solids were oven dried and then weighed to determine solids content. A detailed filtration-drying-weighing sequence is given in Appendix B.3.

In the separation tests, feed concentrations of about 900 wppm were obtained by mixing approximately 170 g HDPE with 190 liters of tap water. Each batch was used for sampling up to a total of 5 g of solids. This total did not include feed samples, which should not change the concentration or the size distribution of the suspension. The size density distribution was assumed to be unaffected by the removal of this small fraction of solids (  $\approx$  3% of the total mass). Overflow samples were not collected because these samples contained a large amount of solids, which would necessitate frequent replenishment of the dispersion. A closure of the steady state material balance was not pursued directly, but the reproducibility of underflow purity measurements was indicative of steady state conditions. Samples for the feed and underflow streams ranged from 500 ml at low volumetric flow rates ( $Q_F \approx 10$  gpm = 38 lpm) to 1 liter at the highest volumetric flow rates ( $Q_F \approx 25$  gpm = 95 lpm). These volumes represent sampling times of approximately 10 - 15 seconds.

The isokinetic sampling assemblies were calibrated by closing the overflow valve and running the suspension through the feed and underflow sampling assemblies (see Figure 5.2). In this configuration both streams should remain at feed conditions. Six samples from each probe were taken using 30 second intervals between feed and underflow stream sampling. Filtering analysis of the twelve samples indicated a mean of 870 wppm

with deviations of ± 19 wppm. These results compared favorably with the calculated feed concentration of 856 wppm based on flow loop volume and the initial amount of solids charged to the system, giving confidence to the sampling and gravimetric procedures. These results reflect corrections for a tap water dissolved/stray solids content of 12 wppm determined by a separate filtration analysis. The calibration tests for the isokinetic sampling assemblies indicate that the feed concentration remains approximately constant over the duration of the experiment. In subsequent tests only two feed samples were taken, one at the beginning of each test and another at the end of a test run. The underflow purity was then calculated using an average of these two values for the feed concentration. An uncertainty of ± 19 wppm in the feed concentration from the calibration of the sampling assemblies gives an uncertainty of ±2% in the underflow purity.

#### 5.4. Results and Discussion

## 5.4.1 Characterization of the Dispersion

To characterize the HDPE powder, the mass density and the size density distribution were determined as outlined in Appendix B.4. A mass density of  $\mathcal{C}_D = 0.976 \pm 0.004$  g/cm³ was found for the solids by a gravimetric procedure. This corresponds to a dimensionless density difference of  $1 - \mathcal{C}_D/\mathcal{C}_C \approx 0.025$  (at 20°C).

The size density distribution was measured by using an Elzone 180 series particle sizer with 127 channel capability. Table B.1 lists the cumulative size distribution data, indicating particle sizes from 2 - 120 microns. This is quite representative of size distributions which occur in an the offshore deciling environment (see p.6 Colman, 1981). When the

cumulative data is fitted to a log-normal size density distribution (see Figure B.2), a mode size of 43 microns is calculated. The combination of the small density difference and the small size range makes this dispersion suitable for determining subtle differences between separators.

#### 5.4.2 Reverse Flow Vortex Behavior

The stability of the reverse flow vortex for the hydrocyclones studied was found to be a dynamic phenomenon. Instabilities in the reverse flow vortex manifested themselves over periods of time as short as ten seconds and as long as twenty minutes, depending on the operating conditions. In both designs, the particle core existed for the entire length of the hydrocyclone, its diameter increasing with increasing feed concentration, but never exceeding the overflow orifice diameter for stable conditions.

In a study of a series of hydrocyclone designs, Colman [1981] noted that flow conditions corresponding to good separation efficiencies could be determined by observing the behavior of the reverse flow vortex. These observations were confirmed in the present study. The reverse flow vortex behavior can be easily visualized because light dispersed phase particles migrate toward the core and are captured in the jet-like flow. Figure 5.3 summarizes the observed operating regimes for the CT- and SCI-cyclones. The three operating regimes include: (1) an unstable feed flow; (2) a stable reverse flow; and, (3) a transient reverse flow. The lower boundary for the inlet velocity, defined by  $u_F \approx 1.7 \text{ m/s}$  (\$\approx\$ 8 gpm), represents an operating condition for the flow loop at which the feed pumps would not deliver a steady volumetric flow rate to the hydrocyclone test section.

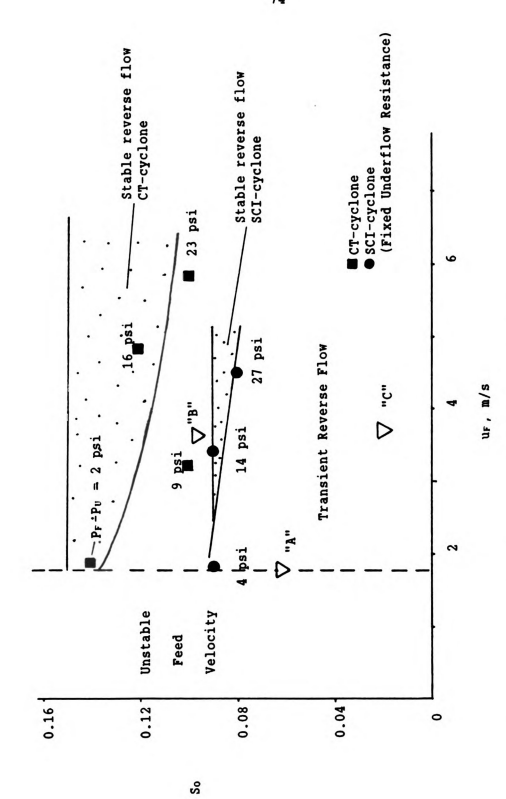


Figure 5.3. Operating regions for hydrocyclone designs.

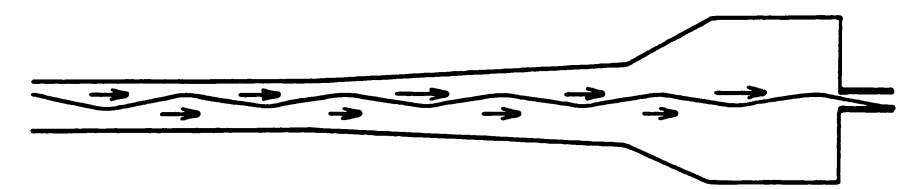
The two stability boundaries in Figure 5.3 were obtained by visual observation of the particle core. The underflow valve was left fully open, giving a fixed underflow resistance for all experiments reported in this research. The pressure drop across the fully open glove valve provided sufficient back pressure to prevent the formation of an air core in the hydrocyclone. At each selected value of the feed velocity, the overflow valve was opened incrementally from the fully closed position. If instabilities in the reverse flow vortex resulted in a transition from reverse flow vortex to a through flow vortex, the overflow valve was opened further. This procedure was continued until no instabilities occurred. The criterion used for stability was no longitudinal pulsations or any thickening of the particle core within twenty minutes of setting the overflow valve position. This time limit was chosen for practical considerations. After determining the minimum overflow ratio So for a given feed velocity, the stability of the reverse flow vortex was further checked by momentarily clamping down on the overflow hose, creating a pressure pulse in the overflow line. If the core remained in a stable reverse flow, the coordinates of the operating point were noted. The points comprising the stability curves locate specific values of  $u_F$ ,  $S_0$ , and  $P_F-P_U$  which are marginally stable.  $P_F$  and  $P_U$ represent, respectively, the feed and underflow pressures (psig) at the wall.

The transient reverse flow regime indicates the combinations of  $S_0$  and  $u_F$  that resulted in an eventual transition from a reverse flow vortex to a through flow (concurrent with the main flow) vortex. For each hydrocyclone design, the transient reverse flow regime consists of all

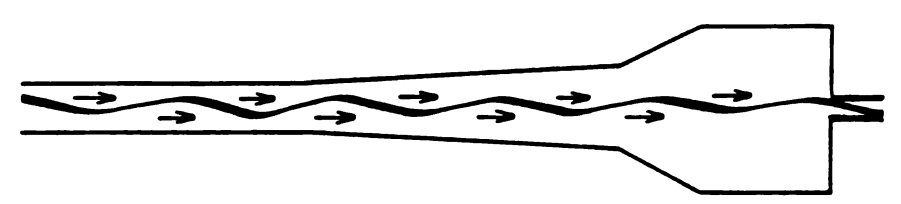
points below the marginal stability curve. The stable operating regions for each hydrocyclone consists of the crosshatched regions above the stability curves. The upper bound for each region was determined by the "natural" overflow ratio, occurring when the overflow and underflow valves were in the fully opened position. As Figure 5.3 shows, the maximum values of the overflow ratio obtained were  $(S_0)_{CT, max} = 0.15$  and  $(S_0)_{SCI, max} = 0.09$ . Also, the stable operating region for the SCI-cyclone is narrower than that for the CT-cyclone, but occurs at lower values of So over the range of feed velocities studied.

The transition from a reverse flow inner vortex to a throughflow inner vortex included three stages. The first stage was the formation of what initially appeared to be a stable reverse flow vortex. The particle core resembled a thin strand of cord along the hydrocyclone axis, somewhat helical in shape as shown in Figure 5.4a. In both designs studied, the motion of groups of solid particles indicated the axial flow of the inner vortex to be toward the overflow orifice over most of the vortex length. In the region near the underflow orifice, the direction of inner vortex axial flow could not be determined. In the SCI-cyclone, some incoherence of the particle core could be seen between the cylindrical underflow section and the large taper section. This incoherence may be due to a secondary (eddy-type) flow caused by the continuance of the 10° taper angle to the underflow diameter over a short distance.

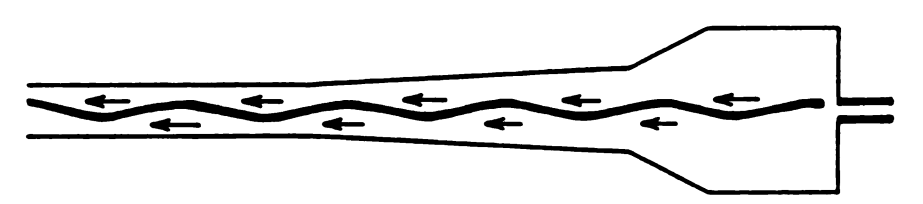
The second stage of the transition begins with longitudinal pulsations of the particle core at a frequency of approximately 2 Hz, originating from near the underflow orifice and continuing toward the overflow orifice (see Figure 5.4b). This event was accompanied by a general



## (a) Stable reverse flow vortex



# (b) Longitudinal Pulsations and thickening of the particle core



# (c) Stable through flow vortex

Figure 5.4. Progression of the reverse flow vortex instability in the CT-cyclone.

thickening of the particle core, also observed by Colman [1981]. The reverse flow particle core was not observed to break up as it proceeded toward the overflow orifice and remix with the feed flow as noted by Colman (see p.29 Colman, 1981). Instead, the particle core was observed to thicken until its diameter exceeded that of the overflow orifice, accompanied by a sudden increase in the overflow stream pressure and a choking of the overflow stream. This thickening was followed by the third stage of the transition; a sudden transformation of the inner vortex from a reverse flow to a through flow vortex (see Figure 5.4c). At this point the overflow ratio So was essentially zero. Some observations of the reverse flow to through flow mode were accompanied by the entrainment of a small amount of air into the inner vortex, but this was not true in general. Also, in some experiments, the third stage of transition was characterized by three to four consecutive transitions from reverse flow to through flow and back to reverse flow. In these cases, the final result was always a stable through flow inner vortex.

The minimum overflow ratio of the CT-cyclone was found to be approximately 10% at  $u_F = 5.8$  m/s, four times as high as the minimum value of the overflow ratio for the CT-cyclone (with the same nominal design scales) reported by Colman and Thew (see Colman and Thew,1983). It is possible that the lower value reported by Colman and Thew may have been due to the use of higher back pressures at the underflow orifice. The pressure drop across the hydrocyclone,  $P_F - P_U$ , when operating at the lower limit of stability is indicated in Figure 5.3 for each value of  $u_F$ . The SCI-design has a higher pressure drop at all feed velocities.

The transition from reverse flow vortex to through flow vortex

occurred on different time scales depending on the initial coordinates  $(u_F,S_0)$  of hydrocyclone operation. In general, the further below the stability curve, the shorter the period of time that elapsed before the transition. Point "A" on Figure 5.3 indicates a transition occurring over an elapsed time of five minutes for the CT-cyclone with initial coordinates  $(u_F = 1.7 \text{ m/s}, S_0 = .06)$ . Point "B" represents a transition occurring over an elapsed time of 19 minutes in the same design, with initial coordinates  $(u_F = 3.6 \text{ m/s}, S_0 = .09)$ . When the initial conditions are set well below the stability curve such as in point "C", where  $S_0$  is approximately 0.02, the CT-cyclone exhibited the instabilities within 10 - 20 seconds.

## 5.4.3 Pressure Drop Measurements

The pressure losses across a hydrocyclone are a direct measure of the operating costs of the device. The pressure drop - flow rate data reported in this section were observed at the minimum values of So corresponding to the stability curves in Figure 5.3. The dimensionless groups chosen to represent this data are the pressure loss coefficients and the feed Reynolds number defined as

$$C_{PU} = \frac{P_F - P_U}{C_{C} u_F^2/2}, \qquad (5-1)$$

$$C_{P0} = \frac{P_F - P_0}{e^{C_{UF}^2/2}},$$
 (5-2)

and

$$Re_{F} = \frac{D_{F} u_{F}}{\nu_{c}} , \qquad (5-3)$$

where Po is the wall pressure measured near the overflow orifice. The

intensity of the fluid swirl at a given axial position is a function of the radial pressure gradient. Measurement of the wall pressures at the inlet and outlets of the hydrocyclone (see Figure 5.2 for pressure gauge location) only gives a gross measurement of the conversion of pressure energy of the fluid into rotational energy that is useful for centrifugal separation.

Figure 5.5 shows the plot of the underflow pressure loss coefficient vs. feed Reynolds number for the two hydrocyclone designs studied. The pressure loss coefficient for the SCI-cyclone is nearly double that for the CT-cyclone. This higher pressure loss indicates a difference in the internal flow structures of the two hydrocyclones, which is consistent with the observation of the incoherence of the particle core near the large taper section apex in the SCI-cyclone (see Section 5.4.2). The coherence of the particle core throughout the entire length of the CT-cyclone, coupled with a lower pressure loss coefficient, suggests that function of the fine taper is to conserve angular momentum without creating secondary flows, resulting in a lower pressure loss.

The pressure loss coefficients for both designs are practically independent of the feed Reynolds number, indicating that viscous losses are small compared to centrifugal head losses.

The pressure loss for the CT-cyclone reported by Colman (see Figure 52, 1981) was replotted in dimensionless variables and is shown in Figure 5.5. The curve indicates a higher pressure loss for the CT-cyclone than was found in the present study, but this may have been due to the inclusion of pressure losses across a vortex breaker at the underflow orifice

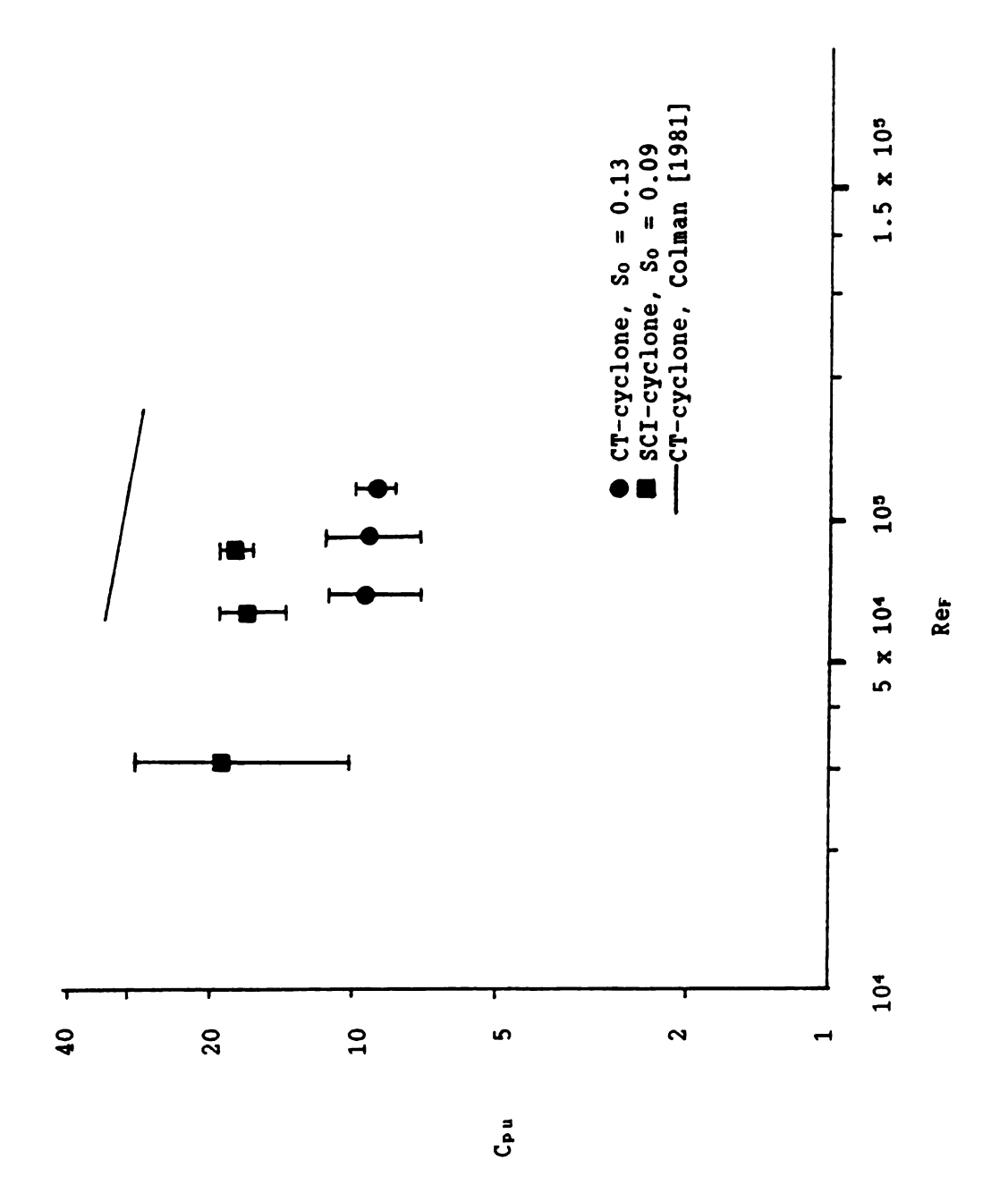


Figure 5.5. Pressure losses for the CT- and SCI-cyclones.

in Colman's experiments. The vortex breaker was included to dissipate the fluid swirl, thus defining the separation length. In the present study, the underflow pressure was measured prior to the underflow valve (see Figure 5.2). Observation of the flow downstream from the underflow valve showed no particle core, indicating that the valve had effectively dissipated the fluid swirl. The overflow pressure loss coefficients, not shown in Figure 5.5, are approximately twice as large as the Cpu values given for each design, suggesting that viscous losses are important for this smaller diameter orifice. This trend agrees with the observations of Colman [1981].

## 5.4.4 Underflow Purity Measurements

The separation performances of the CT- and SCI-cyclones were evaluated using the HDPE dispersion at a feed concentration of  $y_F \approx 900$  wppm and feed velocities ranging from 2.5 to 5.8 m/s. Figure 5.6 shows the underflow purities measured for each design. The CT-cyclone was operated at an overflow split ratio  $S_0 \approx .13$ , while the SCI-cyclone was operated at  $S_0 \approx .09$ , consistent with the minimum  $S_0$  values reported in Section 5.4.1. The SCI-cyclone reached an apparent asymptotic value of E' = 0.42 at  $u_F = 5$  m/s. On the other hand, the underflow purity for the CT-cyclone equals 0.60 at  $u_F = 5.8$  m/s. The two values of  $E' \approx 0.50$  at  $u_F \approx 2.5$  m/s for the CT-cyclone were not reproducible in an additional separation test and are thought to represent anomalous results. The higher underflow purities attained by the CT-cyclone, coupled with the incoherence noted in the particle core for the SCI-cyclone (see Section 5.4.2), further suggests differences in hydrodynamics between the two designs.

The difference in overflow ratios for the two designs may be a

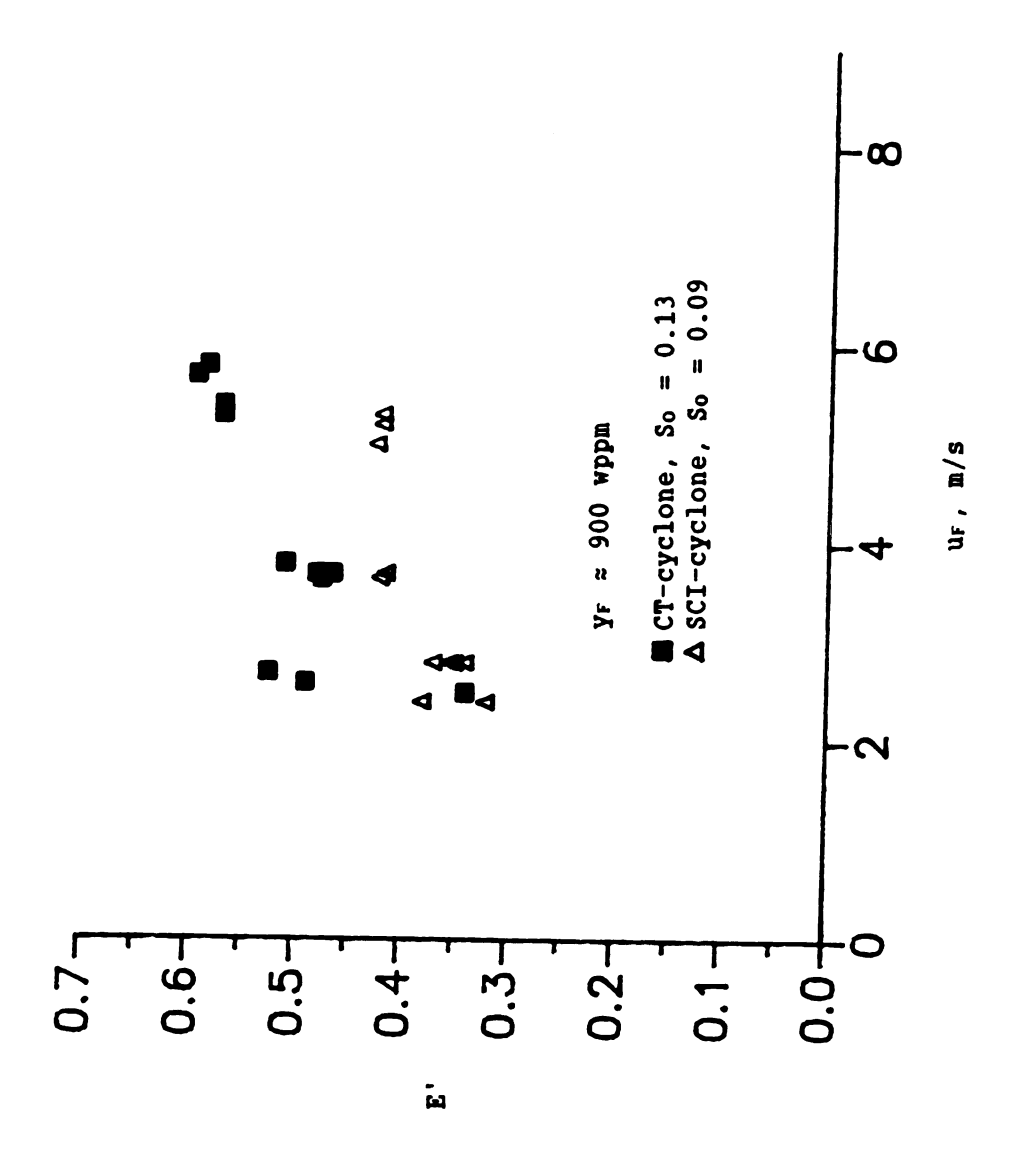


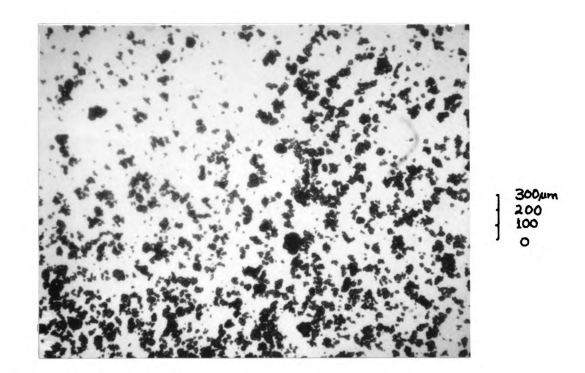
Figure 5.6. Underflow purity for the cyclone designs.

factor in the higher underflow purity observed for the CT-cyclone. The studies of Colman, however, suggest that the underflow purity is not dependent on the overflow ratio when operating above the minimum value of So (see Figure 1.3b). This indicates that the volumetric flow rate leaving through the overflow orifice is not a limiting factor for the removal of light dispersed phase, especially when the volume fraction of the dispersed phase in the feed is much less than the overflow ratio So. In both designs, the reverse flow vortex was observed throughout the hydrocyclone length, giving light particles the full opportunity to reach the capture surface. This suggests that for separation of the HDPE dispersion, an increase in the operating overflow ratio of the SCI-cyclone (by use of higher back pressure at the underflow orifice) would not substantially improve its performance relative to the CT-cyclone.

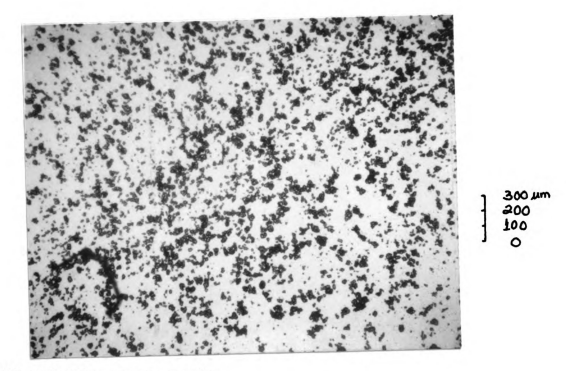
Colman compared the separation performance of the CT-cyclone (L/Dc = 24) and the SCI-cyclone (L/Dc = 14) using a dispersion of polypropylene particles (  $f_D/f_C \approx 0.90$ , mean particle size of 40 microns) in water (see Figure 18 Colman, 1981). At an inlet velocity of 5 m/s, the CT-cyclone (E'  $\approx 0.89$ ) only achieved a 5% higher underflow purity than the SCI-cyclone (E'  $\approx 0.84$ ). The performance of the two designs is thus more comparable when separating a dispersion with a larger density difference. When comparing the hydrocyclones at equal length to diameter ratios, the difference in separation performance would be expected to be even smaller.

Figures 5.7a and 5.7b show optical microscope photographs of the feed and underflow streams for the CT-cyclone at a magnification of approximately 40X. The photographs represent samples taken from the

Figure 5.7. Comparison of particle size distributions for the (a) feed and (b) underflow streams in the CT-cyclone. Photos represent approximately 40% enlargement of samples taken when operating at  $u_F = 3.9$  m/s,  $S_0 = 0.13$ , and  $y_F \approx 250$  wppm. The scale next to the figures can be used to estimate particle sizes.



(a) feed stream sample



(b) underflow stream sample

Figure 5.7.

CT-cyclone operating at  $u_F = 3.9$  m/s,  $S_0 = 0.13$ , and a feed concentration of  $y_F \approx 250$  wppm. The scale next to the photos can be used to estimate particle sizes. The samples were allowed to separate gravimetrically and do not represent the concentrations existing in the streams during hydrocyclone operation. Although the particles are not spherical in shape, Colman and Thew [1983] showed that application of the shape factor correction did not significantly change the shape of or position of the grade efficiency curve when plotted against particle size.

A comparison of Figures 5.7a and 5.7b shows the underflow of the CT-cyclone to be free of most of the large particles existing in the feed. However, the presence of some large particles (80-100 microns) in the underflow suggests that the side-wall boundary layer does exist in this design.

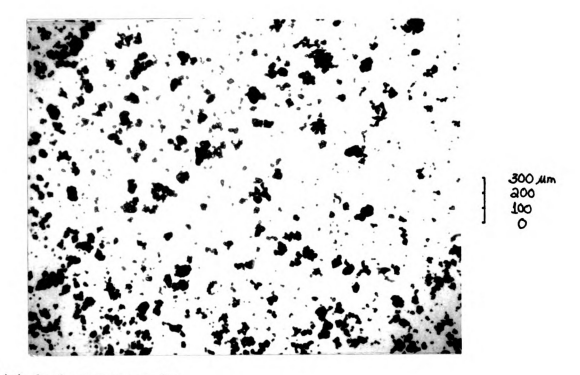
Figures 5.8a and 5.8b show the corresponding photographs for the feed and underflow streams for the SCI-cyclone operating at the same inlet velocity and feed concentration, but with  $S_0 = .09$ . Note the existence of many more large particles in the underflow stream, Figure 5.8b, as compared with Figure 5.7b for the CT-cyclone. This is consistent with the underflow purity measurements. These photographs suggest that the SCI-cyclone allows for a larger side-wall boundary layer flow than does the CT-cyclone.

#### 5.4.5. Conclusions

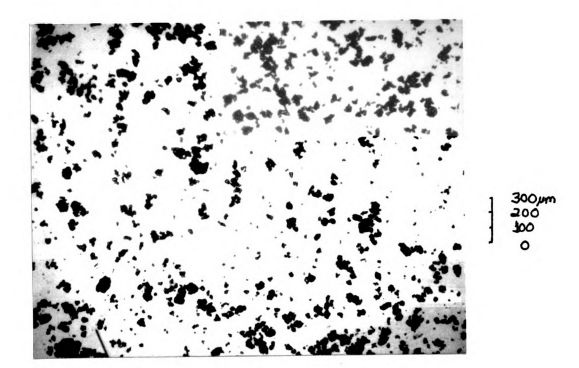
The following conclusions are based on the experimental data presented in Sections 5.4.2 - 5.4.4.

(1) Both hydrocyclone designs exhibited a dynamic instability in the

Figure 5.8. Comparison of particle size distributions for the (a) feed and (b) underflow streams in the SCI-cyclone. Photos represent approximately 40X enlargement of samples taken when operating at  $u_F = 3.9$  m/s,  $S_0 = 0.09$ , and  $y_F \approx 250$  wppm. The scale next to the figures can be used to estimate particle sizes.



(a) feed stream sample



(b) underflow stream sample

Figure 5.8.

reverse flow vortex for the range of inlet velocities studied. Operation of the hydrocyclones outside the conditions for stable reverse flow vortex behavior results in little or no separation of the dispersed phase.

- (2) The higher underflow purity and lower pressure loss for the CT-cyclone indicate that it is a better separator for the HDPE dispersion used in the present work. However, comparison with Colman's data (see Figure 18 Colman, 1981) indicates that the cyclones would be expected to perform comparably when separating a dispersion with a larger density difference and using equal length to diameter ratios.
- (3) The pressure loss data and separation performances indicate different hydrodynamic structures for the two hydrocyclone designs.
- (4) The underflow pressure loss coefficients for both designs were found to be independent of the inlet Reynolds number, indicating that the pressure losses are due primarily to centrifugal head losses. This was not true for the overflow pressure losses, where viscous losses may become important in the small overflow orifice.
- (5) Photographs of samples taken from the underflow streams of both designs at the same inlet velocity indicate that some large particles are lost directly to the underflow from the side-wall boundary layer short circuit flow.

## 5.5. Comparison of Theoretical and Experimental Results

#### 5.5.1 Centrifugal head calculations

The pressure drop data from Figure 5.5 can be used to estimate values for the hydrodynamic parameters n and m. The radial component of

the equation of motion in cylindrical coordinates for an inviscid fluid at steady state can be approximated by

$$\frac{\partial P}{\partial r} = \sqrt{c u e^2 / \hat{r}}$$
 (5-4)

The centrifugal acceleration has been assumed to be the dominant effect for momentum transport and the effect of external potential fields have been neglected. Bradley (see p.89, 1965) concluded that the observed pressure losses across a hydrocyclone are due almost entirely to the centrifugal head, which is calculated by separating and integrating Eq. (5-4) over the appropriate radial limits. An expression for the underflow pressure loss coefficient  $C_{Pu}$  can be found by substituting Eqs. (3-15a) and (3-15b) into Eq. (5-4) and performing the integration from  $\hat{r} = \hat{r}_{C}$  (the hydrocyclone wall radius) to  $\hat{r} = \hat{r}_{U}$  (the underflow radius), giving

$$C_{pu} \approx m^2 (r_{U}^{-2n} - 1)/n$$
 (5-5)

Eq. (5-5) shows no explicit dependence on the inlet Reynolds number Ref.

The underflow pressure loss coefficient for both designs were also found to be independent of  $Re_F$  (see Figure 5.5). It is possible that the parameters m and n vary with  $Re_F$  in such a way that  $C_{P\,U}$  remains constant over the range of inlet velocities. However, it would seem more plausible for each of these parameters to be constants, independent of  $Re_F$ .

If the values of n=0.5 and m=0.5 (these were the "base values" used in the illustrative trajectory calculations of Chapter 4) are substituted into Eq.(5-5), a value of  $C_{pu}=1.5$  results. This is far below the values of  $C_{pu}$  observed for both hydrocyclone designs. A value of  $C_{pu}=15$  results for n=1 (a free vortex) and m=1. This value should

be an upper bound on the centrifugal head for both hydrocyclone designs. Referring to Figure 5.5, this is true for the CT-cyclone ( $C_{Pu} \approx 10$ ), but not for the SCI-cyclone ( $C_{Pu} \approx 18$ ). This result indicates that other factors are involved in the pressure losses across the SCI-cyclone, including the possibility of recirculation flows caused by the continuance of the 10° taper to the underflow diameter.

Because the underflow pressure loss coefficient for both designs is approximately constant over the range of inlet velocities studied, a unique relationship between n and m can be found by solving Eq.(5-5) for m, giving

$$m = \left[ nC_{pu}/(r_{u}^{-2n} - 1) \right]^{1/2}. \qquad (5-6)$$

Substituting  $r_n = 1/4$ ,  $C_{Pu} \approx 10$  (for the CT-cyclone), and requiring  $m \le 1$  places a lower bound of approximately n = 0.75 on the free-like vortex power index. Data from Dabir [1983] and Colman [1981] indicate that this value for n is the maximum expected in liquid hydrocyclones. Using this value of n in Eq.(5-6) results in a value of  $m \approx 1$  for the CT-cyclone. The result of this analysis is that the pressure drop data of Figure 5.5 suggests significantly larger values for these two parameters than was used in the centrifugal efficiency calculations in Chapter 4. Using a value of  $C_{Pu} \approx 18$  for the SCI-cyclone, no values of n or m less than unity could be found to satisfy Eq.(5-6).

#### 5.5.2 Estimation of the centrifugal efficiency

Colman reported separation data for the CT-cyclone (with the same nominal dimensions as the CT-cyclone used in this study) when

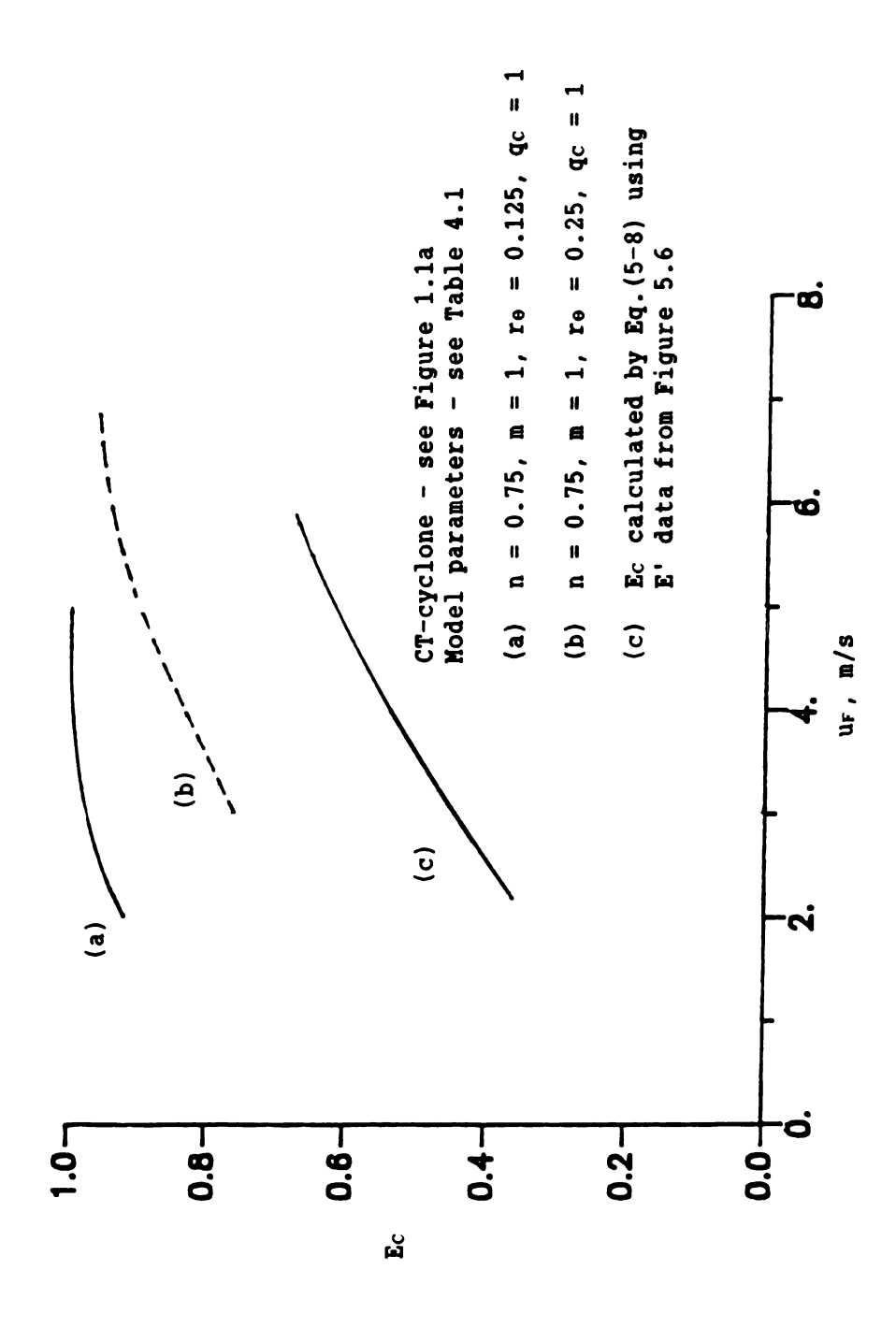
separating a polypropylene powder dispersed in water (  $\phi_0/\phi_c$  = 0.90 and a mean particle size of about 40 microns, see Figure 19 Colman, 1981). This data suggests an asymptotic value of 90% for the underflow purity at an overflow ratio  $S_0 \approx 0.10$ . Assuming that the centrifugal efficiency has reached an asymptotic value of  $E_c$  = 1 in Colman's experiments, Eq.(2-35) can be used to estimate the side-wall short circuit ratio giving

$$S_{SW} = [1 - (E')_{E_c} = 1] (1 - S_0).$$
 (5-7)

Substituting  $S_0$  = 0.10 and  $(E')_{E}$  = 1 = 0.90 into Eq.(5-7) gives  $S_{SW}$  = 0.09. The centrifugal efficiency of the CT-cyclone corresponding to the underflow purities shown in Figure 5.6 can be estimated by solving Eq.(2-36) for Ec, with  $S_{SW}$  = 0.09 and  $S_0$  = 0.13 (see Figure 5.6), giving

$$\mathbf{E}_{\mathbf{C}} = \mathbf{1.12E'} . \tag{5-8}$$

The centrifugal efficiency for the CT-cyclone can be calculated using the particle trajectory model, with the values  $\mathbf{m}=1$  and  $\mathbf{n}=0.75$  found in Section 5.5.1. The remaining hydrodynamic/dispersion parameters are defined by Table 4.1 and the size density distribution for the dispersion is given in Figure B.3. Figure 5.9 shows the result of this calculation (curve a) as well as a plot of the experimentally obtained values of  $\mathbf{E}_{\mathbf{C}}$  given by Eq.(5-8) (curve c). Note that the parameter  $\mathbf{q}_{\mathbf{C}}$  (the fraction of the feed flow rate experiencing centrifugal separation) has been taken equal to unity, although the side-wall short circuit ratio  $\mathbf{S}_{\mathbf{S}\mathbf{W}}$  was assumed to be equal to 0.09. The centrifugal efficiency calculated using  $\mathbf{q}_{\mathbf{C}}=1$  is a lower bound for the case  $\mathbf{S}_{\mathbf{S}\mathbf{W}}=0.09$  (giving



Theoretical vs. experimentally estimated centrifugal efficiency for the CT-cyclone. Figure 5.9.

 $q_C < 1$ ). This is due to the smaller value of  $q_C$  resulting in an increased value of  $N_1$  in Eq.(4-4), giving higher centrifugal grade efficiencies at all particle sizes (see Eqs.(4-7) and (4-8)). So for values of  $q_C < 1$ , the centrifugal efficiency will reach a value of unity even quicker than for curve (a) of Figure 5.8.

Curves (a) and (c) of Figure 5.8 do not show good agreement. Curve (a) was calculated using the position of maximum tangential velocity  $r_0 = 0.125$ , as suggested by the data of Dabir [1983] and Colman (see Figures 34 and 36 Colman, 1981). Curve (b) shows the theoretically calculated centrifugal efficiency curve corresponding to  $r_0 = 0.25$ , which still does not show good agreement. The difference between the theoretically calculated centrifugal efficiency and the experimentally implied centrifugal efficiency may be due to some poor assumptions in the particle trajectory model.

Based on the centrifugal head estimated from Eq.(5-5), the pressure loss data for the CT-cyclone (see Figure 5.5) resulted in values of n ≈ 0.75 and m ≈ 1, which are higher than the values given in Table 4.1. For these higher values of n and m, a possibility that would give closer agreement between the theoretically calculated and experimentally implied centrifugal efficiency curves of Figure 5.8 is for re to be greater than 0.25. However, this requirement corresponds to the existence of a forced vortex in the cylindrical underflow section of the CT-cyclone. LDA studies of Colman show that even for a cylindrical hydrocyclone, the tangential velocity profile is a combination of free-like vortex and forced vortex throughout the entire hydrocyclone length (see Figure 36 Colman, 1981). Therefore, it does not seem likely that

the position of maximum tangential velocity would occur at a radius greater than the underflow radius.

The decay of angular momentum, not accounted for in the particle trajectory model, may play an important role in long hydrocyclones used in light dispersion separations (see Regehr, 1962). The tangential velocity profile for the free-like vortex portion in the hydrodynamic model was assumed to be independent of axial position. A more realistic model may be

$$u_{e} = k(z) \stackrel{\wedge}{r}_{-n} \qquad \stackrel{\wedge}{r}_{e} \leq \stackrel{\wedge}{r} \leq \stackrel{\wedge}{r}_{w}(z) , \qquad (5-9)$$

where the coefficient k(z) denotes dependence of the tangential velocity upon axial position. Note that Eqs.(3-15a) and (3-15b) used a constant value of the power law coefficient,  $k = mu_F \hat{r}_C{}^n$ . By allowing k to be a function of axial position, the magnitude of the tangential velocity can decrease as angular momentum decays (with increasing axial position), while preserving the radial location of the maximum value of the tangential velocity,  $\hat{r}_e$ .

One of the main assumptions in the particle trajectory model is that the cylindrical swirl chamber acts as a mixing chamber, giving a homogeneous distribution of particles across a radial line from the capture surface to the hydrocyclone wall. Although flow visualization studies seem to support this assumption, detailed information on dispersed phase distribution upon entry into the hydrocyclone is not available. Other mixing assumptions could be made, giving different results. For example, if all the dispersed phase particles were assumed to enter the swirl chamber at the wall radius  $\hat{\mathbf{r}} = \hat{\mathbf{r}}_{\mathrm{C}}$ , the resulting centrifugal

grade efficiency curve would resemble a step function. Particles smaller than the  $x_{100}$  size (i.e., the size for which the centrifugal grade efficiency equals 100%) have no chance to be captured in the reverse flow vortex, while particles equal to or larger than the  $x_{100}$  size would be captured at an efficiency of 100%. A comparison between the two mixing models gives very different results. When the mixing chamber model is used with the centrifugal grade efficiency curve for the CT-cyclone at  $u_F = 5$  m/s (see Figure 4.4), the computer program in Appendix A.3 calculates a centrifugal efficiency  $E_C = 0.70$  for the HDPE dispersion. The wall entry mixing model, using a step function for the centrifugal grade efficiency (occurring at  $x_{100} = 60$  microns in Figure 4.4), gives an analytic result for the centrifugal efficiency, i.e.

$$E_C = 1 - F_F (60 \text{ microns})$$
 (5-10)

Figure B.2 gives  $F_F$  (60 microns) = 0.68 resulting in a centrifugal efficiency  $E_C$  = 0.32. Because the centrifugal efficiency is so different for the two mixing models, this assumption is a critical one.

A final possibility to be considered is that the measured pressure loss coefficient does not represent the centrifugal head losses. Colman measured the wall pressure in a cylindrical hydrocyclone at several different axial positions (see Figure 51 Colman, 1981). The data suggests that the underflow pressure loss coefficient remains constant over much of the length of the hydrocyclone, but begins to decrease in the cylindrical underflow section due to frictional losses. If pressure losses along the wall in the CT-cyclone due to wall friction are significant, then the centrifugal head would be lower than the observed

underflow pressure loss coefficient, resulting in lower values for n and m in Eq.(5-6). This may result in closer agreement between the theoretically calculated and experimentally estimated centrifugal efficiencies for the CT-cyclone.

## 5.6. Application of the Cut Size Correlation

An estimate of the efficiency of the CT- and SCI-cyclones when separating a dispersion with a density difference typical of oil-water dispersions will be made using the cut size correlation introduced in Section 4.3.

A set of hydrodynamic parameters (n, m, and  $r_0$ ) can be chosen for the CT- and SCI-cyclones so that the centrifugal efficiency calculated by the particle trajectory model approximates the underflow purity data for each design given in Figure 5.6. The set of parameters for which this occurs was found by trial and error, using the values defined in Table 4.1 for the remaining hydrodynamic and dispersion parameters. Using this approach, the values m = 0.5, n = 0.5, and  $r_0 = 0.16$  resulted in a centrifugal efficiency of 0.45 for the SCI-cyclone at  $u_F = 5$  m/s, compared to an observed underflow purity of E' = 0.42. Likewise, for the CT-cyclone, the values m = 0.5, n = 0.5, and  $r_0 = 0.15$  resulted in a value of  $E_c = 0.57$  at  $u_F = 5$  m/s compared to the observed value of E' = 0.55. These values of m, n, and  $r_0$  are used to approximate the underflow purity using the centrifugal efficiency and do not necessarily represent the hydrodynamics occurring in either hydrocyclone.

Using these values for m, n, and  $r_0$ , the  $N_3$  (50) -  $N_4$  (50) relationships can be constructed for each design as discussed in Section 4.3.

Figure 5.10 shows the resulting curves for each hydrocyclone. The enlarged dot on each curve represents the values of  $N_3^{(50)}$  and  $N_4^{(50)}$  corresponding to the cut size  $x_{50}$  at  $u_F = 5$  m/s  $((x_{50})_{CT} = 47$  microns,  $(x_{50})_{SCI} = 50$  microns) for the HDPE dispersion. Figure 5.10 can be used to estimate the underflow purity that would be achieved by each design for an oil-water dispersion with the same size density distribution as the HDPE powder used in the present study.

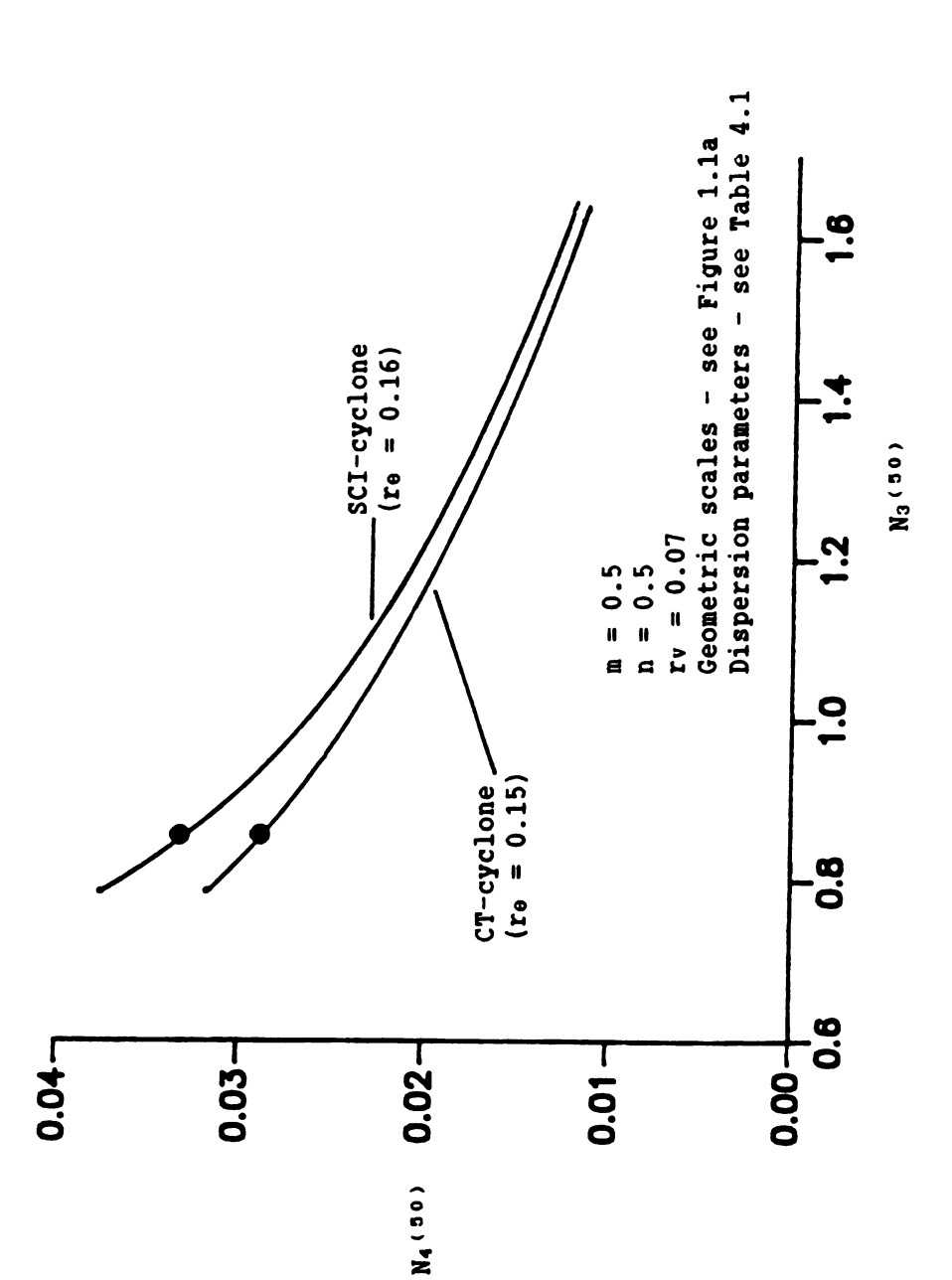
The value of  $N_3$  (50) is the same for each hydrocyclone design and is calculated using Eq. (4-19)

$$N_{3}^{(50)} = \frac{\left[\frac{(1 - \rho_{D}/\rho_{C}) m^{2} \gamma_{C}}{18 \hat{r}_{C} u_{F}}\right]^{1/3}}{q_{C} r_{F}^{2} \hat{r}_{C}/\hat{L}}$$
(4-19)

The model parameters corresponding to the conditions to be evaluated are:  $\ell_D/\ell_C = 0.90$ ,  $\nu_C = 10^{-6} \, \text{m}^2/\text{s}$ ,  $\hat{r_C} = .038 \, \text{m}$ ,  $\nu_F = 5 \, \text{m/s}$ ,  $\nu_F = 0.25$ ,  $\hat{L}/\hat{r_C} = 44$ ,  $\nu_F = 0.5$ , and  $\nu_F = 1.5$  Substituting these values into Eq.(4-17) gives  $\nu_F = 1.366$ . The corresponding  $\nu_F = 1.366$  values can be read from Figure 5.10, giving 0.0174 and 0.0160 for the SCI- and CT-cyclones, respectively. To find the cut size for each design when separating the new dispersion, Eq.(4-20) is solved for  $\nu_F = 1.366$  giving

$$x_{50} = \left[ \frac{18N_4^{(50)} \gamma_{C^2} r_C}{(1 - \rho_D/\rho_C) (mu_F)^2} \right]^{1/3}.$$
 (5-11)

Eq.(5-11) can be used to estimate the  $x_{50}$  values for the two hydrocyclones assuming that the new dispersed phase density does not affect the hydrodynamics of either design. Substitution of the N<sub>4</sub>(50) values found from



 $N_3^{(50)}$  -  $N_4^{(50)}$  relationship using hydrodynamic parameters based on the underflow purities of the CT- and SCI-cyclones from Figure 5.6. Figure 5.10.

Figure 5.10 and the model parameters used in calculating N<sub>3</sub>(50) gives  $(x_{50})_{CT} \approx 26$  microns and  $(x_{50})_{SCT} \approx 27$  microns.

These values for the cut sizes can be used to calculate the centrifugal efficiencies by assuming the centrifugal grade efficiency can be approximated by a step function occurring at the cut size  $x_{50}$ . This representation for the centrifugal grade efficiency curve is not calculated using the trajectory model, but is a good approximation to the curves obtained by the model, especially at high inlet velocities (see Figure 4.4). The evaluation of the centrifugal efficiency (see Eq. (2-27)) can then be found analytically giving

$$E_C \approx 1 - F_F(x_{50})$$
 (5-12)

Using the experimental data from Figure B.2 to find the value of the cumulative distribution at these values of  $x_{50}$  gives

$$(E_C)_{SCI} \approx (E')_{SCI} = 1 - 0.13 = 0.87$$
 (5-13)

and

$$(E_C)_{CT} \approx (E')_{CT} = 1 - 0.12 = 0.88$$
 (5-14)

Thus, for a dispersion with a larger density difference, the two hydrocyclone designs are expected to perform comparably. Colman reported a a value of E' = 0.89 at  $u_F \approx 5$  m/s for the CT-cyclone when separating an HDPE dispersion ( $f_D/f_C = 0.90$ ) with approximately the same size density distribution as that used here (see Figure 45 Colman, 1981). This agrees well with the estimated value given by Eq. (5-14). The 1% difference estimated for the underflow purity of the two hydrocyclones given by Eqs. (5-13) and (5-14) reflects an equal length to diameter ratio. This

result would be anticipated when extrapolating the data given by Colman for the comparison of the performance of the CT- and SCI-cyclones (see Section 5.4.4).

#### CHAPTER 6

#### CONCLUSIONS

The major conclusions of this study can be summarized as follows:

(1) The results of flow visualization, pressure drop measurements, and underflow purity determination suggest that the hydrodynamics occurring in the SCI- and CT-cyclones are different. Flow visualization studies showed an incoherence in the particle core near the apex of the large taper section in the SCI-cyclone, indicating a remixing of fluid at that axial position. No such behavior was observed in the CT-cyclone, the reverse flow vortex appearing to be coherent over the entire hydrocyclone length. Compared to the sharper contraction of the fluid to the underflow diameter in the SCI-cyclone, the gradual taper of the CT-cyclone appears to maintain high swirl without upsetting the coherence of the particle core. The pressure losses in the SCI-cyclone were nearly double those of the CT-cyclone, and it exhibited an 18% lower underflow purity when separating the HDPE dispersion at an inlet velocity of 5 m/s. This pressure drop - efficiency behavior is in contrast to heavy dispersion hydrocyclones where higher efficiencies result from larger pressure drops (see p.87 Bradley, 1965), indicating a source of inefficiency in the SCIcyclone. Because the two designs were geometrically identical in all other respects, the difference in the taper angle \$\beta\$ appears to be the

cause of the different hydrodynamic environments in the two cyclones.

- (2) Based on the scaling calculation presented in Section 6.2, the SCI-and CT-cyclones would be expected to give comparable underflow purities for dispersions where  $\rho_D/\rho_C \approx 0.90$ . For this conclusion to be valid in the separation of a liquid-liquid dispersion, the effects of droplet breakup in the SCI-cyclone should be investigated. If the process stream were naturally available at high pressures, as on offshore oil platforms, the higher pressure loss for the SCI-cyclone would not necessarily be a disadvantage.
- (3) In the context of the particle trajectory model, it was not possible to find a set of hydrodynamic parameters n, m, and re that were consistent with both the pressure losses and underflow purities observed for the CT-cyclone. This result suggests that some of the assumptions in the model may need to be modified. In particular, the decay of angular momentum is likely to be significant for long hydrocyclones used in light dispersion separations, and should be accounted for in the trajectory model. Also, the mixing assumption introduced in Section 2.3 appears to give high centrifugal efficiencies. On the other hand, the assumption that the dispersed phase particles concentrate near the outer wall upon entry appears to give low centrifugal efficiencies, suggesting that the actual mixing conditions lies somewhere between these two extremes.
- (4) Dynamic instabilities in the reverse flow vortex were observed in both hydrocyclone designs over periods as short as ten seconds and as long as twenty minutes. The long time scales over which the dynamic

instabilities of the reverse flow vortex could occur shows the need for carefully mapping out the stable operating regimes for the light dispersion hydrocyclones. The cause of this instability is unknown, but it may be due to insufficient back pressure to drive the reverse flow vortex through the overflow orifice or from asymmetric flow conditions in the swirl chamber resulting from the use of a single inlet design. It is also possible that submerging the overflow line in the recycle tank caused disturbances to be propagated through the overflow valve to the overflow orifice, affecting the stability of the reverse flow vortex.

- (5) Photographs of samples of the feed and underflow streams (see Figure 5.7) suggest the existence of the side-wall boundary layer short circuit flow in both hydrocyclone designs tested. The appearance of more large particles in the underflow stream for the SCI-cyclone indicates that the short circuit effect may be larger in this design.
- sary, especially for large particles. The use of Stoke's law at the highest particle Reynolds numbers occurring in the model flow field results in overestimating particle drift velocities by a factor of two (see Figure 4.3a). When the density difference between continuous and dispersed phase is larger than that used in the calculations presented here, the error incurred by the use of Stokes' law will be even greater.

#### CHAPTER 7

## RECOMMENDATIONS

The following recommendations for further research are made:

- (1) The existence of dynamic instabilities in the reverse flow vortex is a new result. This phenomenon should be the focus of a separate study to quantify its behavior in the CT-cyclone and to study its causes.
- (2) The SCI-cyclone should be tested using a dispersion for which  $f_D H_C = 0.9$  to validate the scaling calculation of Section 5.6 that the SCI- and CT-cyclones would achieve comparable underflow purities when separating this type of dispersion.
- (3) Colman [1981] compared the CT- and SCI-cyclones holding the overflow ratio So fixed for selected feed velocities while the overall
  hydrocyclone lengths and volumes were different. In the present study,
  these two designs have been compared at the same overall length, while
  the hydrocyclone volumes and overflow ratios were different. Experimental comparison of the SCII- (see Figure 1.1a) and CT-cyclones would provide a comparison of double- and single-cone hydrocyclones for which the
  lengths, volumes, and overflow ratios were the same. With a mean fluid
  residence time equal to that of the CT-cyclone and a shallower taper angle
  to eliminate possible secondary flows, the SCII-cyclone may perform

comparable to the CT-cyclone when separating the HDPE dispersion used in this study. Differences between the separation performance of these two designs could be attributed to the fine taper angle in the CT-cyclone.

- (4) The particle trajectory model presented in this study requires more detailed information on the tangential velocity profile as a function of axial position, especially with regard to the decay of angular momentum. A determination of the tangential velocity profile at both upstream and downstream axial positions in the CT-cyclone using LDA is recommended to quantify the decay of angular momentum and arrive at a better model for the tangential velocity in the free-like vortex region.
- (5) A study of the wall pressure profile in the CT-cyclone is suggested to determine the relation of the measured underflow pressure loss coefficient to the centrifugal head losses occurring in the hydrocyclone.

  This will help to quantify the hydrodynamic parameters n (the power index for the free-like vortex) and m (the inlet velocity conversion factor) used in the particle trajectory model.
- (6) The mixing model assumption was shown to be critical. Although flow visualization in the CT- and SCI-cyclones indicated that the swirl chamber acts to mix the incoming feed stream, no quantitative data is available. A study of the distribution of the dispersed phase particles upon entry into the CT-cyclone using high speed cinematography is recommended to clarify this aspect of the separation process.
- (7) The short circuit flows affecting separation performance are literally unexplored. Techniques such as LDA could be used to determine the nature and extent of these flows and would greatly improve the

understanding of the hydrocyclone separator. A focus on the side-wall boundary layer in long hydrocyclones is recommended to understand its role in the separation process.

(7) The use of hydraulic water addition in the cylindrical underflow section may eliminate the effect of the side-wall short circuit flow. This strategy should be used in the CT-cyclone when separating a dispersion for which  $C_D/C_C = 0.90$  and the size distribution is similar to that of the HDPE powder used in this study. If the attainment of underflow purities near 100% is found to be possible using this strategy, the role of the end-wall short circuit flow would be understood better.

# APPENDIX A

COMPUTER PROGRAMS

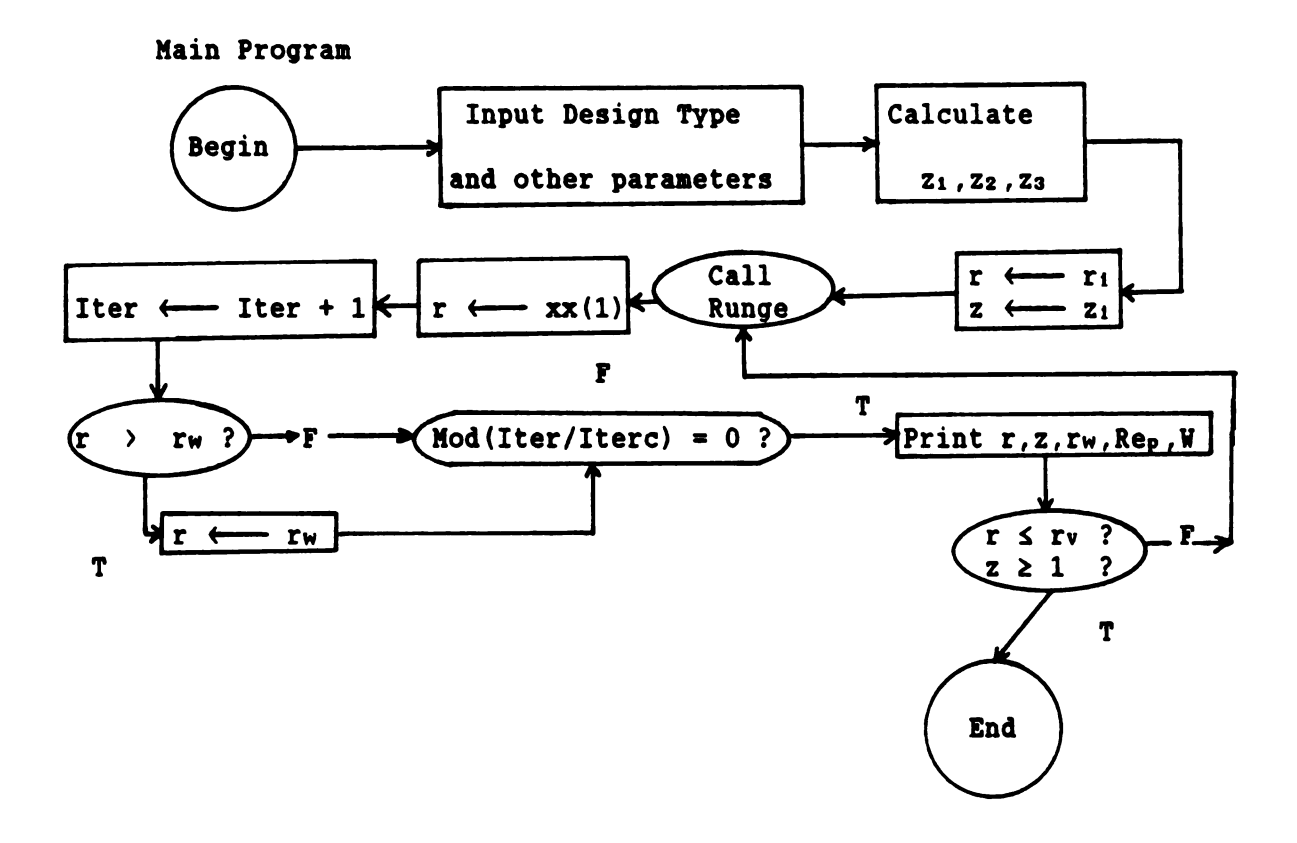
## APPENDIX A

#### COMPUTER PROGRAMS

# A.1 Particle Trajectory Calculation

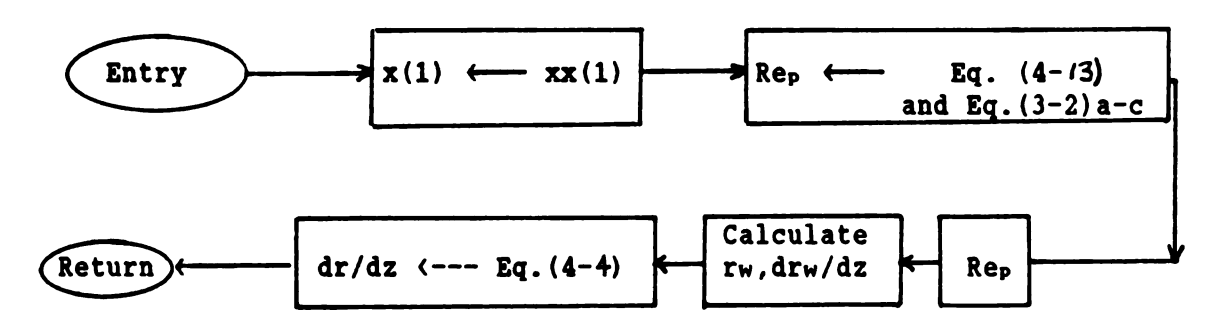
The objective of this section is to solve the initial value problem described in Section 4.1. The Runge-Kutta 4th order method (see p.359 Boyce and Diprima, 1977) is used to numerically integrate Eq.(4-3), a first order nonlinear ODE. The solution strategy discussed in Section 4.1 is outlined in flow chart form in Figure A.1.1. This is followed by the program code with typical output. This program uses a data file named TRJ.DAT that must be created by the user to input the problem parameters.

#### FLOW DIAGRAM FOR PROGRAM TRJ.FOR



Subroutine Runge uses the Runge-Kutta 4th order algorithm to calculate dr/dz. It calls Subroutine Aux to evaluate Eq. (4-3).

## Subroutine Aux



```
C
      PROGRAM TRJ.FOR
C
C
       LDC
             = LENGTH TO DIAMETER RATIO L/Dc
C
             = TOTAL HYDROCYCLONE LENGTH
       LCDC = LENGTH OF CYCLINDRICAL SWIRL CHAMBER Lc/Dc
C
C
             = DIAMETER IN CT-CYCLONE WHERE FINE TAPER BEGINS D/Dc
       DDC
C
       DODC = OVERFLOW DIAMETER RATIO D_0/D_C
C
       LA
             = DIMENSIONLESS LENGTH OF LARGE TAPER SECTION L_{\alpha}/L
C
       LB
             = DIMENSIONLESS LENGTH OF SMALL TAPER SECTION Lo/L
C
      LU
             = DIMENSIONLESS LENGTH OF TAILPIPE SECTION Lu/L
C
      ALPHAD= LARGE TAPER ANGLE a (DEG)
C
       BETAD = SMALL TAPER ANGLE \beta (DEG)
C
      RU
             = UNDERFLOW RADIUS ru
C
      RTH
             = CHANGEOVER RADIUS (FREE-LIKE VORTEX TO FORCED VORTEX) re
C
      EN
             = POWER INDEX OF FREE-LIKE VORTEX n
C
      FC
             = DIMENSIONLESS RADIAL ACCELERATION Fc
C
      R
             = RADIAL COORDINATE, 0 < r < 1 = r_c
C
      RI
             = INITIAL PARTICLE RADIAL COORDINATE ri
C
       Z
             = AXIAL COORDINATE, 0 < z < 1
C
      ZI
             = INITIAL PARTICLE AXIAL COORDINATE Z1
C
      Z1
            = AXIAL POSITION OF START OF 1ST TAPER SECTION Z<sub>1</sub>
C
      Z2
             = AXIAL POSITION OF END OF 1ST TAPER SECTION Z2
             = AXIAL POSITION OF BEGINNING OF 2ND TAPER SECTION Z<sub>3</sub>
C
      Z3
C
      RW
             = WALL RADIAL POSITION rw
C
      RWP
             = RATE OF CHANGE OF WALL POSITION WITH AXIAL LENGTH drw/dz
C
      DZ
             = AXIAL STEP SIZE
C
      XX
             POSITION VECTOR FOR INTEGRATOR
C
      N1
             = DIMENSIONLESS GROUP IN DIFFERENTIAL EQUATION N<sub>1</sub>
             = DIMENSIONLESS GROUP IN REYNOLDS NUMBER CALCULATION
C
      N2
C
      REP
             = PARTICLE REYNOLDS NUMBER Rep
C
      WREP = DRAG COEFFICIENT RATIO W(Rep)
C
      INTLDC= AXIAL POSITION DENOTING VORTEX REVERSAL
C
      I1
             = INTEGER DENOTING CYCLONE MODEL
C
C
                1 = SHORT CYLINDER AND CONE (L<sub>B</sub> = L<sub>U</sub> = 0)
C
                2 = SINGLE CONE DESIGN
C
                3 = DOUBLE CONE DESIGN
C
C
       ITER = COUNTER
C
       ITERC = COUNTER; = # ITERATIONS/PRINTOUT
C
C
C$DEBUG
      INTEGER I1, ITER, ITERC
      REAL*8 N1,N2
      REAL*8 LDC, LCDC, DDC, ALPHA, BETA, ALPHAD, BETAD, RU, RTH, EN, R, RI, Z, ZI
      REAL*8 Z1,Z2,Z3,DODC,DZ,XX(2),RF,INTLDC,LA,LB,LU,RV,REP,RW,RWP,WREP
      COMMON /AUX1/ N1, N2, RTH, EN, WREP, REP, LDC, RWP, RW
      COMMON /AUX2/ I1,Z1,Z2,Z3,ALPHA,BETA,DDC,RU,RV,RF,DODC
```

```
OPEN(2, FILE = 'TRJ.PRN', STATUS = 'NEW')
     OPEN(3, FILE = 'TRJ.DAT', STATUS = 'OLD')
C
C
     READ(3,*)I1,LDC,LCDC,DDC,ALPHAD,BETAD
     READ(3,*)RU,RTH,EN,DZ,RF,INTLDC,DODC
     READ(3,*)RI,ZI
     READ(3,*)N1,N2,ITERC
     WRITE(*,'(1X,'' PARAMETERS ''/1X,''TYPE = '', I1/1X,''LDC = '', E12.
    14/1X, ''DDC = '', E12.4/1X, ''ALPHA = '', E12.4, '' DEG''/1X, ''BETA =
    1 '',E12.4,'' DEG''/1X,''RU = '',E12.4/1X,''RTH = '',E12.4/1X,''EN
    1 = '',E12.4/1X,''DZ = '',E12.4/1X,''RF = '',E12.4/1X,''INTLDC = ''
    1,E12.4/)') I1,LDC,DDC,ALPHAD,BETAD,RU,RTH,EN,DZ,RF,INTLDC
C
     WRITE(*,'(1X,''RI = '',E12.4/1X,''ZI = '',E12.4)')RI,ZI
C
     WRITE(*,'(1X,''DODC = '',E12.4)')DODC
     WRITE(2,'(1X,'' PARAMETERS ''/1X,''TYPE = '', I1/1X,''LDC = '', E12.
    14/1X,''DDC = '',E12.4/1X,''ALPHA = '',E12.4,'' DEG''/1X,''BETA =
    1 '', E12.4,'' DEG''/1X,''RU = '', E12.4/1X,''RTH = '', E12.4/1X,''EN
    1 = '',E12.4/1X,''DZ = '',E12.4/1X,''RF = '',E12.4/1X,''INTLDC = ''
    1,E12.4/)')I1,LDC,DDC,ALPHAD,BETAD,RU,RTH,EN,DZ,RF,INTLDC
C
     WRITE(2,'(1X,''RI = '',E12.4/1X,''ZI = '',E12.4)')RI,ZI
C
     WRITE(2, '(1X, ''DODC = '', E12.4)')DODC
     WRITE(*,'(1X,''N1 = '',E12.4/1X,''N2 = '',E12.4/1X,''ITERC = '',E1
    12.4)')
     WRITE(2,'(1X,''N1 = '',E12.4/1X,''N2 = '',E12.4/1X,''ITERC = '',E1
    12.4)')
  ALPHA = 2.D0*3.14159D0*ALPHAD/360.D0
     BETA = 2.D0*3.14159D0*BETAD/360.D0
C
C
C
C
C
C :
    C
     Z1 = LCDC/LDC
C
     IF (I1.EQ.3) THEN
      Z2 = Z1 + (1.D0-DDC)/(2.D0*LDC*DTAN(ALPHA))
       Z3 = Z2 + (DDC-RU)/(2.D0*LDC*DTAN(BETA))
        LA = (1.D0-DDC)/(2.D0*LDC*DTAN(ALPHA))
        LB = (DDC-RU)/(2.D0*LDC*DTAN(BETA))
         LU = 1.DO - LA - LB - LCDC/LDC
```

```
IF (LU.LT.O.DO) THEN
           WRITE(*,'(1X,''AXIAL LENGTH SCALES INCOMPATIBLE WITH TAPER
    1ANGLES''/1X,''INCREASE L/DC, ALPHA, OR BETA; OR DECREASE LCDC'')')
             STOP
             ENDIF
C
        ELSEIF (I1.E0.2) THEN
         22 = 21 + (1.D0-RU)/(2.D0*LDC*DTAN(ALPHA))
          LA = (1.D0 - RU)/(2.D0*LDC*DTAN(ALPHA))
          LU = 1.DO - LA - LCDC/LDC
C
            IF (LU.LT.O.DO) THEN
            WRITE(*,'(1X,''AXIAL LENGTH SCALES INCOMPATIBLE WITH TAPER
    1 ANGLE''/1X,'' INCREASE L/DC OR ALPHA; OR DECREASE LCDC'')')
             STOP
              ENDIF
          ELSE
C
     IF (I1.EQ.1) THEN
C
           ALPHA = DATAN((1.DO-RU)/(2.DO*LDC*(1.DO-Z1)))
           ALPHAD = ALPHA*360.DO/(2.D0*3.14159D0)
            Z2 = 1.D0
             WRITE(*,'(1X,''FOR TYPE 1, ALPHAD = '',E12.4)')ALPHAD
             WRITE(2,'(1X,''FOR TYPE 1, ALPHAD = '',E12.4)')ALPHAD
                   ENDIF
C
     ENDIF
C
     WRITE(*,'(1X,''Z1 = '',E12.4/1X,''Z2 = '',E12.4/1X,''Z3 = '',E12.4
    1/1X,''LA = '',E12.4/1X,''LB = '',E12.4/1X,''LU = '',E12.4)')Z1,Z2,
    1Z3, LA, LB, LU
     WRITE(2,'(1X,''Z1 = '',E12.4/1X,''Z2 = '',E12.4/1X,''Z3 = '',E12.4
    1/1X,''LA = '',E12.4/1X,''LB = '',E12.4/1X,''LU = '',E12.4)')Z1,Z2,
    1Z3, LA, LB, LU
C
C
     R = RI
     Z = ZI
     RW = RU
     RV = DODC
     WRITE(*,'(7X,''R'',16X,''Z'',16X,''RW'',15X,''REP'',12X,''WREP'')
    1')
     WRITE(2,'(7X,''R'',16X,''Z'',16X,''RW'',15X,''REP'',12X,''WREP'')
    1')
     ITER = 0
C
100
     CONTINUE
      C
     CALL RUNGE(R,Z,DZ,XX)
```

```
R = XX(1)
     IF (R.GT.RW) THEN
      R = RW
       ENDIF
C
C
           ******** SAVE TRAJECTORY POINTS ***********
C*
C
     ITER = ITER + 1
     IF (MOD (ITER, ITERC).EQ.0) THEN
      IF ((Z.LE.INTLDC).AND.(R.GT.RV))THEN
       WRITE(2, '(1X, 4(E12.4, 5X), E12.4)')R, Z, RW, REP, WREP
        WRITE(*,'(1X,4(E12.4,5X),E12.4)')R,Z,RW,REP,WREP
         ENDIF
           ENDIF
C
C
        IF ((Z.GE.INTLDC).OR.(R.LE.RV)) THEN
        IF (Z.LE.21) THEN
        WRITE(2, '(1X, 4(E12.4, 5X), E12.4)')R,Z,RW,REP,WREP
         WRITE(*,'(1X,4(E12.4,5X),E12.4)')R,Z,RW,REP,WREP
         GOTO 150
          ENDIF
     IF (Z.GE.INTLDC) GOTO 150
     GOTO 100
C
150
     END
C
    ******* INTEGRATING SUBROUTINE - 4TH ORDER RUNGE KUTTA ******
C************** VARIABLE LIBRARY ****************************
C
C
                 # OF DIFFERENTIAL EQS. IN SYSTEM TO BE EVALUATED
      NN
C
      SAVEX =
                 ORIGINAL VALUE OF DEPENDENT VARIABLE
C
      XP
                 DERIVATIVE VALUE
             =
C
                 INCREMENT FOR INDEPENDENT VARIABLE IN R-K ALGORITHM
      PHI
             =
C
      HH
                 DUMMY VARIABLE FOR STEP SIZE
       ***********
C
C
     SUBROUTINE RUNGE(R,Z,HH,XX)
     INTEGER NN
     REAL*8 SAVEX(2), XX(2), PHI(2), XP(2), R, Z, HH
C
     NN = 1
     XX(1) = R
     CALL AUX(XX,Z,XP)
     DO 501 J=1,NN
     SAVEX(J) = XX(J)
501 PHI(J) = XP(J)
     DO 502 J=1,NN
502
     XX(J) = SAVEX(J) + 0.5*HH*XP(J)
```

```
Z = Z + 5.D-1*HH
      CALL AUX(XX,Z,XP)
      DO 503 J=1,NN
      PHI(J) = PHI(J) + 2.0 \times XP(J)
503
      XX(J) = SAVEX(J) + 0.5 * HH * XP(J)
      CALL AUX(XX.Z.XP)
      DO 504 J=1,NN
     PHI(J) = PHI(J) + 2.0 \times XP(J)
504
    XX(J) = SAVEX(J) + HH \times XP(J)
      Z = Z + 5.D-1*HH
      CALL AUX(XX.Z.XP)
      DO 505 J=1,NN
      PHI(J) = PHI(J) + XP(J)
505
     XX(J) = SAVEX(J) + PHI(J)*HH/6.D0
      END
C
C
C
C
    SUBROUTINE AUX
    COMPUTATION OF DERIVATIVES FOR SUBROUTINE RUNGE
   USER MUST SUPPLY DERIVATIVE FUNCTIONS (XP'S) FOR NN 1ST ORDER ODE'S
C
C*********** VARIABLE LIBRARY ******************
C
C
       REP1 - REP3 = VALUES OF THE PARTICLE REYNOLDS NUMBERS IN THE
С
                     DIFFERENT FLOW REGIMES
C
       PART1
                   = FIRST PART OF DERIVATIVE dr/dz
C
       PART2
                   = SECOND PART OF DERIVATTIVE dr/dz
C
                   = DUMMY VARIABLE FOR AXIAL POSTION z
       ZE
C********************************
C
      SUBROUTINE AUX(X,ZE,XP)
      INTEGER 11
      REAL*8 N1,N2
      REAL*8 X(2), XP(2), RTH, EN, LDC, WREP, FC, RW, RWP
      REAL*8 REP, REP1, REP2, REP3, PART1, PART2
      REAL*8 ZE, Z1, Z2, Z3, ALPHA, BETA, DDC, RU, RV, RF, DODC
      COMMON /AUX1/ N1, N2, RTH, EN, WREP, REP, LDC, RWP, RW
      COMMON /AUX2/ I1,Z1,Z2,Z3,ALPHA,BETA,DDC,RU,RV,RF,DODC
C
C
      IF (X(1).GT.RTH) THEN
       FC = 1.D0/(X(1)**(2.D0*EN + 1.D0))
        ELSE
         FC = X(1)/(RTH**(2.D0*EN + 2.D0))
          ENDIF
C
      REP1 = N1*N2*FC
      REP2 = (1.2973D0*N1*N2*FC)**(1.D0/1.4D0)
      REP3 = DSQRT(54.5455D0*N1*N2*FC)
```

```
IF ((REP1.GE.O.DO).AND.(REP.LE.2.DO)) THEN
      REP = REP1
       WREP = 1.D0
        ELSEIF ((REP2.GT.2.DO).AND.(REP2.LE.500.DO)) THEN
        REP = REP2
          WREP = 1.2973DO/(REP**4.D-1)
          ELSE
           IF (REP3.GT.500.DO) THEN
            REP = REP3
             WREP = 54.5455DO/REP
              ENDIF
               ENDIF
C
C
C****
      C
C
  ****** DEFAULT FOR INITIAL POSITION ******************
C
     RW = 1.D0
     RWP = 0.D0
C
C
     ******************
C
     IF (I1.EQ.3) THEN
      IF((ZE.GT.Z1).AND.(ZE.LE.Z2))THEN
       RW = 1.DO - 2.DO*(DTAN(ALPHA))*(ZE-Z1)*LDC
        RWP = -2.D0*LDC*DTAN(ALPHA)
        ELSEIF ((ZE.GT.Z2).AND.(ZE.LE.Z3))THEN
          RW = DDC - 2.D0*(DTAN(BETA))*(ZE-Z2)*LDC
          RWP = -2.D0*LDC*DTAN(BETA)
C
           ELSE
            IF (ZE.GT.23) THEN
             RW = RU
              RWP = 0.D0
               ENDIF
                ENDIF
C
     ELSEIF (I1.EQ.2) THEN
      IF((ZE.GT.Z1).AND.(ZE.LE.Z2))THEN
       RW = 1.D0 - 2.D0*(DTAN(ALPHA))*(ZE-Z1)*LDC
        RWP = -2.D0*LDC*DTAN(ALPHA)
        ELSE
          IF (ZE.GT.Z2) THEN
          RW = RU
           RWP = 0.D0
C
            ENDIF
             ENDIF
C
    ELSE
C
    I1 = 1
```

```
IF (ZE.GT.Z1) THEN
       RW = 1.D0 - (1.D0 - RU) * (ZE-Z1) / (Z2 - Z1)
        RWP = (RU - 1.D0)/(Z2-Z1)
         ENDIF
     ENDIF
C
C
     PART1 = RW*RWP*(X(1)**2 - RV*RV)/(X(1)*(RW*RW-RV*RV))
     PART2 = -N1*FC*WREP*(RW*RW - RV*RV)
     XP(1) = PART1 + PART2
C
C
C *********** KEEPING TRAJECTORY '' IN BOUNDS '' *********
C
     IF ((X(1).GE.RW).AND.(ABS(XP(1)).LT.ABS(RWP))) THEN
      XP(1) = RWP
      ENDIF
C
C
  **********
C
C
     END
```

#### PROGRAM INPUT

TYPE = 3LDC = 0.2200E+02DDC = 0.5000E+00ALPHA = 0.1000E+02 DEGBETA = 0.7500E+00 DEGRU = 0.2500E+00RTH = 0.1250E+00EN = 0.5000E+00 DZ = 0.5000E-03 RF = 0.2500E+00INTLDC = 0.1000E+01RI = 0.1000E+01ZI = 0.4545E-01DODC = 0.7000E-01N1 = 0.3220E+01N2 = 0.7100E+01

#### PROGRAM OUTPUT

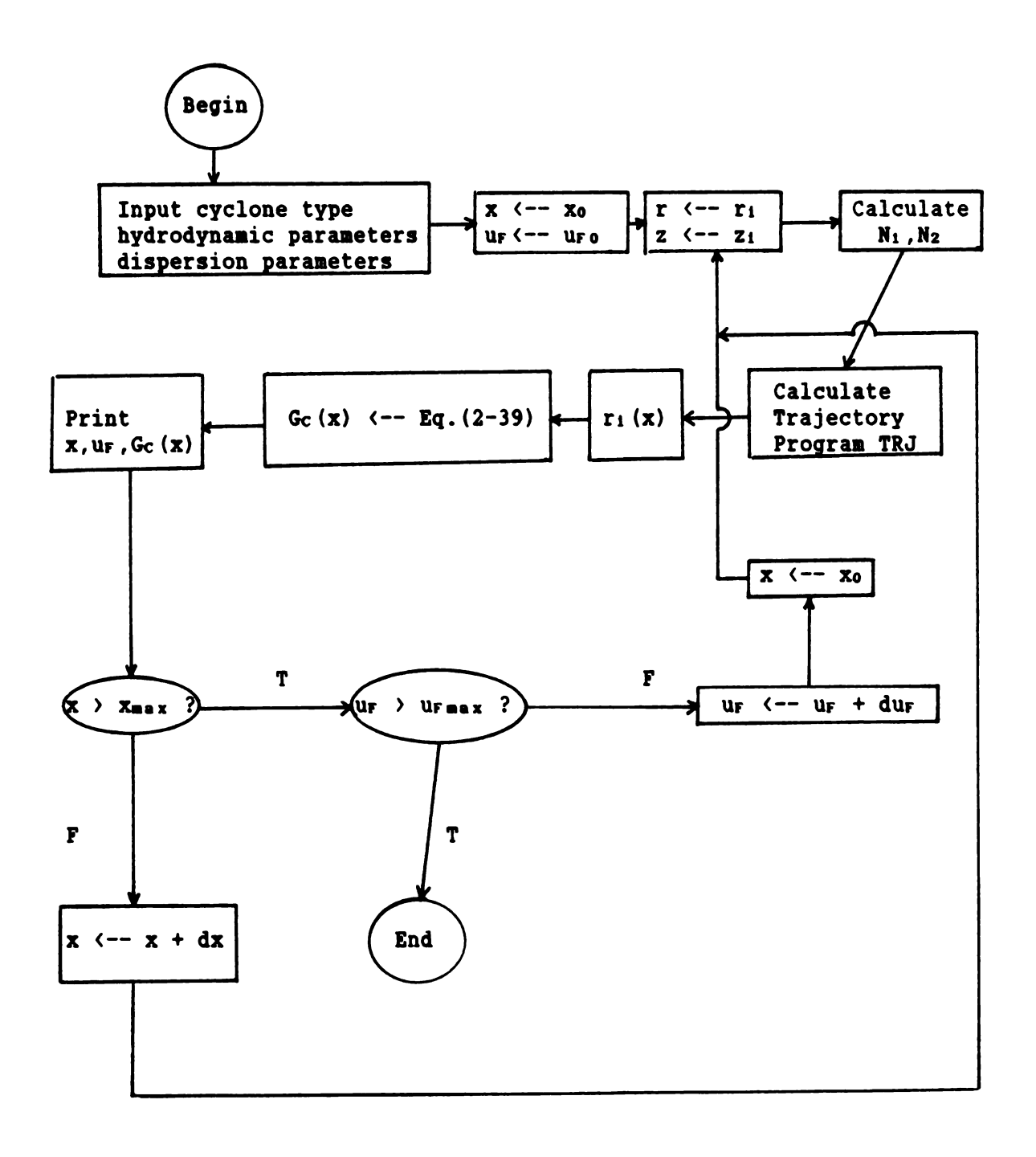
ITERC = 50

Z1 = 0.4545E-01 Z2 = 0.1099E+00 Z3 = 0.5439E+00 LA = 0.6445E-01 LB = 0.4340E+00 LU = 0.4561E+00

R	Z	RW	REP	WREP
1.0000E+00	0.4545E-01	1.0000E+00	0.2303E+00	0.1000E+01
0.7982E+00	0.7045E-01	0.8061E+00	0.3585E+00	0.1000E+01
0.5983E+00	0.9545E-01	0.6121E+00	0.6383E+00	0.1000E+01
0.4743E+00	0.1205E+00	0.4939E+00	0.1015E+01	0.1000E+01
0.4510E+00	0.1455E+00	0.4795E+00	0.1123E+01	0.1000E+01
0.4275E+00	0.1705E+00	0.4651E+00	0.1250E+01	0.1000E+01
0.4040E+00	0.1955E+00	0.4507E+00	0.1400E+01	0.1000E+01
0.3802E+00	0.2205E+00	0.4363E+00	0.1581E+01	0.1000E+01
0.3561E+00	0.2455E+00	0.4219E+00	0.1801E+01	0.1000E+01
0.3317E+00	0.2705E+00	0.4075E+00	0.2029E+01	0.9775E+00
0.3074E+00	0.2955E+00	0.3931E+00	0.2262E+01	0.9359E+00
0.2832E+00	0.3205E+00	0.3787E+00	0.2544E+01	0.8930E+00
0.2589E+00	0.3455E+00	0.3643E+00	0.2891E+01	0.8484E+00
0.2345E+00	0.3705E+00	0.3499E+00	0.3330E+01	0.8018E+00
0.2099E+00	0.3955E+00	0.3355E+00	0.3901E+01	0.7526E+00
0.1848E+00	0.4205E+00	0.3211E+00	0.4679E+01	0.6998E+00
0.1589E+00	0.4455E+00	0.3067E+00	0.5807E+01	0.6419E+00
0.1313E+00	0.4705E+00	0.2923E+00	0.7629E+01	0.5755E+00
0.1042E+00	0.4955E+00	0.2779E+00	0.7182E+01	0.5896E+00
0.8401E-01	0.5205E+00	0.2635E+00	0.6160E+01	0.6269E+00

## A.2. Centrifugal Grade Efficiency Calculation

## FLOW DIAGRAM FOR CENTRIFUGAL GRADE EFFICIENCY CALCULATION



## PROGRAM INPUT

FOR CYCLONE MODEL 3 LDC = 0.2200E+02LCDC = 0.1000E+01DDC =0.5000E+00 DODC = 0.7000E-01RF = 0.2500E + 00RU = 0.2500E+00ALPHAD = 0.1000E+02 DEGREESBETAD = 0.7500E+00 DEGREES X0 = 0.5000E-05M XMAX = 0.2000E-03 MDX0 = 0.1000E-04UF0 = 0.2000E+01M/S DUF = 0.3000E+01 M/SUFMAX = 0.1700E+02 M/SQCF = 0.1000E+01RHODC = 0.9750E+00 DENSITY RATIO NU = 0.1000E-05 KINEMATIC VISCOSITY,  $M^2/S$ RCH = 0.3800E-01 CYCLONE RADIUS, M M = 0.5000E+00RTH = 0.1250E+00 EN = 0.5000E+00INTLDC = 0.1000E+01DZ = -0.5000E-03

# TYPICAL PROGRAM OUTPUT (THIS OUTPUT WAS USED IN FIGURE 4.4)

Z1 = 0.4545E-01 Z2 = 0.1099E+00 Z3 = 0.5439E+00 LA = 0.6445E-01 LB = 0.4340E+00 LU = 0.4561E+00

Y (um)

# FOR UF = 0.2000E+01 m/sec

v (hm)	GC
0.5000E+01	0.1589E-02
0.1500E+02	0.1778E-01
0.2500E+02	0.6250E-01
0.3500E+02	0.1347E+00
0.4500E+02	0.2285E+00
0.5500E+02	0.3462E+00
0.6500E+02	0.4859E+00
0.7500E+02	0.6311E+00
0.8000E+02	0.7053E+00
0.8500E+02	0.7807E+00
0.9000E+02	0.8573E+00

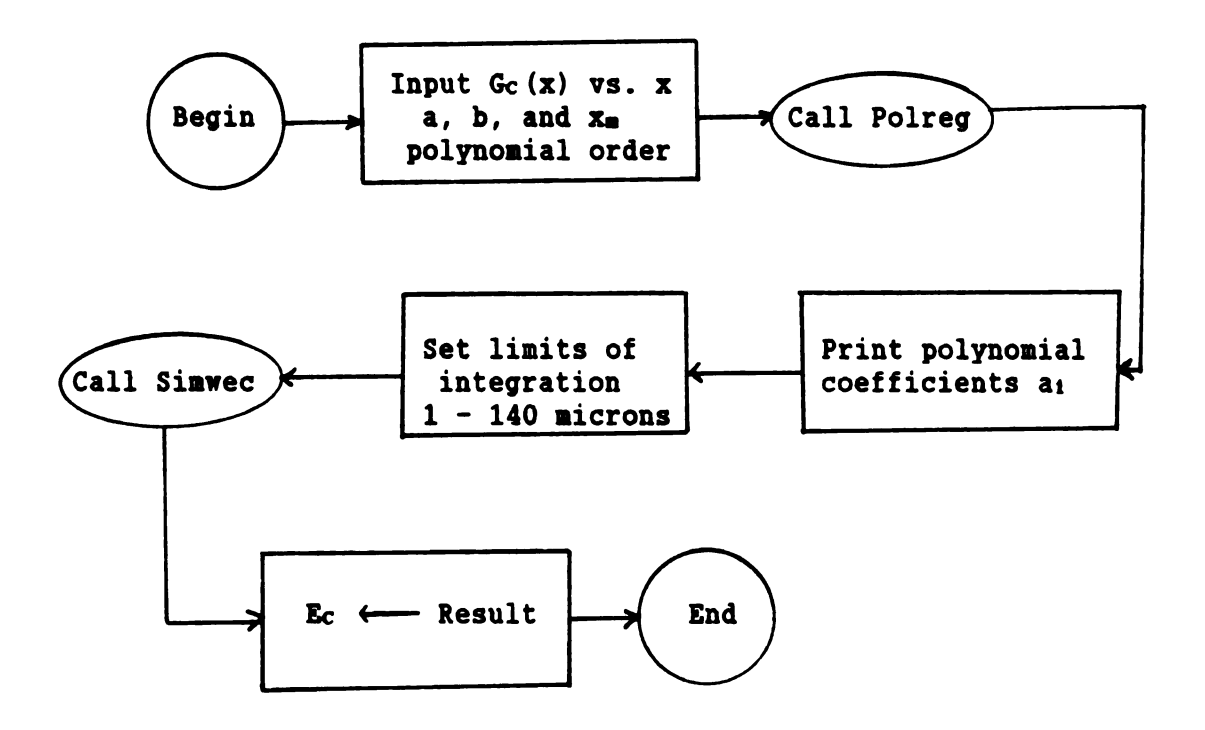
CC

X (μm)	GC
0.9250E+02	0.8960E+00
0.9500E+02	0.9350E+00
0.9750E+02	0.9735E+00
0.1000E+03	0.1000E+01
FOR UF = $0.5$	000E+01 m/sec
X (μm)	GC
0.5000E+01	0.4152E-02
0.1500E+02	0.5480E-01
0.2500E+02	0.1745E+00
0.3500E+02	0.3507E+00
0.4500E+02	0.5747E+00
0.5000E+02	0.6912E+00
0.5500E+02	0.8070E+00
0.6000E+02	0.9159E+00
0.6250E+02	0.9683 <b>E</b> +00
0.6500E+02	0.1000E+01
FOR UF = 0.8	000E+01 m/sec
X (µm)	GC
0.5000E+01	0.6945E-02
0.1500E+02	0.9594E-01
0.2500E+02	0.2841E+00
0.3500E+02	0.5579E+00
0.4000E+02	0.7020E+00
0.4500E+02	0.8331E+00
0.5000E+02	0.9568E+00
0.5250E+02	0.1000E+01
FOR UF = 0.1	100E+02 m/sec
X (µm)	GC
0.5000E+01	A GAGE#_AA
0.5000E+01 0.1500E+02	0.9986E-02 0.1362E+00
0.1500E+02 0.2500E+02	0.1362E+00 0.3957E+00
0.2500E+02 0.3500E+02	0.3957E+00
0.4000E+02	0.7209E+00 0.8613E+00
0.4250E+02	0.8613E+00
0.4250E+02 0.4500E+02	0.9308E+00 0.1000E+01
U.45UUETUZ	0.10000401

## A.2. Calculation of the Centrifugal Efficiency

The objective of this section is to evaluate the centrifugal efficiency integral given by Eq. (2-27). The program CENEFF.FOR does this by accomplishing a variety of tasks. In the main program, a data set containing the centrifugal grade efficiency as a function of particle size is read in from a data file CENEFF.DAT provided by the user. This data set is fit to a second order polynomial (the order can be varied) using a least squares minimization method (see p.124 Hornbeck, 1975) in subroutine POLREG. The polynomial coefficients are calculated using a Gauss-Jordan matrix inversion algorithm (see p.163 McCracken, 1967) in subroutine MATINY. The log-normal representation has been used as a model for the feed size density distribution in function subprograms EF and EFP. The parameters a, b, and xm for the log-normal distribution (see Eqs.(B-1) - (B-3)) are input in CENEFF.DAT. The centrifugal efficiency integral is evaluated using a composite Simpson's rule with end correction (see p.150 Hornbeck, 1975) in subroutine SIMWEC. The integral is evaluated at successively larger numbers of panels until the convergence criterion is met or the number of calculations exceeds a preset limits. The limits of the integration were set at 1 and 140 microns, the practical limits on the size range (see Figure B.4.2). This strategy is outlined in the following flow chart.

## FLOW DIAGRAM FOR PROGRAM CENEFF.FOR



```
C
      PROGRAM CENEFF
C
      UPDATED 10 MAY 1989
C
C ***********************
C
C
    THE FOLLOWING VARIABLE LIBRARY DEFINES SYMBOLS IN THE MAIN PROGRAM.
C
C
    J0
                INTEGER DENOTING CYCLONE TYPE
C
                1 = CONE ONLY
C
                2 = SINGLE-CONE (SC)
C
                3 = DOUBLE-CONE (CT)
C
    J1
                INTEGER DENOTING THE NUMBER OF DATA PAIRS INPUT TO THE
C
                MAIN PROGRAM
C
    J2
                INTEGER DENOTING ORDER OF POLYNOMIAL CHOSEN TO FIT
C
                Gc VS. X DATA
C
    J2P1
                J2 + 1
C
                J2P1 x 2
    J2P12
             =
C
                COUNTERS
    J3,J5
             =
C
    I1
                INTEGER DENOTING INITIAL # OF PANELS USED IN THE
C
                INTEGRATION SUBROUTINE SINVEC.
C
    X
                PARTICLE DIAMETER VECTOR
C
                LOWER LIMIT OF INTEGRATION ON PARTICLE SIZE
    XL
             =
C
    XUP
                UPPER LIMIT OF INTEGRATION ON PARTICLE SIZE
C
    A1,B1
                CONSTANTS OF LOG-NORMAL SIZE DENSITY DISTRIBUTION
            =
C
                MODE SIZE OF PARTICLE DISTRIBUTION X=
    XM
C
                SUCCESSIVE INTEGRATION CONVERGENCE CRITERION IN SIMVEC
    EPS
             =
C
    GC
                VECTOR HOLDING CENTRIFUGAL GRADE EFFICIENCIES
            =
C
    AI
                VECTOR HOLDING COEFFICIENTS FOR APPROXIMATING
C
                POLYNOMIAL, I.E. GC = A1 + A2*X + A3*X**2 + ...
C
    DUV1,
                DUMMY VECTORS/MATRICES ALLOWING VARIABLE DIMENSIONING
C
    DUM2-4
                IN SUBROUTINES AND FUNCTION SUBPROGRAMS
C
    EC
             = CENTRIFUGAL EFFICIENCY OF HYDROCYCLONE
C
C
C
  *********************
C
C
C
C
C
                       MAIN
                                 PROGRAM
C
C
 *****************
C
     PARAMETER(J1 = 5, J2 = 2, J2P1 = 3, J2P12 = 6)
     INTEGER 11, J3, J5, K3
     REAL*8 XL, XUP, A1, B1, XM, EPS, EC, GC(J1), X(J1), AI(J2P1)
     REAL*8 DUV1(J2P1), DUM2(J2P1, J2P1), DUM3(J2P1, J2P1), DUM4(J2P1, J2P12)
     COMMON/SIMW/I1, EPS
     COMMON/FCN/A1, B1, XM
     OPEN(2,FILE = 'CENEFF.DAT', STATUS = 'OLD')
     OPEN(4, FILE = 'CENEFF. PRN', STATUS = 'NEW')
     READ(2,*) (GC(J3), J3 = 1, J1)
     READ(2,*) (X(J3),J3 = 1,J1)
```

```
READ(2,*) A1,B1,XM,I1,EPS
C
      WRITE(*,'(6X,''GC'',15X,''X''/)')
      WRITE(*, '(1X, E12.4, 5X, E12.4)') (GC(J3), X(J3), J3 = 1, J1)
      WRITE(*,'(/1X,''INTERPOLATING POLYNOMIAL ORDER = '',12)')J2
C
      WRITE(*,'(1X,''FEED DISTRIBUTION PARAMETERS''/1X,''A1 '',E12.4/1X,
     1''B1 '',E12.4/1X,''XM '',E12.4/1X,''EPS '',E12.4/1X,''I1 '',I2/)')
     1A1,B1,XM,EPS,I1
C
C
      WRITE(4,'(6X,''GC'',15X,''X''/)')
      WRITE(4, '(1X, E12.4, 5X, E12.4)') (GC(J3), X(J3), J3 = 1, J1)
      WRITE (4, '(/1X, ''INTERPOLATING POLYNOMIAL ORDER = '', I2) ') J2
C
      WRITE (4, '(1X, ''FEED DISTRIBUTION PARAMETERS''/1X, ''A1 '', E12.4/1X,
     1''B1 '',E12.4/1X,''XM '',E12.4/1X,''EPS '',E12.4/1X,''I1 '',I2/)')
     1A1, B1, XM, EPS, I1
C
C ** CALL SUBROUTINE POLREG TO GENERATE NTH POLYNOMIAL COEFFICIENTS AI **
C
C
      J5 = 2*(J2+1)
      CALL POLREG (J1, J2P1, J5, GC, X, DUV1, DUM2, DUM3, DUM4, AI)
C
      WRITE(*,'(/1X,''POLYNOMIAL COEFFICIENTS = '')')
      WRITE (4, '(/1x, ''POLYNOMIAL COEFFICIENTS = '')')
      DO 15 K3 = 1.J2P1
      WRITE(4,'(1X,E12.4)')AI(K3)
15
      WRITE(*,'(1X,E12.4)')AI(K3)
C
C
C
C *** SET LOWER AND UPPER BOUNDS OF INTEGRATION FROM 1 --> 140 um ******
C
      XL = 1.D0
      XUP = 140.D0
C ******* CALL SUBROUTINE SIMVEC TO CALCULATE Ec ***********
C
C
       CALL SIMWEC(XL, XUP, J2P1, AI, EC)
       WRITE(*,'(//1X,''EC = '',E12.4)')EC
       WRITE(4,'(//1X,''EC = '',E12.4)')EC
C
C
30
      END
C
C *********** E N D O F M A I N P R O G R A M *******
```

```
C *** S U B R O U T I N E S / F U N C T I O N S U B P R O G R A M S **
C
 *** POLYNOMIAL REGRESSION SUBROUTINE ***
C
C
     THE LOGIC FOR THIS POLYNOMIAL REGRESSION IS FOUND IN CH7. HORNBECK
C
C
     VARIABLE LIBRARY
C
C
     K1, K2, K22 = HOLDERS FOR J1, J2, J2P1 FROM MAIN PROGRAM
C
     ΥI
               = VECTOR HOLDING ABCISSA VALUES IN REGRESSION
C
     XI
               = VECTOR HOLDING ORDINATE VALUES IN REGRESSION
C
     AIP
               = VECTOR HOLDING COEFFICIENTS FOR REGRESSION
C
                  POLYNOMIAL
C
     SUMV
               = VECTOR DENOTING SUMMATION OF YI
C
     SMCM
               = COEFFICIENT MATRIX
C
     SMCMIN
              = INVERSE MATRIX OF SMCM
C
     BMINV
               = MANIPULATION MATRIX IN MATINV
C
     K3-K5
              = INTEGER COUNTERS
C
     E, EMAX
              = EXPONENTS IN POLYNOMIAL SERIES
C
C
     SUBROUTINE POLREG(K1, K2, K22, Y1, X1, SUMV, SMCM, SMCMIN, BMINV, AIP)
     INTEGER K1, K2, K22, K3, K4, K5, EMAX, E
     REAL*8 YI (K1), XI (K1), AIP (K2), SUMV (K2), SMCM (K2, K2)
     REAL*8 SMCMIN(K2, K2), BMINV(K2, K22)
C
C
C
   C
     DO 101 K3 = 1, K2
101
      SUMV(K3) = 0.D0
       DO 102 K3 = 1, K2
       DO 102 \text{ K4} = 1, \text{K1}
102
         SUMV(K3) = SUMV(K3) + (XI(K4)**(K3-1))*YI(K4)
    C
     DO 105 K3 = 1.K2
      DO 105 \text{ K4} = 1, \text{K2}
105
       SMCM(K3, K4) = 0.D0
       EMAX = 2*(K2-1)
        DO 120 K3 = K2,1,-1
         E = EMAX
          DO 115 K4 = K2,1,-1
           DO 110 K5 = 1, K1
110
            SMCM(K3,K4) = SMCM(K3,K4) + XI(K5)**E
115
             E = E - 1
120
              EMAX = EMAX - 1
C
  *************
С
```

```
CALL HATINV (SHCH, SHCHIN, K2, K22, BMINV)
C
C
  ***** MULTIPLY SUMV BY SMCMIN TO GIVE POLYNOMIAL COEFFICIENTS ******
C
      DO 125 K3 = 1, K2
125
      AIP(K3) = 0.D0
      DO 130 K3 = 1, K2
       DO 130 K4 = 1, K2
130
        AIP(K3) = AIP(K3) + SMCMIN(K3, K4) *SUMV(K4)
C
C
      END
C
C
C
 ****** END OF SUBROUTINE POLREG ********
C
C
C
C ***** M A T R I X
                        INVERSION SUBROUTINE *******
C
C
     MATRIX INVERSION SUBROUTINE TAKEN FROM P.163 MCCRACKEN, 1967
C
      THIS SUBROUTINE RECEIVES COEFFICIENT MATRIX MATRIX A1 AND RETURNS
C
      ITS INVERSE A2, HAVING PERFORMED GAUSS-JORDAN ELIMINATION.
C
C
      SUBROUTINE MATINV (A1, A2, L1, L2, B)
      INTEGER L1, L2, L3, L4, L5, L6, L7, L7P1, L8, L7M1
      REAL*8 A1 (L1, L1), A2 (L1, L1), B (L1, L2), TEMP
C
      DO 201 L3 = 1,L1
      DO 201 L4 = 1, L1
201
        B(L3,L4) = A1(L3,L4)
      L5 = L1 + 1
      L6 = L2
      DO 202 L3 = 1, L1
      DO 202 L4 = L5, L6
202
        B(L3,L4) = 0.D0
      DO 203 L3 = 1, L1
      L4 = L3 + L1
203
        B(L3,L4) = 1.D0
      DO 250 L7 = 1,L1
      L7P1 = L7 + 1
        IF(L7.EQ.L1)GOTO 240
        L8 = L7
          DO 230 L3 = L7P1, L1
230
           IF(ABS(B(L3,L7)).GT.ABS(B(L8,L7)))L8 = L3
          IF (L8.EQ.L7) GOTO 240
          DO 231 L4 = L7, L6
           TEMP = B(L7, L4)
            B(L7,L4) = B(L8,L4)
231
             B(L8,L4) = TEMP
240
          DO 241 L4 = L7P1, L6
```

```
241
          B(L7,L4) = B(L7,L4)/B(L7,L7)
         IF (L7.EQ.1) GOTO 247
         L7M1 = L7 - 1
         DO 245 L3 = 1.L7M1
          DO 245 L4 = L7P1, L6
245
           B(L3,L4) = B(L3,L4) - B(L3,L7)*B(L7,L4)
         IF (L7.E0.L1) GOTO 270
247
         DO 250 L3 = L7P1.L1
          DO 250 L4 = L7P1.L6
250
           B(L3,L4) = B(L3,L4) - B(L3,L7)*B(L7,L4)
270
         DO 271 L3 = 1,L1
          DO 271 L4 = 1, L1
           L7 = L4 + L1
271
            A2(L3,L4) = B(L3,L7)
     END
C
C
C ****** E N D O F S U B R O U T I N E M A T I N V *********
C
C
C
C
   *****
                       INTEGRATING SUBROUTINE ****************
C
C
     SUBROUTINE SIMVEC (AY, BY, IO, AI, ANSWER)
C
C
C
     VARIABLE LIBRARY - SUBROUTINE SIMVEC
C
C
     10
               = DUMMY VARIABLE TO ALLOW VARIABLE ARRAY FOR AI VECTOR
C
     I1
               = SAME AS IN MAIN PROGRAM
C
     12
               = COUNTER FOR # OF ITERATIONS ON INTEGRAL VALUE
C
               = LOOP COUNTER
     13
C
     14
               = DUMMY VARIABLE FOR # OF MESH POINTS = # PANELS + 1
C
     AY, BY
               = DUMMY VARIABLES FOR INTEGRATION LIMITS A, B
C
     ANSWER
               = RESULT OF INTEGRATION
C
     F
               = FUNCTION EVALUATION VALUE
C
     EF
               = FUNCTION SUBPROGRAM FOR FUNCTION BEING INTEGRATED
C
     EFP
               = FUNCTION SUBPROGRAM FOR 1ST DERIVATIVE OF EF
C
     TOT
               = VECTOR CONTAINING INTEGRAL VALUES
C
               = INTERVAL LENGTH
     H
C
     ZE
               INDEPENDENT VARIABLE OF INTEGRATION
C
     PART1
               = ENDPOINT FUNCTION EVALUATIONS SUMMATION
C
     PART2
               = ODD MESH POINT FUNCTION VALUE SUMMATION
C
     PART3
               = EVEN MESH POINT FUNCTION VALUE SUMMATION
C
     PART4
               = ENDPOINT DERIVATIVE VALUE SUMMATION
C
     EPS
               = INTEGRAL CONVERGENCE CRITERION
C
   *********
C
     INTEGER 11,12,13,10
     REAL*8 AY, BY, ANSWER, F (500), TOT (100), EF, EFP, H, ZE, EPS, AI (10)
     COMMON/SIMW/I1, EPS
```

```
I2 = 0
    I4 = I1
 *** CALCULATE INTERVAL LENGTH, INITIALIZE INDEPENDENT VARIABLE ****
500
   H = (BY - AY)/(I4-1)
    ZE = AY
C
 ****** CALCULATE FUNCTION VALUES AT INNER MESH POINTS *******
    DO 510 I3 = 2.14-1
    ZE = ZE + H
510
    F(I3) = EF(ZE,AI,I0)
  ***********
C
C
  ****** CALCULATE FUNCTION VALUES AT INTERVAL ENDPOINTS ******
C
    PART1 = 5.D-1*(EF(AY,AI,IO) + EF(BY,AI,IO))
C
C
  ******************
C
   ****** CALCULATE ODD POINT FUNCTION VALUE SUMMATION *******
C
    PART2 = 0.D0
    DO 515 I3 = 3, I4-2, 2
515
    PART2 = PART2 + F(I3)
  ***********
C
  ****** CALCULATE EVEN POINT FUNCTION VALUE SUMMATION *******
C
    PART3 = 0.D0
    DO 520 I3 = 2.14-1.2
520
    PART3 = PART3 + F(I3)
C ****** CALCULATE DERIVATIVE VALUES AT INTERVAL ENDPOINTS *******
    PART4 = H*(EFP(AY,AI,IO) - EFP(BY,AI,IO))
    I2 = I2 + 1
C
C
C
C
  C
    TOT(12) = H*(14.D0*(PART1 + PART2) + 16.D0*PART3 + PART4)/15.D0
C
  C
    I4 = I4 + 10
C
```

```
*****************
     IF (I2.EQ.1) GOTO 500
C
C
  ******************
C
C
  ********** CHECK CONVERGENCE CRITERION **************
C
     IF (DABS (TOT (I2) - TOT (I2-1)).LE.EPS) GOTO 530
C
     IF (12.GT.44) THEN
      WRITE(*,'(1X,''REACHED MAX # OF PANELS IN SIMVEC''/1X,''NEED TO I
    INCREASE DIMENSION OF TOT AND F ACCORDINGLY''/1X,''OR RELAX CONVERG
    1ENCE CRITERION EPS'')')
      GOTO 530
       ENDIF
C
     GOTO 500
530
     ANSWER = TOT(12)
     15 = 14
     END
C ****** E N D O F S U B R O U T I N E S I M W E C ********
C
C
C ******* F U N C T I O N
                               S U B P R O G R A M S ***********
C
C
     THESE SUBPROGRAMS PERFORM FUNCTION EVALUATIONS FOR SIMVEC.
C
     CALCULATING GC (x) ff (x) MULTIPLICATIONS USING THE POLYNOMIAL
C
     COEFFICIENTS AI AND THE LOG-NORMAL SIZE DENSITY PARAMETERS A1.B1.
C
     AND XM
C
C
     VARIABLE LIBRARY
C
C
     GEC
           = Gc
C
     GECP
           = DERIVATIVE OF Gc
C
     Y1-Y4 = HOLDERS FOR f_F(x) FUNCTION
C
           = FUNCTION VALUE OF GcfF
     EF
C
     EFP
           = DERIVATIVE OF EF
C
     FUNCTION EF(X1, AYI, P1)
     INTEGER P1, P2
     REAL*8 AYI(P1), X1, A1, B1, XM, GEC, EF, Y1, Y2, Y3, Y4
     COMMON/FCN/ A1.B1.XM
C
     GEC = 0.D0
     Y1 = DLOG(X1/XM)
     Y2 = Y1 **2
     Y3 = -B1*Y2
     Y4 = DEXP(Y3)
     DO 600 P2 = 1, P1
600
      GEC = GEC + AYI(P2)*(X1**(P2-1))
     IF (GEC.GT.1.DO) THEN
      GEC = 1.D0
```

```
ENDIF
C
     IF (GEC.LT.O.DO) THEN
      GEC = 0.D0
       ENDIF
C
     EF = A1*Y4*GEC
     END
C
C ***** END OF FUNCTION SUBPROGRAM EF ****
C
C
     FUNCTION EFP(X1,AYI,P1)
     INTEGER P1, P2
     REAL*8 AYI(P1), X1, A1, B1, LMAX, XM, GEC, GECP, EFP, Y1, Y2, Y3, Y4
     COMMON/FCN/ A1, B1, XM
C
C
     GEC = 0.D0
     GECP = 0.D0
     Y1 = DLOG(X1/XM)
     Y2 = Y1 \times 2
     Y3 = -B1*Y2
     Y4 = DEXP(Y3)
     DO 700 P2 = 1,P1
700
      GEC = GEC + AYI(P2) * (X1 ** (P2-1))
       IF (GEC.LT.O.DO) THEN
        GEC = 0.D0
         ENDIF
        IF (GEC.GT.1.DO) THEN
         GEC = 1.D0
          ENDIF
     DO 710 P2 = 1,P1-1
710
      GECP = GECP + P2*AYI(P2+1)*(X1**(P2-1))
C
     EFP = A1*Y4*GECP - GEC*(2.D0*A1*B1*Y1*Y4)
     END
C **** E N D
             OF FUNCTION SUBPROGRAM EFP ****
C ****** E N D O F P R O G R A M C E N E F F **********
```

# PROGRAM INPUT

GC	X (MICRONS)
0.9683E+00	0.6250E+02
0.9159E+00	0.6000E+02
0.6912E+00 0.3507E+00	0.5000E+02 0.3500E+02
0.1745E+00	0.2500E+02
0.1000E-03	0.1000 <b>E</b> -03

# INTERPOLATING POLYNOMIAL ORDER = 2

# FEED SIZE DENSITY DISTRIBUTION PARAMETERS

A1 = 0.2360E-01 (MICRON\*\*-1)

B1 = 0.3700E+01

XM = 0.4300E+02 (MICRONS)

EPS = 0.1000E-03

I1 = 51

# PROGRAM OUTPUT

# POLYNOMIAL COEFFICIENTS

A0 = -0.6531E-02A1 = 0.2961E-02

A2 = 0.2068E-03

EC = 0.6526E+00

# APPENDIX B

EXPERIMENTAL METHODS AND TABULATED DATA

#### APPENDIX B

#### EXPERIMENTAL METHODS AND TABULATED DATA

# B.1 Isokinetic Sampling Technique

Svarovsky (see p.26, 1977) has given two rules for sampling:

- (1) Sampling should be made from a moving stream.
- (2) A sample of the whole of the stream should be taken for many short periods rather than part of the stream for the whole of the time.

The second option was initially used to gather samples which needed to be subdivided into smaller portions for analysis. There were two difficulties with this method. First, repeated removal of the underflow line from below the liquid-air interface caused intense foaming in the feed tank due to the entrainment of air by the liquid jet. This foaming kept dispersed phase particles at the liquid-air interface, changing the feed composition. Also, entrained microbubbles formed an air core in the hydrocyclone, visibly changing separator hydrodynamics. Secondly, subdivision of this sample into representative portions suitable for gravimetric analysis was not possible. There was a tendency for particle stratification (float-out) and particle segregation by centrifugal action due to the swirl induced by stirring prior to subdivision.

To continuously withdraw a portion of a fluid from a moving stream, care must be taken to sample in a representative manner. In general,

when a bluff body is placed in the flow, very fine particles tend to follow fluid streamlines, but large particles deviate from the streamlines due to inertial effects. To sample from a moving stream without appreciably disturbing streamlines, a nozzle facing opposite to the direction of flow is used to remove a portion of the stream. This type of sampling is usually referred to as isokinetic sampling. A schematic of the design for the isokinetic sampling assemblies used in the flow loop (see Figure 5.2) is shown in Figure B.1. The assemblies were based on the design described by Colman (see Figure 4 Colman, 1981). A 5 mm ID probe was centered in a 19 mm ID copper tube that was part of the feed underflow line. The probe left the copper tube at about a 45° angle and was connected to 9.5 mm ID needle valve assembly. The needle valve was used to adjust the sampling rate. Pressure taps 1.6 mm ID were made in the probe wall and the tube wall. These were connected across a mercury manometer to measure the static pressure drop between the tube and probe walls. The entire assembly was located at least 10 tube diameters from bends or constrictions in the underflow or feed lines to help maintain a homogeneous particle distribution in the stream.

The principle of operation (see p.142 Fuchs, 1964 or Dennis et al., 1957 for more details) is to maintain equal static pressures at the probe and tube wall, resulting in a minimum deflection of fluid streamlines. This is accomplished by varying sampling valve resistance. The two types of flow conditions that give erroneous concentration measurements result from deviations in streamline flow at the mouth of the probe. When the fluid velocity in the sampling tube is too high (indicated on the manometer as an unbalanced pressure reading in favor of higher pressure

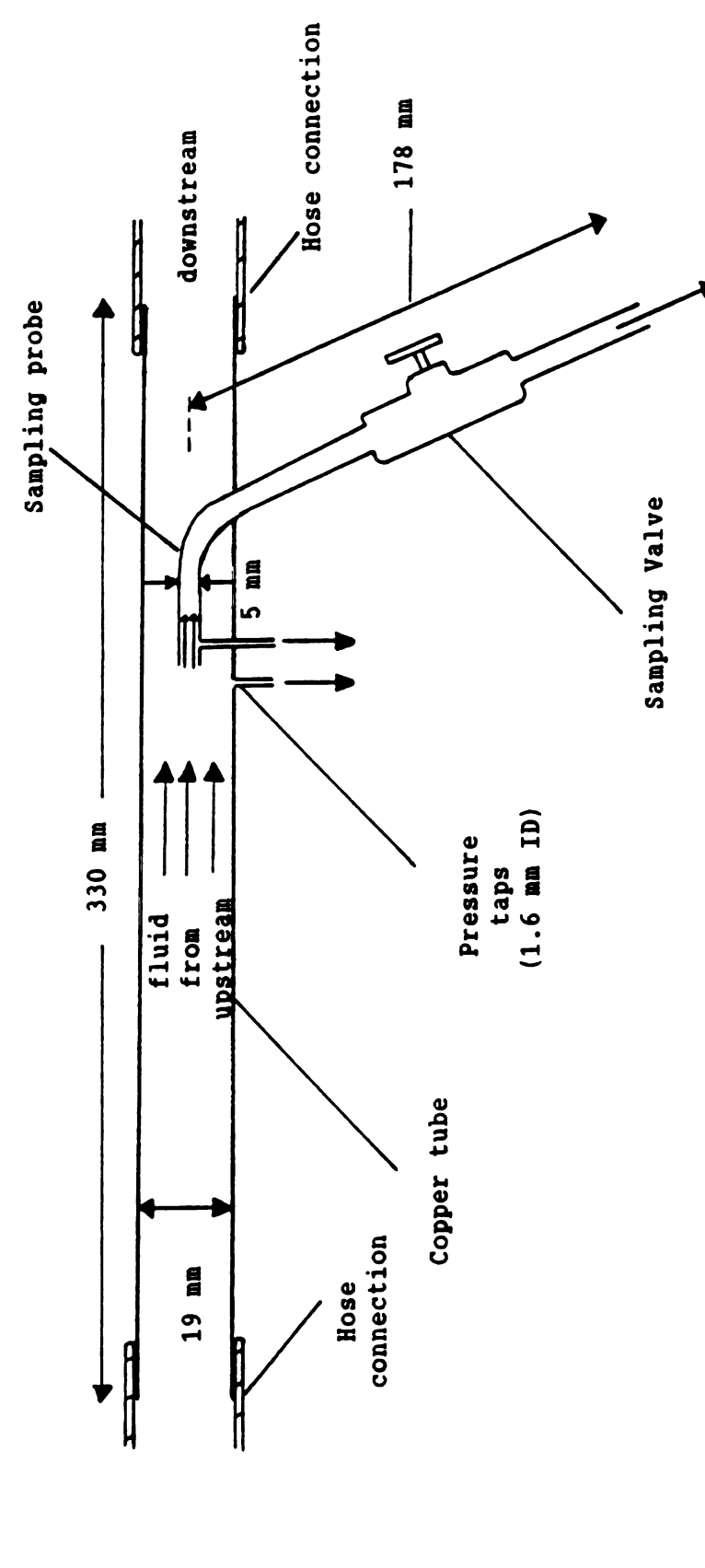


Figure B.1. Isokinetic sampling assembly.

at the copper tube wall), light dispersed particles from streamlines directed just outside the probe enter the probe due to centripetal effects. The concentration measured is too high. When the fluid velocity in the probe is too low, particles from streamlines directed just inside the probe walls will not enter the probe due to centripetal effects and the concentration measured is too low. A balanced manometer reading gives the correct concentration, although Dennis et al. [1957] have argued in favor of slightly higher probe velocities to counter the effect of friction losses inside the smaller diameter probe.

# B.2. Calibration of Rotameters

To calibrate the rotameters measuring the feed and underflow streams, a large calibrated bucket (20 liters ± 5%) and a stopwatch were used. Samples of 20 liters were taken for flow rates greater than 57 liters/min and samples of 10 liters were taken for flow rates less than 57 liters/min. The resulting volumetric flow rate was plotted vs. indicated flow rate and a least squares algorithm was used to fit the resulting calibration curve.

With a reaction time of about 0.5 seconds for bucket removal, the resulting flow rate measurement errors are bounded above by 9% and below by 7.5%. The overflow volumetric rate was measured by diverting the whole stream into a calibrated beaker (2 liters  $\pm$  5%). With an estimated reaction time of 0.25 seconds due to beaker removal, the error in measured flow rate was about  $\pm$  6%. The error bounds on the feed stream and the overflow stream flow rates combine to give a bound on the ratio of these two flow rates (So) of  $\pm$  1.5%.

### B.3. Filtration Methodology

To analyze the dispersed phase mass fractions in the feed and underflow streams, a gravimetric method based on filtration was used. The feed and underflow stream samples ranged from 500 ml to 1400 ml. These samples were collected in suitable beakers and weighed to  $\pm$  0.2 g. The sample was then analyzed after preparation of the filter papers. The following sequence outlines the steps taken in this process.

- (1) Handle filter papers with sterilized gloves or tongs at all times.
- (2) Rinse clean filters in deionized or distilled water to remove dust, loose paper fragments, etc..
- (3) Fold wet filter papers in quarters. 15 cm diameter papers will hold about 50 ml when folded in the funnel shape. Place folded filters into small beaker for oven drying.
- (4) Dry filters at 115°C for 3 hours. This temperature was chosen so as not to melt the HDPE crystals (melting point ≈ 125°C).
- (5) Mark dried filters lightly with a pencil.
- (6) Transfer filters to a dessicator for cooling for about 4 hrs.
- (7) Just prior to filtration, weigh filter on a precision balance (accurate to four significant digits). Allow the scale reading to stabilize in the fourth digit and make a five count before reading the mass display. This procedure was used on all weighings to consistently account for moisture adsorption during the weighing process.
- (8) Wet each filter with deionized or distilled water before inserting into the funnel. The edge of the filter and funnel lip should be flush and the filter cone should be seated into the funnel apex. Clamps were used to seal short circuit paths for air during the filtering.
- (9) Filter at appropriate suction, taking care not to burst filters with excessive vacuum. Follow filtration with 200 ml of deionized or distilled water to rinse solids.
- (10) Remove filter and dry in oven at 115°C for three hours.
- (11) Dessicate for four hours.
- (12) Remove filters from dessicator and weigh as in step (7).

### B.4. Characterization of the Dispersion

In order to accurately characterize the HDPE powder used in the experimental work, the mass density and size density distribution were determined.

# B.4.1. Mass density determination

The mass density of the HDPE powder was calculated gravimetrically using a pycnometer. The volume of the pycnometer was calibrated using distilled water. The mass of the water required to fill the vessel was converted to volume using the density of water given by the CRC Handbook of Chemistry and Physics (see p.F-4, 1988). Using this calculated volume, the density of normal-butanol was confirmed to within 0.5% of the value given by Kreith (see p.657, 1986) giving confidence to the procedure. The density of the HDPE powder was determined in the following manner. With a known mass of HDPE in the pycnometer, normalbutanol ( $\approx 0.8$  g/cm<sup>3</sup>) was slowly added. The heavier HDPE remained on the bottom of the vessel. After the pyknometer was filled and capped, excess fluid was removed from the vessel surface. The mass of the vessel and contents was measured over a 15 - 20 minute period. As the temperature of the fluid rose, normal-butanol exited around the loose fitting cap and evaporated. At three to four points in the experiment, the mass and the temperature of the pycnometer and contents were recorded. Using normal-butanol densities reported in the International Critical Tables (see p.33, Volume 3, 1926), the volume of the HDPE powder was calculated by difference. The density of the powder could then be calculated from the measured mass of powder. Three separate determinations of the powder mass density yielded a mean value of 0.976 ±.004 g/cm<sup>3</sup>, comparing well with the value reported by the Dow Chemical Company of  $0.96 \text{ g/cm}^3$ .

### B.4.2. Size density determination

Svarovsky [1977] has summarized commonly used representations of cumulative size distributions and also the different measures of particle size that can be used. The equivalent diameter of a sphere which has the same volume as a given particle will be used and denoted by the symbol x.

The log-normal distribution is a common representation for quantities which are necessarily non-negative, such as particle size. As its name implies, the log-normal distribution is a distribution in which the logarithm of the variate is normally distributed. The equation expressing the size density distribution using this representation was shown by Svarovsky (see p.21,1977) to be

$$f(x) = a \exp(-b\ln^2(x/x_n)) , \qquad (B-1)$$

where

$$a = [\exp(-1/4b)(b/\pi)^{1/2}]/x_m , \qquad (B-2)$$

and

$$b = (2\ln^2 \sigma_g)^{-1} . (B-3)$$

The variables  $x_m$  and  $\sigma_g$  represent the mode size and the geometric standard deviation of the cumulative size distribution. The mode size  $x_m$  is the particle size at which the cumulative size distribution has the steepest slope and the geometric standard deviation is a measure of the spread of the density distribution around the mode size  $x_m$ .

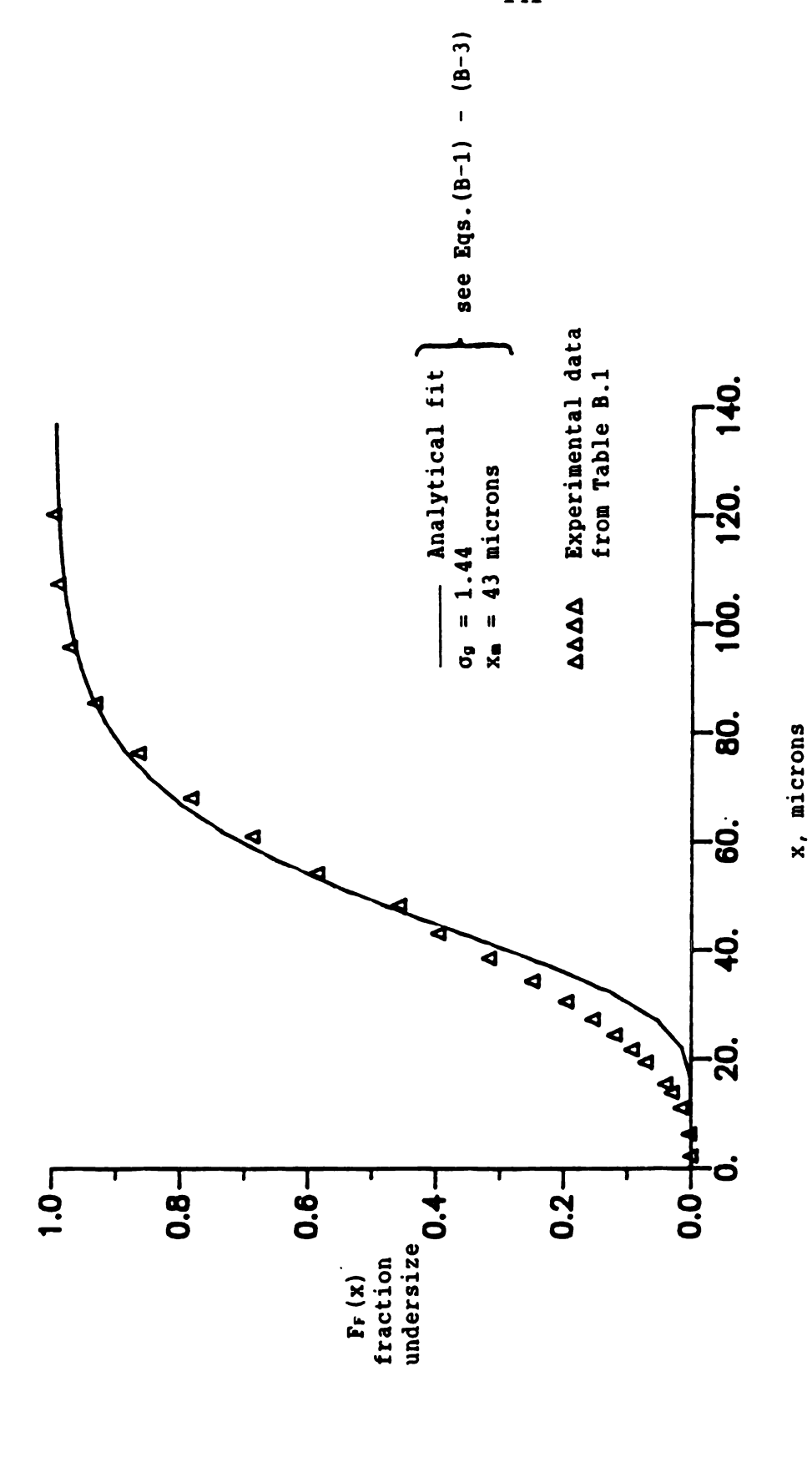
Samples of the HDPE powder were analyzed by personnel from Particle Data Institute using the Elzone 180 series particle size analyzer. The data for the cumulative volume fraction oversize as a function of equivalent spherical diameter is given in Table B.1. Using the method

described by Svarovsky (see p.21, 1977), the parameters  $x_m$  and  $\sigma_g$  can be estimated from the cumulative size distribution in Table B.1.

Table B.1. Diameter size vs. percentage oversize

Size (microns)	% Oversize	Size (microns)	68.30 60.30 54.20 41.30 31.20 21.60	
2.2	100.00	38.5	68.30	
6.2	99.76	43.1	60.30	
11.0	98.45	48.3	54.20	
13.8	97.03	54.2	41.30	
15.4	96.00	61.0	31.20	
19.4	92.90	68.0	21.60	
21.7	90.70	76.3	13.40	
24.4	88.00	85.5	6.60	
27.3	84.60	95.8	2.60	
30.6	80.40	107.4	0.70	
34.3	74.90	120.3	0.04	

With these two parameters, the size density distribution (Eq.(B-1)) is then fully described. To test how well this fitted size density distribution represents the data given in Table B.1, Eq.(B-1) can be integrated over the particle size range to give the cumulative size distribution (see Eq.(2-4)). The curves for the experimental and calculated cumulative size distribution can be compared. In this manner, values of  $x_m$  and  $x_m$  can be chosen for which the calculated cumulative distribution is a better fit to the experimental data. Figure B.2 shows the result of this trial and error procedure, which resulted in the following set of parameters for Eq.(B-1):  $x_m = 43$  microns and  $x_m = 1.44$ . The calculated cumulative size distribution fits the data of Table B.1 adequately, as shown in Figure B.2. The resulting size density distribution is shown in Figure B.3 and is very similar to the size density distribution of the polypropylene powder used by Colman (see Figure 5 Colman, 1981).



Comparison of analytically fitted cumulative size distribution to experimental data for HDPE powder. Figure B.2.

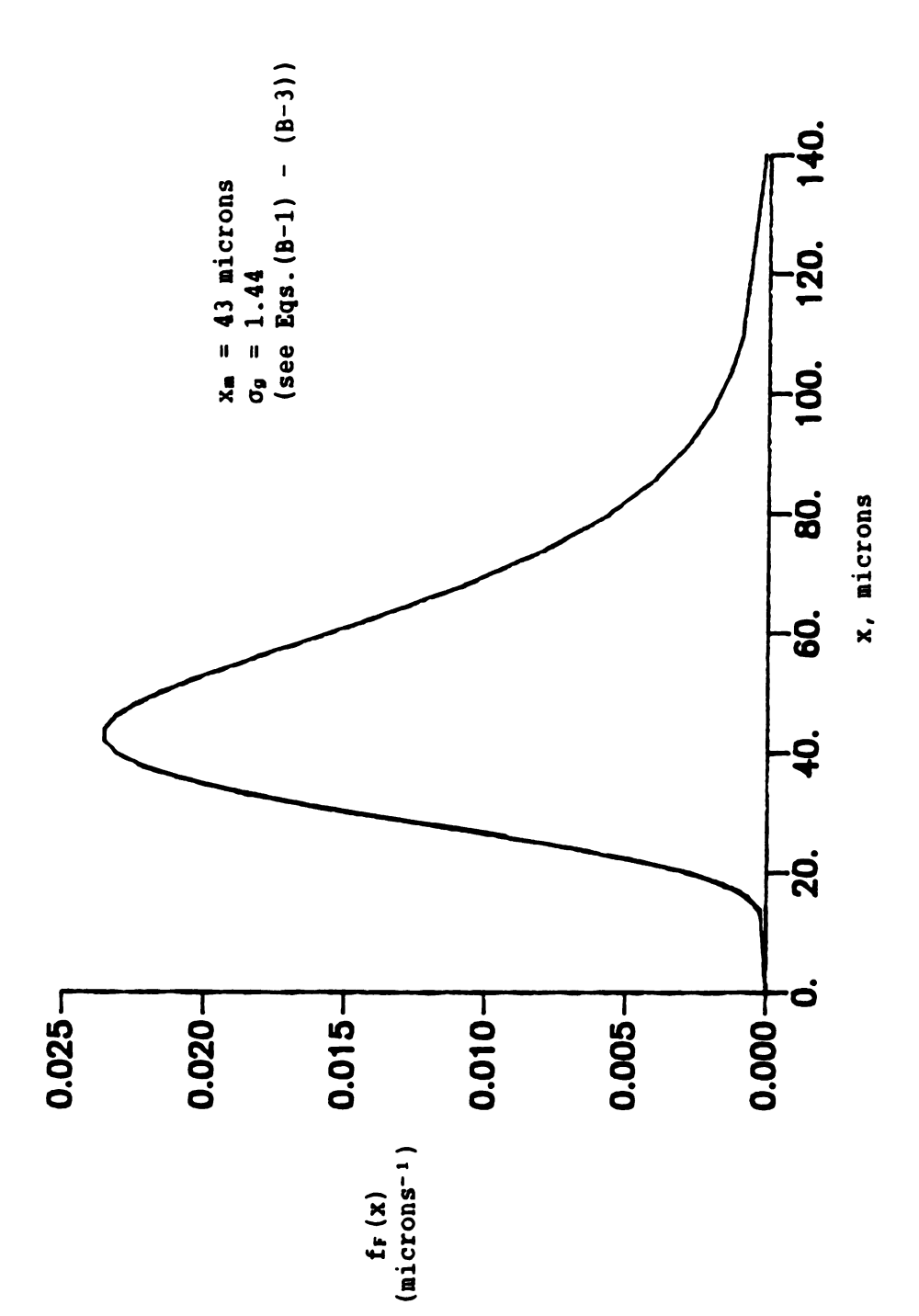


Figure B.3. Size density distribution for HDPE powder.

# B.5. Pressure Drop - Flow Rate Data

Table B.2 contains the pressure drop - flow rate data observed at the minimum overflow ratios given in Figure 5.3.

Table B.2. Pressure drop - flow rate data

Colman-Thew (	CT)	des	ign
---------------	-----	-----	-----

(So)min (psi)	P <sub>F</sub> -P <sub>0</sub>	P <sub>F</sub> -P <sub>U</sub>	Сро	C <sub>P u</sub>	Ref
0.14	2±2	2±2			34674
0.10	14±2	9±2	14.5	9.3	69347
0.12	31±2	16±2	18.6	9.6	90913
0.10	50±2	23±2	20.0	9.2	116632
S	ingle-Co	one (SC)	() desig	ın	
0.09	7±2	4±2	34.7	19.8	31714
0.09	23±2	14±2	27.3	16.6	64696
0.08	47±2	27±2	31.2	17.9	86684
	(psi) 0.14 0.10 0.12 0.10 S 0.09 0.09	(psi)  0.14	(psi)  0.14	(psi)  0.14	(psi)  0.14

T ≈ 20°c

See Figure 5.2 for location of pressure gauges.

# B.6. Underflow Purity Data

Tables B.3 and B.4 contain underflow purity data for the SCI- and CT-cyclones, respectively.

In both experiments for the SCI-cyclone (see Table B.3), the underflow purity was calculated using an average feed composition. In Experiment #1, the feed composition is equal to the average of the feed compositions of samples 1, 4, and 8. The underflow purity for the SCI-cyclone for the feed flow rate 11 gpm (sample 2) is then (see Eq.(1-1))

$$E' = 1 - (566 \text{ wppm})/(856 \text{ wppm}) = 0.339.$$

In experiment #4 for the CT-cyclone (see Table B.4), the underflow purity is calculated in the same manner as the SCI-cyclone, while in experiment #3, the dispersed phase feed and underflow compositions are measured at each flow rate and used to calculate E'. For example, at a feed flow rate of 26.5 gpm (see Experiment #3), the underflow purity is calculated as

E' = 1 - (364 wppm)/(866 wppm) = 0.583.

Table B.3. Underflow purity data for SCI-cyclone.

Experiment #1

Sample*	Qf (gpm)	So	$P_F - P_U$ (± 2 psi)	Sample Mass (g)	Solids Mass (g)	YF OT YU
1/ <b>F</b>	11.0	0.09	7	460.8	0.3999	856
2/U	11.0	0.09	7	570.9	0.3299	566
3/U	17.3	0.09	17	850.0	0.4261	489
4/F	23.4	0.09	30	1051.5	0.8570	803
5/ช	23.4	0.09	30	1091.5	0.5371	480
6/U	16.6	0.09	16	836.2	0.4152	485
7/ט	23.7	0.09		1248.5	0.6124	479
8/F	23.7	0.09	32	605.3	0.5104	831
9/U	11.0	0.09	8	591.0	0.3073	508
			T = 21°C,	(YF)AVG = 83	30 wppm	
			Ex	periment #2		
1/ <b>F</b>	13.0	0.09	10	602.9	0.5772	945
2/11	13.0	0 09		519 A	0.3229	610

1/F	13.0	0.09	10	602.9	0.5772	945
2/U	13.0	0.09	9	519.4	0.3229	610
3/U	13.0	0.09	9	531.9	0.3383	625
4/U	13.0	0.09	9	548.0	0.3504	627
5/F	22.5	0.10	28	1209.5	1.1525	941
6/U	22.5	0.10	28	1124.7	0.6233	542
7/U	13.3	0.10	11	563.4	0.3386	589
8/U	13.2	0.10	10	601.8	0.3767	614

 $T = 21^{\circ}C$ ,  $(y_F)_{AVG} = 943 \text{ wppm}$ 

Concentrations corrected for 12 wppm dissolved/stray solids content of tap water.

<sup>\*</sup>F = Feed, U = Underflow

Table B.4. Underflow purity data for CT-cyclone.

# Experiment #3

Sample*	Qf (gpm)	So	P <sub>F</sub> -P <sub>U</sub> (± 2 psi)	Sample Mass (g)	Solids Mass (g)	yr or yu (wppm)
1/F	12.6	0.15	6	524.3	0.4705	885
2/U	12.6	0.15	6	525.5	0.3003	559
3/ <b>F</b>	16.6	0.15	9	813.7	0.7224	876
4/U	16.6	0.15	9	955.3	0.4620	472
5/F	26.5	0.13	18	1149.0	1.0084	866
6/U	26.5	0.13	18	1054.8	0.3964	364
7/F	16.6	0.14	9	914.6	0.8019	865
8/U	16.6	0.14	9	877.3	0.4071	452
9/F	24.3	0.14	18	1171.0	1.0278	866
10/U	24.3	0.14	18	1066.0	0.4144	377
11/F	12.0	0.15	6	551.8	0.4908	878
12/U	12.0	0.15	6	492.6	0.2064	407

T = 18.5°C

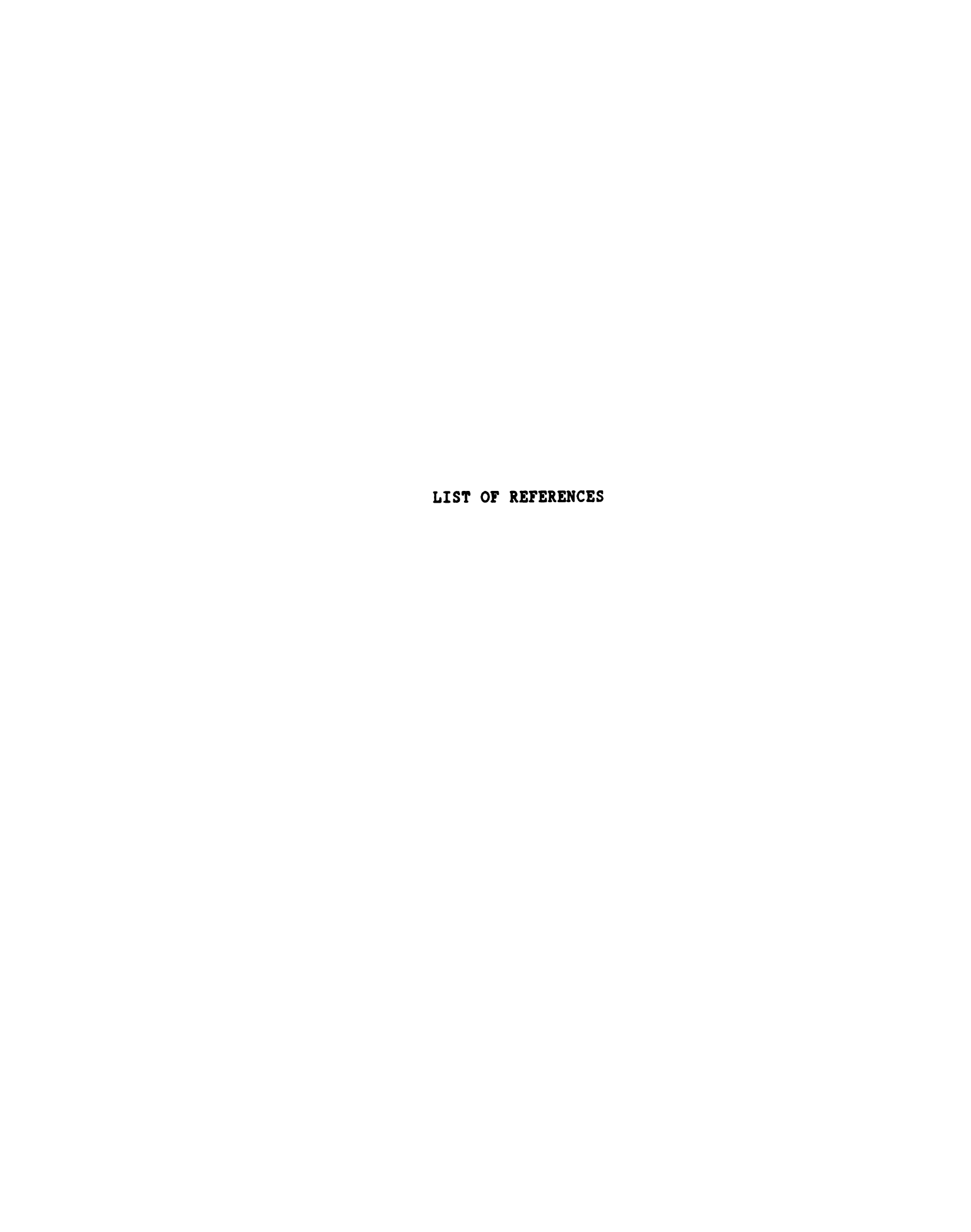
# Experiment # 4

1/F	11.5	0.15	5±2	529.6	0.4571	851
2/U	11.5	0.15	5±2	528.0	0.2966	550
3/U	16.7	0.14	9±2	736.1	0.3367	445
4/U	24.4	0.14	17±2	1037.6	0.3898	364
5/U	17.1	0.14	10±2	750.8	0.3219	417
6/ <b>F</b>	25.4	0.14	19±2	1140.6	0.9582	828
7/ט	25.4	0.14	19±2	1164.6	0.4092	339
8/U	11.4	0.15	6±2	565.4	0.2472	425

 $T = 20.5^{\circ}C$ ,  $(y_F)_{AVG} = 840 \text{ wppm}$ 

Concentrations corrected for 12 wppm dissolved/stray solids content tap water.

<sup>\*</sup>F = Feed, U = underflow



#### LIST OF REFERENCES

- BIRD, R.B., STEWART, W.E., and E.N. LIGHTFOOT, 1960, Transport Phenomena, Wiley, New York.
- BOHNET, M., 1969, "Trennen Zweier Flusaigkeiter im Hydrozyklon", Chemie-Ing.-Techn. 41, Jahrg., (1969), p.381.
- BOUCHILLON, C.W., 1963, "Particle Trajectories in a Hydrocyclone", Ph.D. Dissertation, School of Mechanical Engineering, Georgia Institute of Technology.
- BOYCE, W.E., and R.C. DIPRIMA, 1977, <u>Elementary Differential Equations</u> and Boundary Value Problems, 3rd edition, John Wiley, New York.
- BRADLEY, D., 1965, The Hydrocyclone, Pergamon Press, New York.
- BRADLEY, D., and D.J. PULLING, 1959, "Flow Patterns in the Hydraulic Cyclone and Their Interpretation in Terms of Performance", Trans. Inst. Chem. Eng., 37, p34.
- COLMAN, D.A., 1981, "The Hydrocyclone for Separating Light Dispersions", Ph.D. Dissertation, Department of Mechanical Engineering, Southampton University.
- COLMAN, D.A. and M.T. THEW, 1983, "Correlation of Separation Results From Light Dispersion Hydrocyclones", Chem. Eng. Res. Des., 61, July 1983, p.233.
- COLMAN, D.A., THEW, M.T., and D. LLOYD, 1984, "The Concept of Hydrocyclones for Separating Light Dispersions and a Comparison of Field Data with Laboratory Work", p.217 in <a href="https://hydrocyclones.com/Hydrocyclones">Hydrocyclones</a>, R. Pickford (Editor), BHRA 2nd International Conference on Hydrocyclones, University of Bath.
- CRC Handbook of Chemistry and Physics, Weast, R.C., 1988, 68th edition, CRC Press.
- DABIR, B., 1983, "Mean Velocity Measurements in a 3" Hydrocyclone Using Laser Doppler Anemometry", Ph.D. Dissertation, Michigan State University.

- DAHLSTROM, D.A., 1952, "High Efficiency Desliming By Use of Hydraulic Water Additions to the Liquid-Solid Cyclone", Mining Engineering, August 1952, p.789.
- DENNIS, R., SAMPLES, W.R., ANDERSON, D.M., and L. SILVERMAN, 1957, "Isokinetic Sampling Probes", Industrial and Engineering Chemistry", 49, No.2, p.294.
- FUCHS, N.A., 1964, The Mechanics of Aerosols, Pergamon Press, New York.
- HAYES, J.J., CARROLL, W.C., FOTHERGILL, D.W.J, and G.J.J. PRENDERGAST, 1985, "Hydrocyclones for Treating Oily Water: Development and Field Testing in Bass Strait", 17th Annual Offshore Technology Conference, May 6-9, OTC 5079, Houston, TX.
- HITCHON, J.W., 1959, "Cyclones as Liquid-Liquid Contactor-Separators", AERE CE/R 2777.
- HINZE, J.O., 1959, Turbulence, McGraw-Hill, New York.
- HORNBECK, R.W., 1975, <u>Numerical Methods</u>, Prentice-Hall, Englewood Cliffs, New Jersey.
- International Critical Tables of Numerical Data of Physics, Chemistry, and Technology, Washburn, W.E., 1926, National Research Council, McGraw-Hill, New York.
- KELSALL, D.F., 1952, "A Study of the Motion of Solid Particles in a Hydraulic Cyclone", Trans. Inst. Chem. Eng., 30, p.87.
- KIMBER, G.R. and M.T. THEW, 1974, "Experiments on Oil/Water Separations with Hydrocyclones", Proc. 1st European Conference on Mixing and Centrifugal Separation, Cambridge, September 1974, Paper E1, BHRA, Cranfield.
- KREITH, F. and M.S. BOHN, 1986, <u>Principles of Heat Transfer</u>, Harper and Row, New York.
- MCCRACKEN, D., 1967, Fortran with Engineering Applications, John Wiley, New York.
- MELDRUM, N., 1987, "Hydrocyclones: A Solution to Produced Water Treatment", Proc. 19th Annual Offshore Technology Conference, OTC 5594, Houston, April 27-30.
- REGEHR, H.- U., 1962, "Untersuchungen die Entischung Disperser Stoff Systeme im Hydrozyklon", Forsch. Gebiete Ingenieurwes, 28, 11/27.
- RIETEMA, K., 1961, "Performance and Design of Hydrocyclones I-IV, Chem. Eng. Sci., 15, pp.298-325.

- SIMKIN, D.J. and R.B. OLNEY, 1956, "Phase Separation and Mass Transfer in a Liquid-Liquid Cyclone", AICHE Jl. 2, p.545.
- SVAROVSKY, L., 1984, Hydrocyclones, Holt Technology, New York.
- SVAROVSKY, L., 1977, Solid-Liquid Separation, Butterworths, London.
- TEPE, J.B. and W.K. WOODS, 1943, "Design of Ether-Water Contacting System", United States Atomic Energy Commission, AECD-2864.

